DEVELOPMENT OF A PASSIVELY STABLE PYRAMID SAIL TO DEORBIT SMALL SATELLITES

A Dissertation
Presented to
The Academic Faculty

By

Alexandra C. Long

In Partial Fulfillment
of the Requirements for the Degree
Doctor of Philosophy in the
School of Aerospace Engineering

Georgia Institute of Technology

August 2018

DEVELOPMENT OF A PASSIVELY STABLE PYRAMID SAIL TO DEORBIT SMALL SATELLITES

Approved by:

Dr. David A. Spencer, Advisor
School of Aerospace Engineering
Georgia Institute of Technology

Dr. Glenn Lightsey, Co-Advisor
School of Aerospace Engineering
Georgia Institute of Technology

Dr. Julian Rimoli
School of Aerospace Engineering
Georgia Institute of Technology

Mr. Mark Schoenenberger
Atmospheric Flight and Entry Systems Branch
NASA Langley Research Center

Mr. Les Johnson
Advanced Concepts Office
NASA Marshall Space Flight Center

Date Approved: July 10, 2018

What are the principal reasons for undertaking a national space program? ... The first of these factors is the compelling urge of man to explore and to discover, the thrust of curiosity that leads men to try to go where no one has gone before. Most of the surface of the earth has now been explored and men now turn to the exploration of outer space as their next objective.

"Introduction to Outer Space", by Dwight D. Eisenhower's Presidential Science Advisory Committee, March 26, 1958

To my amazing family whose love and support helped me to persevere through the years of education, specifically my sisters who inspired me to be good at math by forcing me to be scorekeeper at every game from a young age. They were only a phone call away.

ACKNOWLEDGEMENTS

This research was supported by a NASA Space Technology Research Fellowship. I would especially like to thank Mark Schoenenberger, Juan Fernandez, Garry Qualls, and Jin Ho Kang of NASA Langley Research Center; Andrew Heaton of NASA Marshall Space Flight Center; Jeremy Banik of the Air Force Research Laboratory; and Kenneth Hart of Georgia Institute of Technology for their advice towards the completion of this work. Glenn Lightsey of Georgia Institute of Technology provided the space and tools to conduct testing; and I appreciate Terry Stevenson, Andrew Fear, Shaj Patel, Christopher Pubillones, Warren Eshpeter, and the rest of the volunteers at Georgia Institute of Technology for their help folding the sail. I would like to acknowledge Tony Cofer, Bartlomiej Kokot, Alexis Lora de la Calle, and the other students at Purdue University for their work developing the engineering and ight units for the ADE system. Brandon Warren of the University of Nebraska designed the test rigs for the SHEARLESS Testing and Greg Dean of NASA Langley Research Center helped support that testing. In addition, I would like to thank McKenzie Long of Cardinal Innovative for creating the square pyramid graphic that appears in chapter three, and for copy editing this dissertation.

CONTENTS

LIST OF TABLES

LIST OF FIGURES

SUMMARY

Orbital debris is a growing problem in low-Earth orbit, especially with a number of commercial companies intending to launch hundreds to thousands of micro-satellites into this regime with the goal of providing global internet service. The main goal of this research is to create a system that will passively deorbit a small satellite from low-Earth orbit within 25 years to reduce the probability of collision. This will create an option for satellite designers that will easily allow them to follow end-of-life guidelines. This is accomplished with three contributions to the current state of the art.

The first contribution is the design of an aerodynamically stable, passive, deployable drag device for small satellite deorbit. The first step was to conduct a trade study that compares five technologies commonly proposed for deorbit purposes, and it concludes that an aerodynamically stable drag sail is the favored choice based on performance, reliability and impact to the host spacecraft. Next, the system level requirements are to create a scalable system that includes the required size of the sail for specific masses and orbit altitudes. It estimates the operational loads on the booms to develop structural requirements, and analyzes the material and thickness of the sail membrane to ensure it survives the atomic oxygen in low Earth orbit for the duration of the deorbit period. Finally, the stability was analyzed in a simulation the integrated the attitude and orbital behavior of a satellite with the drag sail.

The second contribution is development and laboratory testing of a 1:10 scale prototype of the drag device to demonstrate functionality. A conceptual design for an ESPA-class drag sail is discussed, followed by the detailed design and prototype testing of a CubeSat-class sail that will be launched as part of the Aerodynamic Deorbit Experiment. The third contribution is the characterization of the SHEARLESS booms that were developed at NASA Langley. These are the booms used in the drag sail design, and the characterization was accomplished with bending and torsion testing of two different sizes of booms.

CHAPTER 1
INTRODUCTION

Orbital debris is a growing problem in low-Earth orbit; it has crossed a threshold of critical density where the number of debris objects will continue to grow exponentially due to collisions unless actively mitigated [1]. The current trend is to develop and launch small satellites instead of the historical multi-ton behemoths. This creates a need for a standard system to deorbit these satellites that can be scaled to match the size and orbit of the satellites. A reliable system for small satellite deorbit is required for the commercial small satellite constellations consisting of hundreds to thousands of micro-satellites in Low-Earth Orbit (LEO) at altitudes ranging from 1,000-1,200 km that provide global internet service [2, 3, 4]. The need to deorbit these microsatellites at the end of their operational lifetime is apparent since a 100 kg satellite with a 0.25 m^2 frontal area would take more than 100 years to deorbit naturally from a 1,100 km circular equatorial orbit. This research is focused on accelerating the orbit degradation of small satellites by using a deployable drag sail that is attached to the satellite before launch. Following the operation of the satellite, the drag sail is deployed to passively decrease the orbit lifetime of the system. It will be stowed using a small footprint and a simple interface with the spacecraft. This research describes an aerodynamically stable drag sail comprised of four thin membranes that are supported with deployable booms in the shape of a square pyramid. Therefore, the sail is called the Passively Stable Pyramid Sail or $[PS]^2$.

1.1 The Orbital Debris Problem

In 1978, David Kessler and Burton Cour-Palais predicted that collisions between satellites would become a significant source of debris, leading to a period of exponential growth of debris [5]. The threshold leading to this exponential growth eventually became known

as Kessler Syndrome.Kessler revisited the results from his original paper with new data and modelling techniques in 2010, and concluded that although new operational procedures have helped to control the growth of debris due to collisions, the threshold has been exceeded. In order to prevent future growth, there must be 90% compliance with post mission disposal guidelines, as well as removal of the five objects most likely to cause debris [6]. Those post mission disposal guidelines require spacecraft in Low Earth Orbit (LEO) to deorbit within 25 years after the end of their mission [7, 8].

Two main events reinforced to the space community importance that the problem of orbital debris needed to adressed. In 2007, the Chinese government conducted an antisatellite test on the Fengyun satellite, and in 2009, a Cosmos satellite collided with an Iridium satellite. Figure 1.1 shows the number of tracked objects in Earth orbit by year [9]. It is important to note that the majority of tracked objects are fragmentation debris, with two large increases corresponding to those key events.

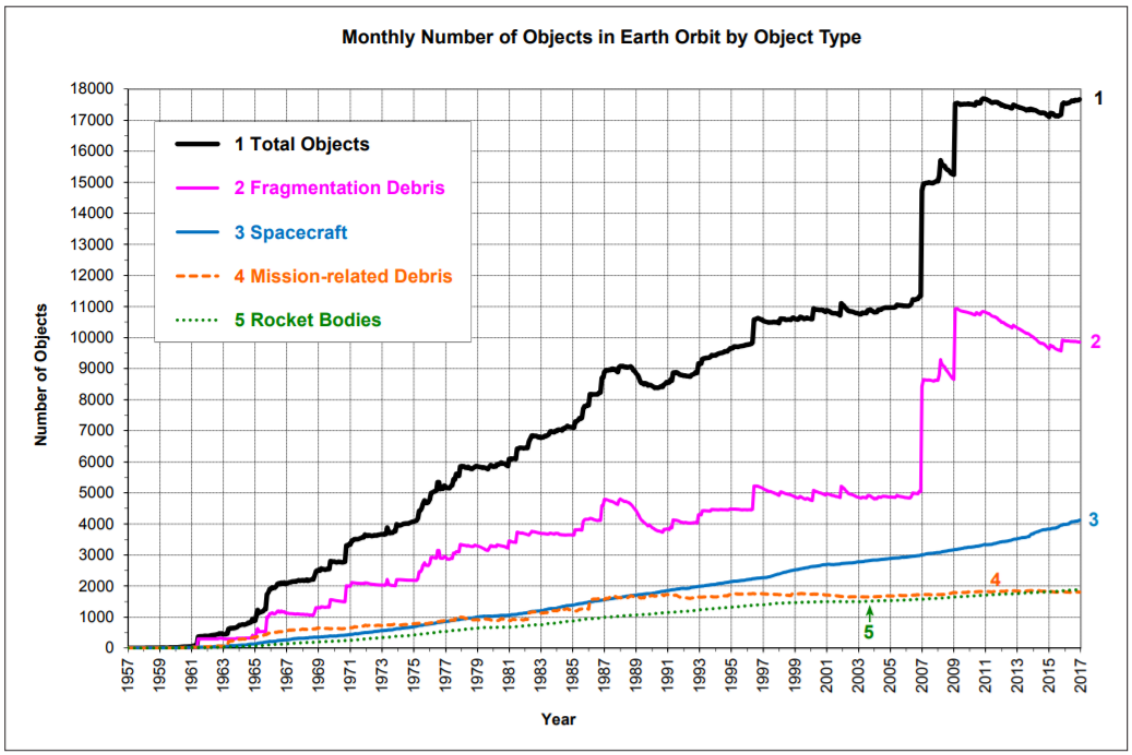

Figure 1.1: Yearly increase in number of tracked objects in Earth orbit [9]

The fragmentation debris shown in Figure 1.1 reflects only a small percentage of objects

capable of disabling a satellite, since only objects greater than about 10 cm in diameter are tracked. Levin et al. describes three main types of lethal debris objects in LEO [1]. The first, called "shrapnel", which is about 1 cm in size and comprises about 98% of the lethal objects. "Shrapnel" is the primary threat to satellites because it is too small to track and avoid, but too heavy to be shielded against. The second type is called "hubcaps". "Hubcaps" are greater than 10 cm with masses less than 2 kg, so are tracked. These make up about 2% of lethal objects and cause the most conjunctions and avoidance maneuvers. The final type of lethal debris is referred to as "cars" because they are over 2 kg. While "cars" make up less than 1% of lethal objects, they are the primary source of new shrapnel because they represent 99% of the collision area and mass [1]. It is misleading to call a 3 kg object a "Car", but dividing up that group into different sections does not make sense based on the percentage of the population. Therefore, in this research, the categories will be small, medium, and large objects.

McKnight et al. describes three types of orbital collisions [10]. A Type I collision is when a small object strikes and disables an operational satellite, creating more small fragments. Type II is when a medium strikes a large object, creating thousands of lethal and trackable objects. The final and most concerning collision is Type III, where two large objects collide and create double the number of lethal objects as a Type II collision [10]. The Cosmos-Iridium collision was a Type III. This demonstrates why only five large objects per year could make a significant difference in the growth rate, according to Kessler et al. [6]. Luckily, the disasterous Type III collisions are only likely in certain orbital regimes. Figure 1.2 shows a histogram that sorts the space objects described in Figure 1.1 by orbital altitude and inclination [11]. It can be seen that a large majority of objects are only in a few inclination bands. Figure 1.3 is the same data with the altitude restricted to 500-1300 km, and the inclination restricted to 60° - 150° to reveal more details. These more populated regions (especially altitudes of 760-780 km, 840-860 km, and 940-980 km) are significantly more susceptible to those Type III collisions [10], but are also very desirable for satellite

missions. Large objects in these bands are why Kessler specified objects are most likely to cause collisions, rather than just saying a certain mass or size [6]. This research focuses on technology for post mission disposal, but a short explanation of active debris removal is given in the next section.

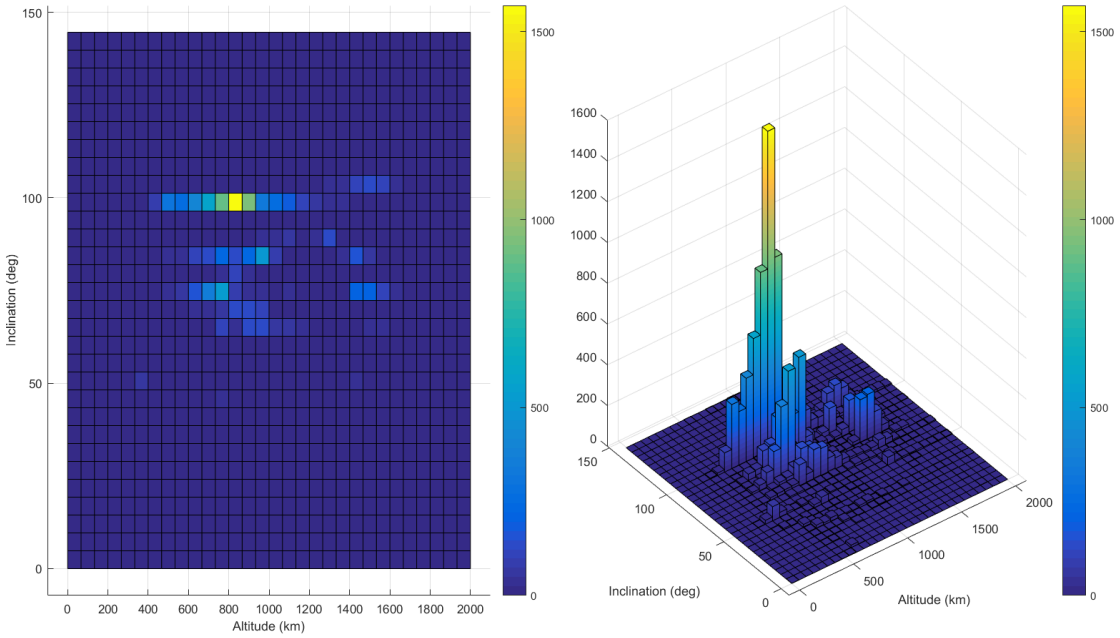

Figure 1.2: Number of objects in LEO sorted by altitude and inclination. Data compiled from the Satellite Situation Report from Dec 15, 2017 [11]

1.2 Current State of the Art

As mentioned above, removing space objects is necessary to protect the use of space. This removal is divided into two categories based on who initiates the removal: the spacecraft operators or an external entity. The former case uses a plan that is part of the spacecraft design and is initiated at the end of the spacecraft lifetime, while the latter case is usually accomplished after the spacecraft has been abandoned [10]. Removal from LEO initiated by the spacecraft operator is referred to as post mission disposal (PMD), and removal initiated by an external entity is referred to as Active Debris Removal (ADR). The current state of the art of both of these technologies will be discussed in this section. There are many

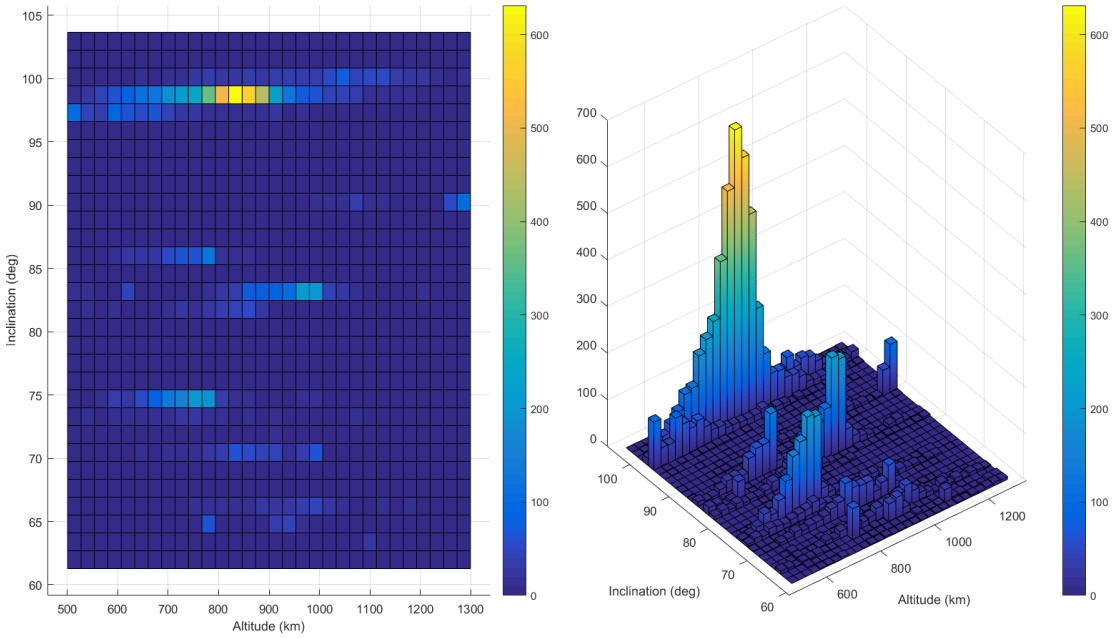

Figure 1.3: Number of objects in LEO sorted by altitude and inclination zoomed in to the populous region. Data compiled from the Satellite Situation Report from Dec 15, 2017 [11]

innovative ideas that have been proposed and brought to different levels of technological readiness.

1.2.1 Active Debris Removal

The basic concept of Active Debris Removal is that after a derelict object is identified for deorbit, the ADR system is launched to rendezvous with the object. The system then captures the target and maneuvers it to a deorbit trajectory. There have been many proposed concepts, but this is a technologically challenging problem to solve, most significant is figuring out how to deploy this technology on a large enough scale to make a difference. As mentioned earlier, Kessler et al. argues that the active removal of at least five large objects per year is necessary to maintain the current population level of objects in LEO [6].

The challenge for the rendezvous phase concerns the operations and economics of the system. One concept is a system that will deorbit with its target object, which requires a launch slot for each derelict object. The Tethered Tug, designed by the University of Colorado, Boulder, is an example that uses the residual fuel in a Soyuz upper stage to

rendezvous and dock with debris via a tether and then deorbit both the debris and upper stage with the Soyuz engine [12]. A competing concept is that of a mothership that carries multiple capture and deorbit modules. The mothership will rendezvous with an object, deploy a module, then move on to the next object until all deorbit modules have been used, similar to the Deorbiter CubeSat concept proposed by the University of Toronto [13]. A final concept is one that captures an object, than maneuvers to an orbit where the object is released onto a deorbit trajectory. This allows a single system to deorbit multiple derelict objects during a mission. An example is the DEbris Capture and Orbital Manipulation (DECOM) system designed by the University of Washington that uses electric propulsion for the maneuvers [14]. The concept of operations is shown in Figure 1.4.

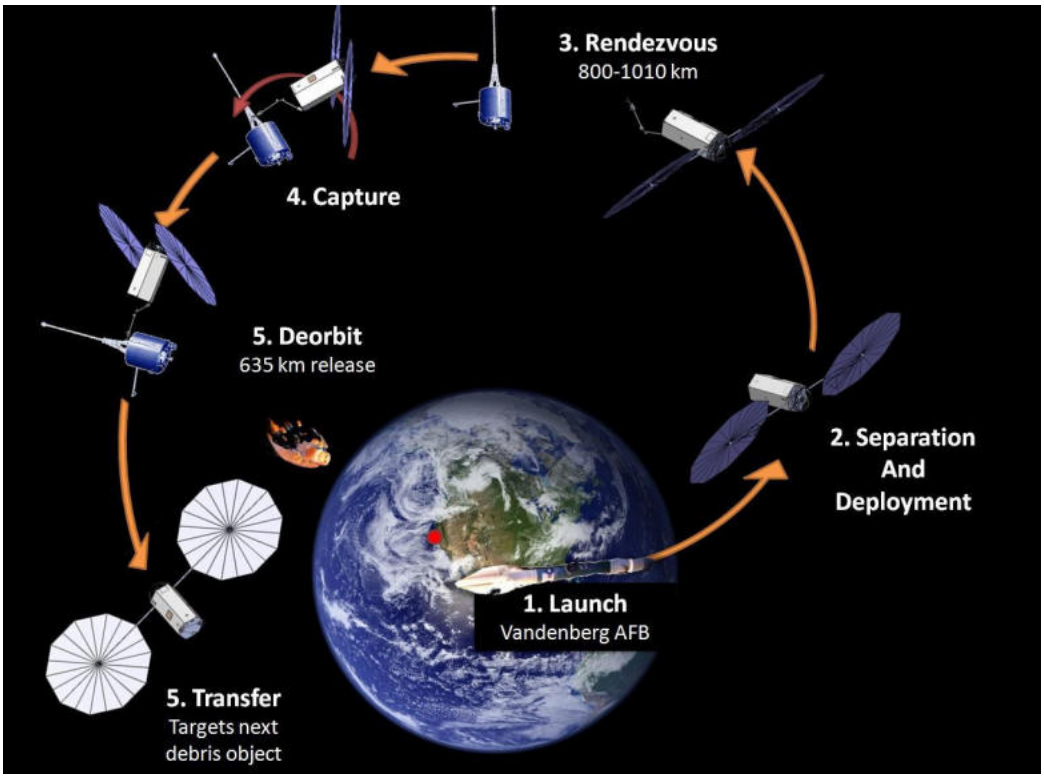

Figure 1.4: Concept of operations for the DEbris Capture and Orbital Manipulation mission (DECOM) [14]

Another focus of current research is the technology required to capture uncooperative objects. The most common ideas are: a net [15], a harpoon [16], a robotic arm [17], or a claw-like system [18]. Many of these missions are in the laboratory prototyping phase, but

the RemoveDebris mission was launched early 2018 by a consortium of partners funded by the European Space Agency. The goal is to demonstrate key ADR technologies on orbit, such as net capture, harpoon capture, vision-based navigation, and drag sail deorbitation [16].

1.2.2 Post Mission Disposal Technologies

The technologies used to remove satellites from orbit when initiated by the satellite operator are referred to as Post Mission Dispoal (PMD) technologies because the goal is for the satellite to burn up in the atmosphere during reentry. These technologies are part of the satellite design and are launched with the satellite. All modify the orbit to place the satellite on a trajectory that will ensure it deorbits, defined as the altitude falling below 100 km, within 25 years. PMD can be separated into two categories: active and passive.

Active PMD technologies require a fully functioning satellite to control the system. These technologies include traditional propulsion, both chemical and electric. Chemical propulsion usually accomplishes the trajectory modification in a single deorbit burn lasting a few minutes, while electric propulsion requires hours or days to achieve the required change in velocity. Both systems can be integrated into the satellite either by expanding the capabilities of the onboard propulsion unit or as an external PMD module. For example, the company D-Orbit has an independent propulsion module with solid rocket motors [19]. D-Orbit has configurations for a range of satellite sizes (100-3000 kg), and all the different Earth orbit regions (i.e. LEO, MEO, and GEO) [19]. This independent system helps to enforce the regulation by removing the temptation to extend the lifetime of the satellite with the propellant reserved for PMD.

Passive PMD technologies only need to be deployed before initiating the deorbit of the host satellite because they use the atmoshphere and/or the Eath's magnetic field to remove energy from the satellite. The three types most often described in the literature are tethers, inflatable balloons, and drag sails.

A tether is a long, thin exposed wire that is deployed from a satellite. As seen in Figure 1.5, the motion of the conducting tether through the Earth's magnetic field will generate a voltage along the tether that induces a current. This current interacts with the Earth's magnetic field to generate a Lorentz force that opposes the orbital motion [20]. Tethers Unlimited has three versions of an electrodynamic tether called the Terminator Tether designed to deorbit CubeSats, nanosats (<100 kg), and microsats (<200 kg) within 25 years [20, 21]. A CubeSat Terminator Tape produced by Tethers Unlimited is currently on-orbit, but deployment of the tape has not yet been initiated.

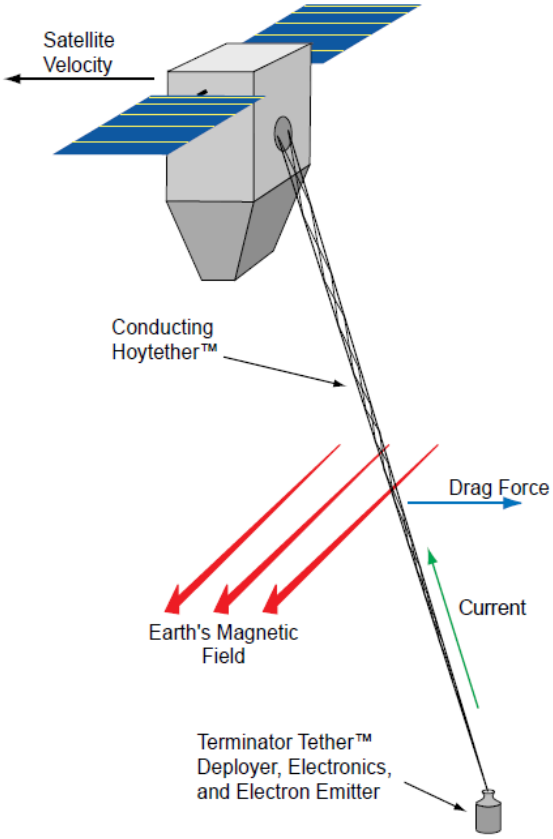

Figure 1.5: The Terminator Tether and how it creates drag with its electrodynamic tether. [20]

Inflatable balloons and drag sails accomplish deorbit by increasing the surface area of the satellite to take advantage of the atmospheric drag found in LEO. An inflatable balloon is a thin membrane that is inflated using a gas to create the drag area. Some designs depend on the inflation to maintain the drag area, while others use a chemical reaction to rigidize

the balloon after the initial inflation [22]. Figure 1.6 shows one balloon concept called the Gossamer Orbit Lowering Device (GOLD) that was developed by Global Aerospace Corp. [23].

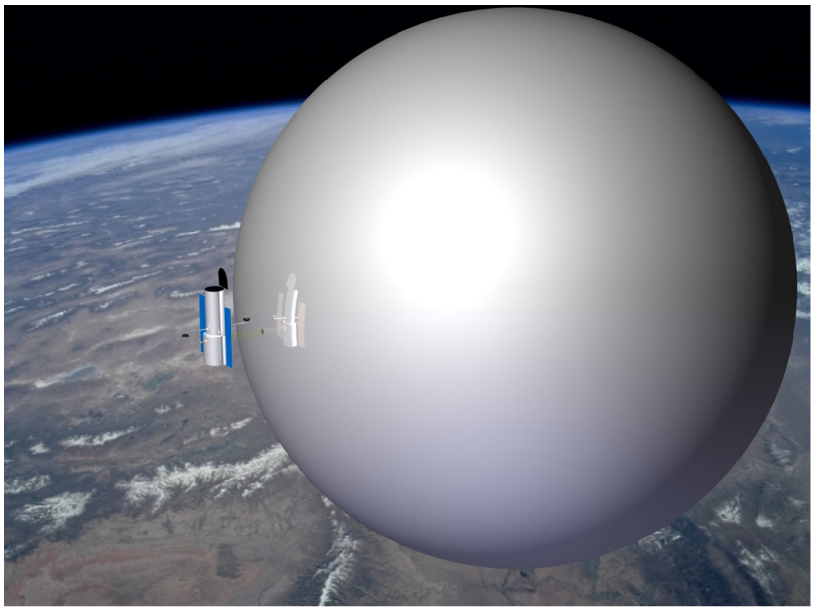

Figure 1.6: The Gossamer Orbit Lowering Device initiating deorbit [23]

A drag sail is composed of a thin membrane that is supported by a structure, similar to a solar sail, as shown in Figure 1.7. There have been several drag sail systems packaged within 3U cubesats or smaller, listed in Table 1.1. The dragNET system successfully deorbited a Minotaur I upper stage (about 100 kg mass [24]) in about two years after launching the ORS-3 mission to an altitude of 500 km and an inclination of 40.5° [25, 26]. Without the device, it could have taken up to six years to deorbit. InflateSail decreased the deorbit time of a 3U Cubesat bus from an estimated five years to 72 days, deorbiting from a 505 km altitude, 97.44° orbit [27]. The CanX-7 satellite demonstrated a significant change in altitude decay rate after the sails were deployed [28]. Using PMD is inherently the superior option compared to ADR because the reduction of the time spent in orbit is designed into the satellite, and once full compliance with the 25 year guideline is reached, ADR will only be needed for rare failure events.

Figure 1.7: The dragNET drag sail system [29]

Table 1.1: List of drag sail missions and their status

Name	Drag Area (m^2)	Organization	Status	Reference
dragNET	14	MMA Design	Flown & Deorbited	[29, 25]
AEOLDOS	1, 1.5, 3	University of Glasgow	In development	[30]
Deorbitsail	25	University of Surrey	Failed to deploy	[31, 32]
Inflatesail	10	University of Surrey	Flown & Deorbited	[33]
CanX-7	4	University of Toronto	Flown	[34, 35]

1.2.3 Solar Sail Missions

Solar sails and drag sails are often mentioned in the same sentence because they are different applications of the same technology. Both are inspired by conventional seafaring sailboats that use a sail to capture the force of the wind to use for propulsion. A drag sail utilizes atmospheric drag to change the energy of its system, and a solar sail utilizes solar radiation pressure for propulsion. This concept has captured the imagination of engineers for decades, inspring concept studies as early as the 1970s when the Jet Propulsion Laboratory designed a solar sailing spacecraft to rendezvous with Halley's Comet. This mission was cancelled, but it advanced the technology [36].

The next major step forward for this technology was NASA's In-Space Propulsion Technology project in the early 2000s. This project funded the development of large solar sail systems, and two competing companies, ATK Space Systems and L'Garde Inc., tested fully

integrated 20-m sail systems under high vacuum and an appropriate thermal environment [37]. Both systems were square, with four membrane quadrants supported by four booms, as shown in Figure 1.8. The ATK sail used coilable truss booms with a CP1 sail membrane [38] and the L'Garde sail used inflatable booms with a mylar sail membrane [39]. This configuration and the technology developed for both sails has been used in all of the solar sails developed in the United States since.

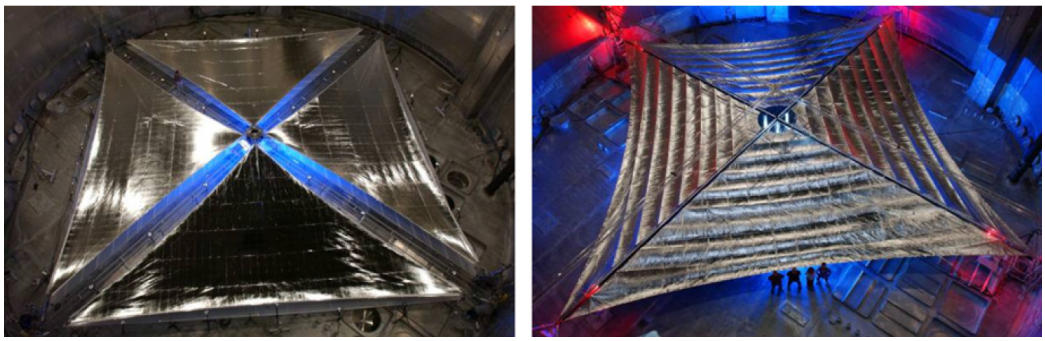

Figure 1.8: The 20 m solar sails during the ground tests of the NASA In-Space Technology Project; ATK Space Systems (left), L'Garde Inc. (right) [37]

The first sail to successfully deploy and demonstrate solar sailing was the Interplanetary Kite-craft Accelerated by Radiation Of the Sun (IKAROS) built by the Japanese Exploration Agency (JAXA). It was a 200 m^2 square solar powered sail launched in 2010, but was deployed and tensioned by centrifugal forces instead of static booms. The sail material included flexible thin film solar cells to allow the sail to provide power as well as thrust while it traveled to Venus [40, 41, 42].

The next sucessful solar sail mission was Nanosail-D2. This mission leveraged the technology from the ATK solar sail to develop a 10 m^2 sail housed in a 3U cubesat. It demonstrated that the sail could accelerate deorbit by using atmospheric drag, and showed that the the solar radiation pressure had a significant effect on the attitude because of its reflective membrane [43]. It was a collaboration between NASA Marshall Space Flight Center, which built the solar sail, and NASA Ames Research Center, which built the cubesat bus [44]. A larger version with an 85 m^2 sail is currently being built for the Near-Earth Asteroid (NEA) Scout mission to be used to propel the spacecraft on a trajectory to fly

by an asteroid. This is the one American sail that does not use four membrane quadrants. Instead, it uses one large square membrane supported by four booms, which remain shaded from the sun by the membrane [45].

The Planetary Society developed a solar sail for the LightSail program. It is a 32 m^2 solar sail housed in a 3U cubesat. LightSail 1 was launched in 2015, successfully deployed the solar sail, and demonstrated functionality of the cubesat bus in June of that year. The LightSail 2 mission is scheduled to fly in 2018 with the goal of controlling the sail orientation with a momentum wheel to modify its orbital parameters [46, 47, 48, 49].

There are two notable solar sail missions that were designed but never flown. The first Sunjammer mission was selected for development through the NASA Space Technology program in 2011 and was designed to have a 1208 m^2 solar sail. Before it was cancelled in 2014, one quarter of the sail was successfully deployed in a lab [50]. The second mission is CubeSail which was developed by the University of Surrey. It was a 25 m^2 solar sail deployed from a 3U cubesat and developed around the same time as Nanosail-D and LightSail [51, 52].

1.2.4 Deployable Booms

Deployable structures are important for modern spacecraft to overcome the volume constraint imposed by the launch vehicle payload fairing by unfolding to a significantly larger size upon reaching space. This technology enables a range of missions, from those that require more solar panels than can be mounted to the spacecraft body, to large telescopes that require large apatures,like the James Webb Space Telescope. A subset of deployable technologies is gossamer structures, ultra-low-mass structures usually made out of inflatables or ultra-thin composites used on spacecraft where a large structure is required for a very small mass. This is important for drag sails and solar sails because their performance depends on maximizing the area of the sail (A) and minimizing the mass of the full system (m). This allows the system to maximize its acceleration (a) from an external pressure (P),

as described by the basic relationship shown in Equation (1.1).

$$a = \frac{PA}{m} \tag{1.1}$$

As was explained earlier, drag sails create their drag area by supporting thin membranes between mostly rigid booms. The membranes are usually made of Kapton, Mylar, CP1, or a similar polymer that is anywhere from 2 - 25 μm thick, allowing the mass and packaged volume of the membrane to be fairly minimal. The on-orbit lifetime of the membrane material is a concern that will be discussed later. The bigger concerns are the booms and the mechanisms required to deploy them.

There are a number of different categories of booms that vary on packing efficiency, mass, strength, and length. One example is a telescoping boom, shown in Figure 1.9. It consists of a series of cylinders that are stowed by retracting inside each other. They require a deployment actuator to deploy, but this also allows the booms to be retracted. Telescoping booms are often used when high strength and stiffness are required, but because of their higher mass and stowed volume, they are usually not used in gossamer structures.

Another common boom type is a folding boom, which has hinges that unfold. There are many different kinds folding booms with various hinge designs. They are not good options for drag sails because the deployment path is not linear. A linear deployment path is important since most drag sail booms pull out the sail membranes during deployment, and booms that have less predictable paths pose the risk of the membranes getting tangled.

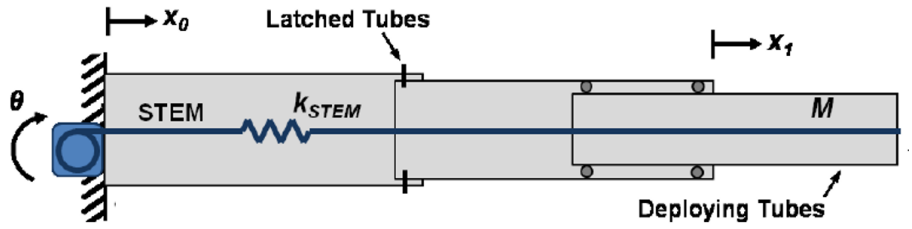

Figure 1.9: Diagram of a telescoping boom [53].

A third option is the coilable mast that was used in the design of the ATK solar sail discussed in the previous section. As can be seen in Figure 1.10, this boom is a truss structure that has continuous longerons that allow it to be stowed in a cylindrical volume that is less than 2% of its deployed length. It is deployed by the stored strain energy in the longerons, and controlled by a lanyard that is connected to a motor to limit the deployment rate. This system is very efficient and is able to be used at fairly long lengths [54].

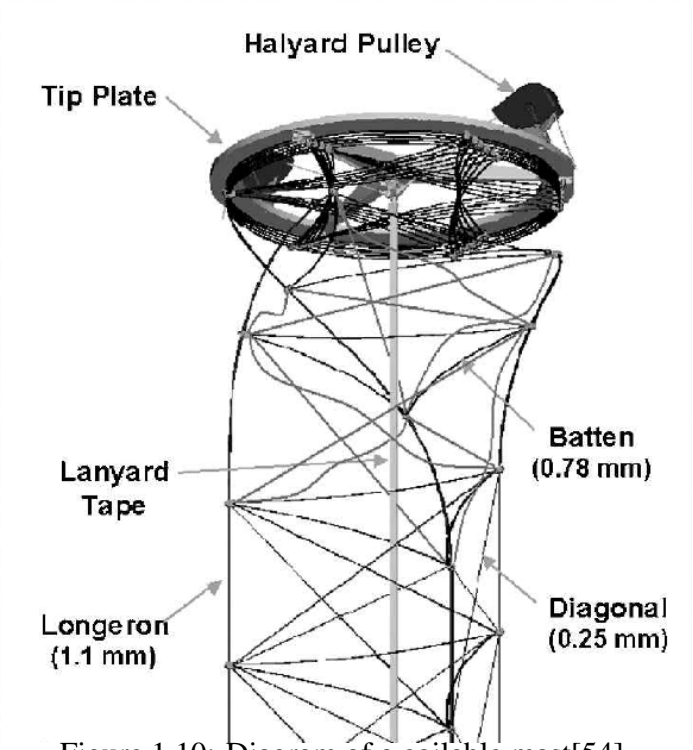

Figure 1.10: Diagram of a coilable mast[54].

An inflatable boom, like the one used in the L'Garde solar sail, is composed of a tube made from a membrane similar to that of the sail, and is deployed by inflating with air. Most designs then use a chemical reaction to rigidize the booms after they are fully deployed to prevent deflation. There remains a risk of micrometeoroids ripping holes in the booms before they can be rigidized. Inflatable booms are also well suited for large structures [55].

The final boom type is called a rollable boom, also known as collapsible tube booms or flexible shell booms. They have thin walls that allow them to be flattened then rolled around a hub when they are stowed. These are often made out of either thin composites like carbon-

fibered reinforced plastics, or stainless steel. Carbon fiber is becoming more common as technology has improved to allow for thinner shells because carbon fiber deflects less under direct sunlight [56]. This boom type is better for smaller scale projects because the stowed height has been demonstrated as small as 20 mm, but the demonstrated length is around 10 m. The specific properties of the boom are highly dependent on size and cross section. The earliest cross section, and the basis for all of the following cross-sections, is the tape spring shown in Figure 1.11. This is the same design as a common tape measure, and the benefit is that it is strained elastically when stowed, but essentially strain free when deployed. The key parameters are the radius of curvature, R, and the subtended angle, α [57].

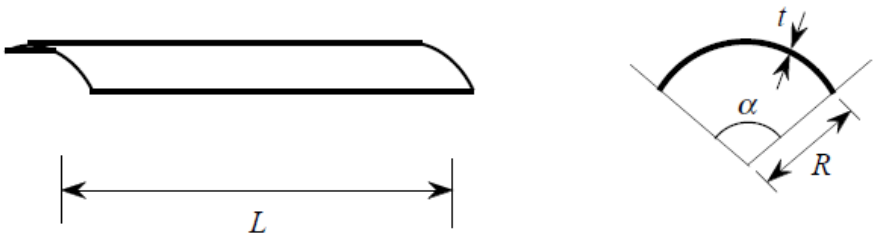

Figure 1.11: Deployable tape spring geometry [57].

Figure 1.12 shows the next generation of rollable boom cross sections, both flattened and deployed. The Storable Tubular Extendable Member (STEM) is a tape spring with $\alpha > 360°$ to create a closed cross section. The Collapsible Tubular Mast (CTM) is two tape springs bonded with their curvature facing each other to create a closed cross-section. This provides rotational stiffness, but the CTM has a smaller cross sectional inertia for its stowed height when compared to the Triangular Rollable And Collapsible (TRAC) boom, which is two tape springs bonded with their curvatures facing away [58]. The CTM and TRAC booms have problems with high stresses induced at the bond areas when they are coiled, among other issues. The SHEAth-based Rollable LEnticular-Shaped and low-Stiction (SHEARLESS) boom, shown in Figure 1.13, tries to solve this problem by coupling two tape springs with a polymer sleeve instead of bonding. This allows for lower stored energy in the boom and allows for a smaller coiling diameter [59].

When designing a system for the rollable booms, one of the main challenges is boom

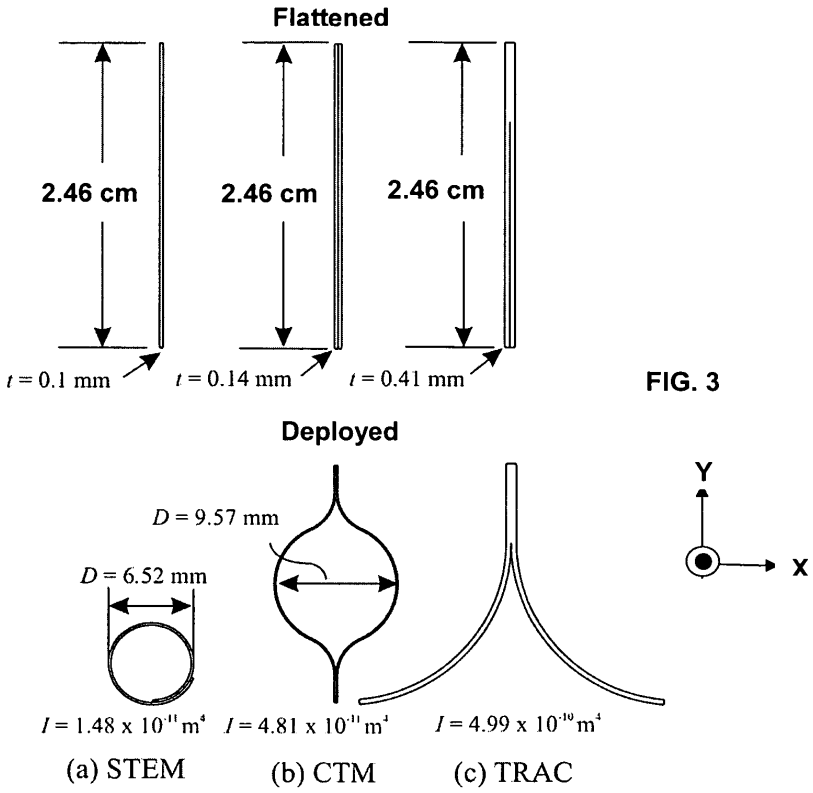

Figure 1.12: Deployable boom cross-sectional geometry, both collapsed and deployed[60].

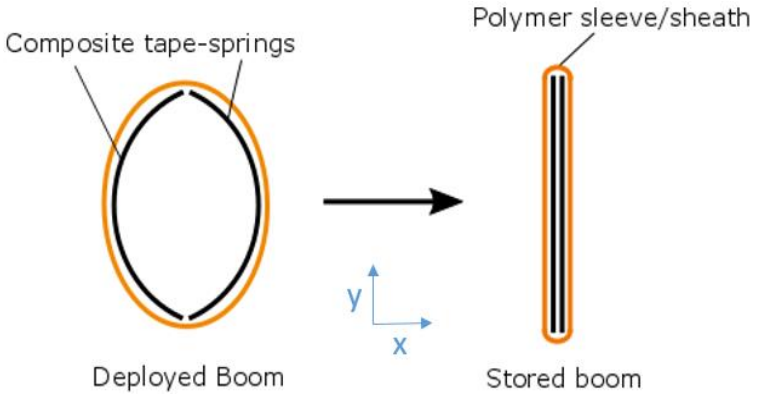

Figure 1.13: SHEARLESS boom in the stowed and deployed state[59].

blossoming. Blossoming, sometimes referred to as blooming, is when the coils of booms that are wrapped around a rotating central hub do not rotate rigidly with the hub and instead the layers slide with respect to each other, resulting in the inner coils of the boom expanding to a lower energy state, as illustrated in Figure 1.14. This expansion can cause the boom to jam inside the deployer, and risks damaging the booms due to the angle at the roots.

The accepted way to prevent this is by applying a force normal to the outside of the coil, directed inward, that is continuous over the deployment using various mechanisms that utilize springs. In the past, the required spring force has been determined empirically [61].

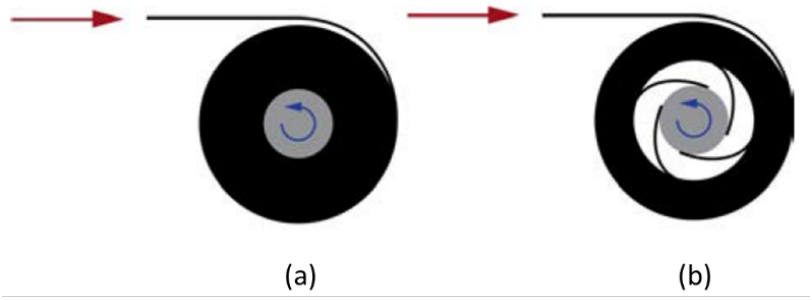

Figure 1.14: As the boom deploys, (a) the sail deployment forces cause the spiraling booms to separate, and (b) the relative motion between the adjacent booms causes the coil to expand. [61]

1.3 Contributions

The goal of this work is to create a system that will passively deorbit a small satellite from Low Earth Orbit within 25 years to reduce the probability of collisions. This will create an option for satellite designers that will easily allow them to follow the end of life guidelines. This work will have three main contributions to the state of the art.

1.3.1 Design of an aerodynamically stable, passive, deployable drag device for small satellite deorbit

This investigation describes the design of a device that can be used to passively deorbit small satellites. A key requirement for this design is to have simple mechanical and electrical interfaces to minimize the impact to the host satellite. An innovative feature of the deorbit device system is an aerodynamically stable design to ensure the maximum drag attitude is maintained during the deorbit trajectory without active attitude control. The design of the drag device is scalable so that it may be used on a range of satellite sizes to meet the 25-year deorbit guideline for circular orbit altitudes up to 1,100 km.

1.3.2 Development and laboratory testing of a 1:10 scale prototype of the drag device to demonstrate functionality

A primary goal of this system is for it to be easily scaled to accommodate different satellite masses and different orbit altitudes. This investigation describes the detailed design of a 1:10 scale version of the system as well as the conceptual design of the system sized to deorbit the baseline satellite configuration. Three component prototypes are built and tested to verify the subsystems of the passively stable pyramid sail. The boom deployer mechanism is built to ensure that friction is reduced and blossoming controlled. A test is conducted to evaluate the procedure for the deployment of the sail quadrants. This also provides data on how to mount the sail and the forces required to deploy the sail. Testing is conducted on how to package the sails and booms in the chosen secondary payload volume.

1.3.3 Characterization of SHEARLESS Booms

SHEARLESS booms are comprised of two tape springs that are constrained together inside a polymer sleeve. It has been shown that in bending, there is some friction between the tape springs that couple them together, and a small interaction between the tape springs and the sleeve in torsion. The amount of this effect is not known. This research investigates the mechanical properties of the SHEARLESS booms for both the 45 mm tall full scale version and the 20 mm small scale version by conducting bending and torsion testing. It is important to test both sizes and compare how the properties change when the boom size is changed.

1.4 Thesis Structure

This thesis is comprised of seven chapters. This current chapter describes the literature review and current state of the art. Chapter 2 describes the trade study that resulted in the identification of an aerodynamically stable drag sail as the preferred PMD technology.

Chapter 3 defines the driving requirements for the scalable $[PS]^2$ system followed by the analyses conducted to define the component requirements.

Chapter 4 describes the aerodynamic stability analysis conducted to investigate how an aerodynamically stable drag sail will behave in orbit. This simulation includes two phases, with and without orbital motion to clearly understand how aerodynamics and solar radiation pressure interact with the sail.

Chapter 5 focuses on the specific design of both the CubeSat-class system and the ESPA-Class System. Chapter 5 also describes the prototype testing conducted for the CubeSat-class system, which includes testing of the boom deployer and packaging verification of the sail membrane.

Chapter 6 describes the characterization of the SHEARLESS booms. This section first explains the bending and torsion testing conducted, then describes the results of the testing.

Chapter 7 completes the dissertation with a review of the findings and a list of the conclusions. It also summarizes the open issues and suggests future research topics.

CHAPTER 2

TRADE STUDY ON DRAG DEVICE CONFIGURATION

There are many different approaches to ensure that a satellite in Low Earth Orbit (LEO) will deorbit within 25 years of the end of the mission lifetime. LEO is commonly defined as altitudes approximately 300 km to 2000 km. This trade study investigates deorbit options for small satellites in circular orbits in higher altitudes in LEO (1000-1400 km) to match the mega-constellations that are currently being developed. There are at least four commercial small satellite constellations planned to provide global internet service, consisting of hundreds to thousands of satellites in LEO at altitudes ranging from 1,000-1,325 km [2, 3, 4, 62]. These constellations are summarized in Table 2.1. The OneWeb constellation consists of 900 satellites with masses of 150 kg with altitudes of 1,200 km [3, 63]. SpaceX plans on launching 4,425 satellites, with a satellite mass of about 400 kg, to a range of altitudes [64, 65]. The Boeing constellation is divided into three orbital bands, two of them are at an altitude of 1,200 km with different inclinations, and the third is 1,000 km with a near polar inclination. The intended mass of the Boeing satellites is unknown [2, 66]. The need to deorbit these microsatellites at the end of their operational lifetime is apparent since the satellites would take more than 100 years to deorbit naturally.

Table 2.1: Planned satellite constellations for global internet service

Company	**No. of Satellites**	**Satellite Mass**	**Orbit Altitude**	**Orbit Inclination**	**Reference**
OneWeb	720	150 kg	1200 km	87.9°	[3, 63]
SpaceX	4,425	400 kg	1110-1325 km	53°- 81°	[64, 65]
Boeing	2,956	unknown	1000, 1200 km	88°, 45°, 55°	[2, 66]
Telesat	117	unknown	1000, 1248 km	99.5°, 37.4°	[67]

2.1 Assumptions

The first step of this trade study was to assume the values of parameters to reduce the design space. The chosen parameters have a consistent impact on all possible solutions. The assumptions are listed in Table 2.2, with the first being that a satellite starts from a circular orbit. The second assumption is the orbit inclination is equal to 87.9°, or the value for the OneWeb constellation. This is a worst case scenario for all of the constellations in Table 2.1, because a satellite takes longer to decay in higher inclination orbits. Finally, the start date is fixed to ensure consistent analysis because of the change in atmospheric density due to the solar cycle.

Table 2.2: Trade study assumptions

Parameter	**Assumption**
Orbit Eccentricity	0
Orbit Inclination	87.9°
Deorbit Start Date	July 1, 2020

2.2 Analysis

The goal of this research is to meet international guidelines by ensuring that satellites will deorbit within 25 years [7, 8]. The five device types investigated are the five most viable deorbit options for small satellites, as described in Chapter 1: chemical propulsion, electric propulsion, electrodynamic tether, drag sails, and inflatable balloons. This analysis assumes an external module is attached to the satellite for the specific purpose of deorbiting with both propulsion options, as opposed to a system required for the primary mission objectives that is used for a deorbit burn at the end of the mission. It also assumes that the drag sail is a flat sail oriented in a maximum drag attitude, meaning the sail is oriented perpendicular to the velocity of the satellite, while the inflatable balloon is a sphere. Relative sizes of the different options compared to the standard CubeSat sizes are shown in

Table 2.3 because they provide a familiar reference.

Table 2.3: Dimensions for standard stowed volumes.

Stowed Volume	Dimensions (m)	Volume (L)	Mass (kg)
3U [68]	0.10 x 0.10 x 0.34	3.0	4
6U [69]	0.12 x 0.24 x 0.36	10.4	12
12U [69]	0.23 x 0.24 x 0.36	20.0	24
27U [69]	0.34 x 0.35 x 0.36	43.0	54

The device types are evaluated based on four main criteria: performance, reliability, impact on the primary spacecraft, and the likelihood of on-orbit impact. Performance is the ability for the device to deorbit the required spacecraft within 25 years, and it is highly dependent on the initial altitude and the mass of the spacecraft. For example, the higher the altitude and/or the greater the satellite mass, the larger the required drag area of the device or the larger the change in velocity required. Reliability is an assessment of risk in terms of the device initiating in the desired fashion and continuing in the deployed configuration for the lifetime of the deorbit device without creating more debris. Unreliability can be seen as the drag sail not fully deploying or the inflatable deflating partway through the deorbit phase due to a micrometeoroid impact. Impact on the primary satellite is assessed by measuring the mass, volume, ease of interface, and impact on the end of life condition. A device with a large impact on the spacecraft reduces the likelihood of being incorporated because the burden is too great. The final evaluation criteria is the liklihood of on-orbit impact.

2.2.1 Chemical Propulsion

Chemical propulsion is a proven technology for small satellites, and if sized correctly, can easily deorbit a small satellite within 25 years. The spacecraft performs a burn that lasts from a few seconds to a few minutes and that changes the orbit to one that will naturally decay within 25 years. This system does not increase the risk of the spacecraft to create

new debris since it does not add any surface area. The risk presents itself in the initiation reliability. A chemical propulsion deorbit system requires a fully functional satellite to control the attitude during the burn and for the duration of the burn. This is fine for a planned deorbit, but it would not work if there was a catastrophic failure on the spacecraft. This also would require the spacecraft to have a planned end of life before the satellite is expected to cease functioning, which removes the opportunity to extend the life span. If the spacecraft requires propulsion for its primary mission, this would be a good option because there would be minimal impact on the spacecraft, beyond shortening the life span, to add additional fuel. There are commerical stand-alone deorbit systems that use chemical propulsion, but for a OneWeb class satellite, the system would have masses of 22-41 kg, and volumes of 320 x 320 x 300 mm to 450 x 450 x 550 mm, depending on exact orbit and functionality [19].

2.2.2 Electric Propulsion

Electric propulsion is similar to chemical propulsion in that it does not increase the risk of the spacecraft creating new debris. The main difference is that electric propulsion produces a small amount of thrust to put the satellite on a trajectory that will deorbit within 25 years. This necessitates a burn that lasts hours or days and therefore requires the spacecraft to be functional for a significant period of time after the end of mission. Electric propulsion also requires a large power source to fuel the engine, which implies large solar panels. This system could be a good option to deorbit satellites that already require electric propulsion for their missions, but the impact on the mission timeline makes it less desirable.

2.2.3 Electrodynamic Tether

Electrodynamic tethers (EDT) are promising PMD technology for CubeSats that have a small mass and volume allowance because of their small stowed volume. Tethers are required to be long, i.e. hundreds of meters for small satellites [70] or 7.5 km for a 1500 kg

satellite [20], so there is a high risk that they will not fully deploy. These long tethers will span a broad range of orbital altitudes, which make them difficult to avoid and creates a high liklihood of collision with other satellites. This also presents the risk that the tether could be broken due to a collision. Additionally, since EDTs depend on the Lorentz-force interaction with the Earth's magnetic field to create the deorbit thrust, low-mass tethers are not very effective at inclinations over 75° because the interaction with the geomagnetic field is much weaker [20]. This shows that the performance of a tether to deorbit a spacecraft from an inclination of 87.9° is unfavorable.

2.2.4 Drag Sail

Drag sails has been proven to decrease deorbit time in flight demonstrations [25, 44]. This reduction in deorbit time is achieved by increasing the drag area, defined as the area perpendicular to the air flow. The largest concern with a drag sail's performance is that flight-proven drag sails were flat, and if uncontrolled, flat sails tend to spin up and orient edge-on to the flow direction. This tendency reduces the time averaged drag area, and limits the effectiveness of the drag sail.

In terms of reliability, the greatest concern is during deployment. Many problems could occur that would prevent the drag sail from fully deploying and creating the desired drag area, such as booms jamming in the deployer or the sails ripping or sticking. These can be mitigated by ground testing. Operational reliability is dependent on the sail remaining deployed and the sail material remaining intact. There is little risk that the booms will retract, and they will not collapse until close to reentry. It is possible for debris to collide with the sail material and create a hole, but the propagation of that hole is easily prevented with rip stops in the sail material. This also reduces the likelihood of new debris being created because the sail material will either have larger objects pass through it or bounce off. The booms, on the other hand, might cause larger objects to break up in the event of a collision, but they are relatively small compared to the sail material.

Inclusion of a drag sail will result in a small impact on a satellite. The mass and volume can be controlled with the techniques used in solar sails so that the only functionality required from the spacecraft is slight power to ensure the batteries are charged for the deployment motor and a communications channel to initiate deployment.

There are three possible procedures to initiate the deployment of a drag sail, only the first requires an active satellite. The nominal deployment method would be a command from the operators on the ground because it allows the operators to tune the lifetime of the mission in real time, reacting to how the hardware performs during the mission. The second procedure is a backup timer that will deploy the sail at a predefined time. Ideally, this timer could be updated by the ground operator. The final procedure involves a watchdog signal issued by the spacecraft; if it is interrupted, the sail is deployed. This capability must be made fail-safe to ensure that premature deployment of the drag sail cannot occur. The final design could include a combination of the three options to increase reliability.

2.2.5 Inflatable Balloon

The deorbit performance of an inflatable balloon is similar to a drag sail, although it requires significantly more surface area to create the desired drag area because this device is usually spherical. A sphere removes the concern about the satellite-device system tumbling because the drag area is the same in all directions, making its effectiveness agnostic to attitude.

In terms of reliability, inflation would not be difficult because it only depends on an inflation device and the membrane material unfolding without ripping. The biggest concern is the operational reliability due to the liklihood of deflation. This analysis assumes that the inflatable is composed entirely of a flexible, thin membrane like a drag sail membrane, which would be susceptible to micrometeoroid and debris punctures. Unlike with a drag sail, the concern is not with hole propagation, since even a small hole would allow the inflation gas to leak out and compromise the drag area. Deflation can be mitigated by using

a technique to rigidize the balloon membrane once it is inflated, but this risks creating new debris. Incoming objects would no longer bounce off or pass through a rigidized balloon while staying intact, collisions would result in a break-up event that creates new debris.

Inflatable balloons require a smaller mass of avionics than drag sails because they only require an inflation device and not boom mounting hardware, but they require almost four times as much membrane volume. This increases the risk of tears during deployment. Like drag sails, balloons do not require an active satellite to deploy, which greatly reduces the impact on the primary spacecraft.

2.3 Trade Study Results

Table 2.4 summarizes the conclusions discussed in the previous section by rating the four criteria for each device as either good, moderate, or poor by the colors green, yellow and red, respectively. In terms of performance, only the electrodynamic tether is not capable of deorbiting a OneWeb class satellite within 25 years because the inclination of the orbit is too high for the tether to be effective. All of the others will accomplish the goal if sized correctly, which is indicated by green highlighting in Table 2.4. The performance concern about the drag sail is mitigated with an aerodynamically stable design.

For initiation reliability, the drag sail and inflatable balloon are most reliable because both will deploy independent of the satellite. Chemical and electric propulsion are only reliable if the satellite is functioning.

Chemical propulsion has the highest operational reliability since it only requires a single short burn for the satellite to reach the required deorbit trajectory. Drag sails have the second highest operational reliability because ripstops prevent holes from propagating through the sail membranes. Inflatable balloons have a risk of deflation due to punctures in the membranes from micrometeroids. Electric propulsion requires a functioning satellite for the full length of burn, which can be as long as a couple years.

The two drag augmentation devices, drag sails and inflatable balloons, are less likely

Table 2.4: Summary of trade study results

	Chemical Propulsion	Electric Propulsion	Electrodynamic Tether	Drag Sail	Inflatable Balloon
Performance			a		
Initiation Reliability	b	b	c	d	
Operation Reliability		e	f		g
Collision Avoidance			h	i	i
Impact to Host S/C	j	k	l		

a For near-polar orbits with inclination >75° EDT performance is reduced
b Requires host spacecraft operability
c Risk of tether deployment failure
d Risk of sail deployment failure
e Requires functioniong host for lifetime of burn
f Risk of breaking due to collision
g Risk of deflation due to puncture
h Risk of impact with deployed tether
i Increased surface area presents higher collision probability
j Deorbit specific modules add significant mass and volume to the system
k Electric propulsion may drive requirement for increased solar panel area
l Requires power source for EDT operation

to avoid collisions than the two propulsion methods because of the required increase in surface area of the system. Neither the chemical or electric propulsion changes the outer size of the satellite when in operation.

Drag sails and inflatable balloons have similar impacts to the host spacecraft in terms of ease of interface and impact on end of life because both only need minimumal information from the host satellite and can be deployed after the spacecraft ceases functioning. The mass and volume required is also less than external propulsion systems. For example, a 150 kg spacecraft could be deorbited from 1,100 km by a drag sail with the approximate volume and mass of a 6U cubesat. An external chemical propulsion module would require a mass and volume similar to a 12U CubeSat. Much of this mass of the propulsion module is due to the hardware for the tanks, engines, etc. The impact to the host spacecraft for chemical propulsion would be minimal if the propulsion system was needed for the primary mission. For completely external systems, the increase in operational reliability of drag sails over

inflatable balloons makes a sail the best choice.

The conclusion from this assessment is that a passively stable drag sail is favored over an inflatable device because of its long-term reliability during deorbit. While chemical and electric propulsion approaches are favored from a performance standpoint, both require an operable host satellite and are therefore of a lower reliability.

CHAPTER 3
SYSTEM REQUIREMENTS AND ANALYSIS

After development of a drag sail was chosen as the baseline concept, the next phase was to determine the design requirements. The driving requirements are discussed to explain the framework for this system. The first analysis determines the required size of the drag sail to deorbit a satellite within 25 years, depending on the mass and altitude. The next analysis estimates the loads exerted on the boom during normal operations to create structural requirements. The required material and thickness of the sail membrane are determined by estimates of the effects of atmoic oxygen in the final analysis.

3.1 Driving Requirements

The "mission statement" for the $[PS]^2$ system is as follows: *The Passively Stable Pyramid Sail shall accelerate the orbital decay rate of small satellites, allowing deorbit to occur within 25 years after the end of the mission.* There are four driving requirements for the $[PS]^2$ system: (1) The system shall be scalable, capable of deorbiting a host vehicle ranging from CubeSat-class to 180 kg-class microsatellites from circular orbit altitudes of up to 1,200 km; (2) The system shall have simple, standardized mechanical and electrical interfaces with the host satellite; (3) The system shall be capable of initiating drag sail deployment either via ground command or backup timer. (4) The $[PS]^2$ shall provide passive aerodynamic stability about the maximum drag attitude when in the upper atmosphere. These driving requirements have provided the basis for the design of the $[PS]^2$ system [71].

3.1.1 Scalability

The size of the drag sail needed to deorbit a spacecraft within 25 years is highly dependent on the mass, orbital altitude, and inclination of the host satellite. Increasing mass and

altitude of the host satellites will require an increase in the drag area provided by the sail. A scalable system allows the $[PS]^2$ to be tailored to specific missions without requiring customized design processes. Table 3.1 shows the $[PS]^2$ system sizes that can be used for different classes of CubeSat and smallsat host spacecraft. While the basic design of the deorbit system is similar for CubeSat and microsatellite applications, some design changes are required. These changes will be discussed in Section III.

Table 3.1: The passively stable pyramid sail system is designed to be scalable to provide deorbit capability for CubeSat and smallsat host spacecraft.

Host Spacecraft		Passively Stable Pyramid Sail Assembly			Max Altitude for 25-year Deorbit (km)*
Spacecraft Class	Mass (kg)	Volume	Mass (kg)	Boom Length (m)	
1U CubeSat	1.33	0.5U	0.74	1.0	1,070
3U CubeSat	6	0.5U	0.74	1.0	940
6U CubeSat	12	0.5U	0.74	1.0	865
12U CubeSat	24	1.5U	3	5.0	1,225
27U CubeSat	54	3U	6	8.0	1,250
ESPA-Class	180	6U	12	10.0	1,110
SmallSat	400	6U	12	10.0	990

* Deorbit durations are calculated using the NASA Debris Analysis Software (DAS) version 2.0.2, with an assumed drag sail deployment date of June 30, 2020, and an orbit inclination of 87.9 deg.

3.1.2 Standard Interface

The drag sail assembly is required to have a standard mechanical and electrical interface with the host spacecraft in order to provide broad applicability as a deorbit system. The interfaces for each version of the $[PS]^2$ system are established to provide ease of integration with the host system, as shown in Table 3.2. For host CubeSats of the 1U or 3U form factor, the $[PS]^2$ is mechanically mounted with screws that pass through the CubeSat rails into the drag sail assembly. The $[PS]^2$ assembly includes the bottom pegs, per the CubeSat standard. For 6U, 12U, and 27U CubeSats, bolt holes are provided for hard mounting the $[PS]^2$ within the CubeSat structure. For smallsat host satellites, $[PS]^2$ will have a simple bolt-on mechanical interface to the satellite structure.

For 1U and 3U CubeSats, the electrical interface uses a flat-flex 6-position ribbon cable, with a Molex connector to the $[PS]^2$ printed circuit board. Host satellites with larger form factors will utilize a standard RS-422 interface to provide power and data connectivity with $[PS]^2$.

Table 3.2: Standard mechanical and electrical interfaces for $[PS]^2$

Host Spacecraft Class	Mechanical Interface	Electrical Interface
1U CubeSat	4 screws in each corner, attached to CubeSat rails	Molex connector to 6-position flat-flex ribbon cable
3U CubeSat	4 screws in each corner, attached to CubeSat rails	Molex connector to 6-position flat-flex ribbon cable
6U CubeSat	Bolt into CubeSat structure	RS-422
12U CubeSat	Bolt into CubeSat structure	RS-422
27U CubeSat	Bolt into CubeSat structure	RS-422
ESPA-Class Smallsat	Bolt on to satellite structure	RS-422
Smallsat	Bolt on to satellite structure	RS-422

3.1.3 Initiation of Drag Sail Deployment

The $[PS]^2$ is required to be capable of initiating drag sail deployment through a command received from the host spacecraft or based upon a stored deployment time that may be updated via ground command. The intent of this requirement is to provide the host satellite with control over deployment initiation, but ensure automated deployment in the event that the host satellite becomes inactive. A third procedure that initiates deployment is interruption of a watchdog signal issuing from the spacecraft. This capability must be made fail-safe to ensure that premature deployment of the drag sail cannot occur. The final design could include a combination of these three options to increase reliability.

For CubeSat-class deorbit systems, deployment is initiated by burnwire activation. The burnwire event allows spring-loaded doors to open, releasing booms that self-deploy due to stored strain energy. For the full-scale system for ESPA-class and larger satellites, boom deployment is motor-controlled and initiated by a command issued via the $[PS]^2$ flight computer or a watchdog signal from the spacecraft, if it is interrupted, the sail is deployed.

This capability must be made fail-safe to ensure that premature deployment of the drag sail cannot occur.

3.1.4 Passive Aerodynamic Stability

Flat drag sails tend to tumble or trim edge-on to the flow [43]. The $[PS]^2$ geometry is required to provide passive aerodynamic stability, such that the maximum drag area is presented in the flow direction. The square pyramid shape provides restoring torques when the sail is perturbed from the nominal maximum-drag orientation. Figure 3.1 shows the variables that define the configuration of the sail. The two variables that define the size and shape are the boom length, L, and the apex half-angle, ϕ. The apex half-angle is defined as the angle between one boom and the center axis, so an apex half-angle of 90° corresponds to the flat sail. The nominal value of the apex half-angle was set to ϕ = 70° after a preliminary stability analysis showed that this angle provides a good balance between stability and drag creation, which are competing goals.

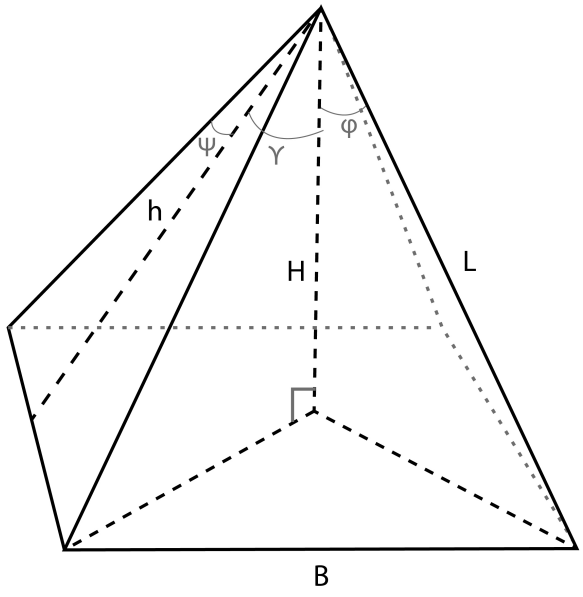

Figure 3.1: Diagram of the square pyramid sail with variable definitions [72]

3.2 Atmosphere Model

Acceleration due to atmospheric drag can be approximated by Equation (3.1), where ρ is the atmospheric density, C_D is the coefficient of drag, A_D is the cross-sectional drag area, m is the spacecraft mass, and V is the spacecraft velocity [73]. The one variable that does not depend on the configuration of the spacecraft is atmospheric density, which is very difficuly to predict because it can change up to two orders of magnitude due to variations with the solar cycle, daily change in activity, geomagnetic activity, diurnal variation, semiannual variation, and seasonal variations of the lower thermosphere and helium [73, 74]. These variations have been approximated in multiple models created from empirical observations of density [74, 75, 76]. The most significant variation is due to the solar magnetic cycle where the solar magnetic field reverses polarity approximately every 11 years. The solar 10.7 cm radio flux varies in sync with this cycle, which can be seen in Figure 3.2. This cycle heats the atmosphere, causing it to increase in density, and the peaks in F10.7 index correspond with high levels of atmospheric density, as seen in Figure 3.3 [73].

$$a_D = -\frac{1}{2}\rho C_D \frac{A_D}{m} V^2 \tag{3.1}$$

The atmospheric density of a specific altitude can be roughly approximated as decreasing exponentially as altitude increases, as shown in Equation (3.2), where ρ_0 is the density at the reference altitude, Δh is the difference between the altitudes, and h_0 is the atmospheric scale height [73]. For a higher fidelity density value, as well as for prediction, the two most commonly used models are the Jacchia 1970 model [74] or the MSISE-90 (Mass-Spectrometer Incoherent Scatter Extension) model developed by Hedin in 1990 [76]. They both strive to predict characteristics of the atmosphere based on emperical observations.

$$\rho \approx \rho_0 \exp^{-\Delta h / h_0} \tag{3.2}$$

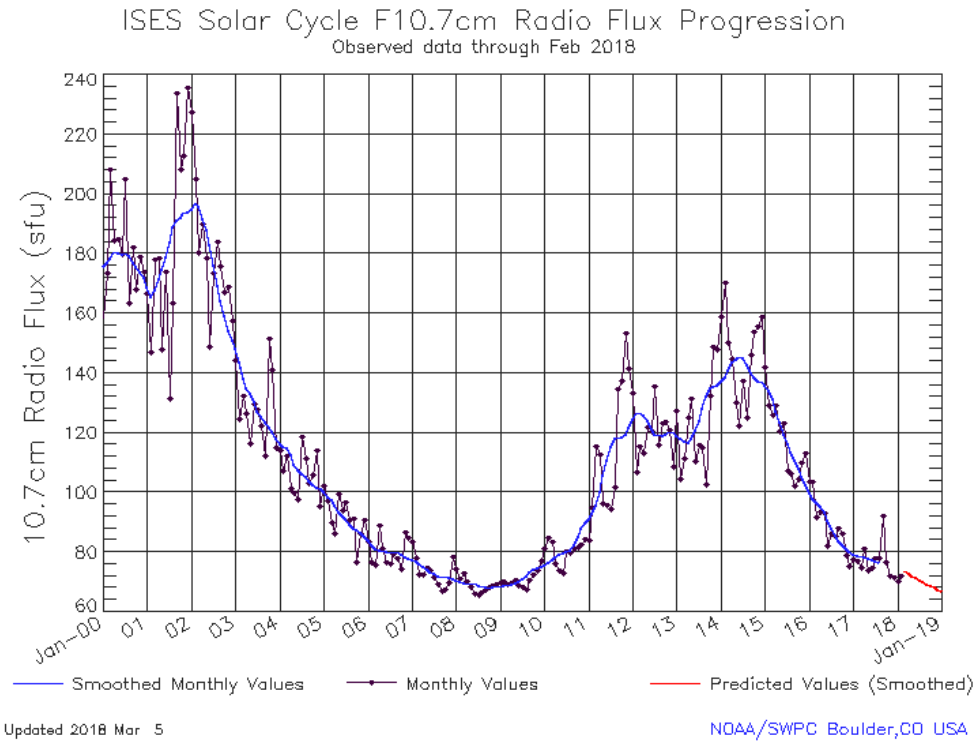

Figure 3.2: Solar Cycle F10.7 cm Radio Flux Progression from March 5, 2018 [77]

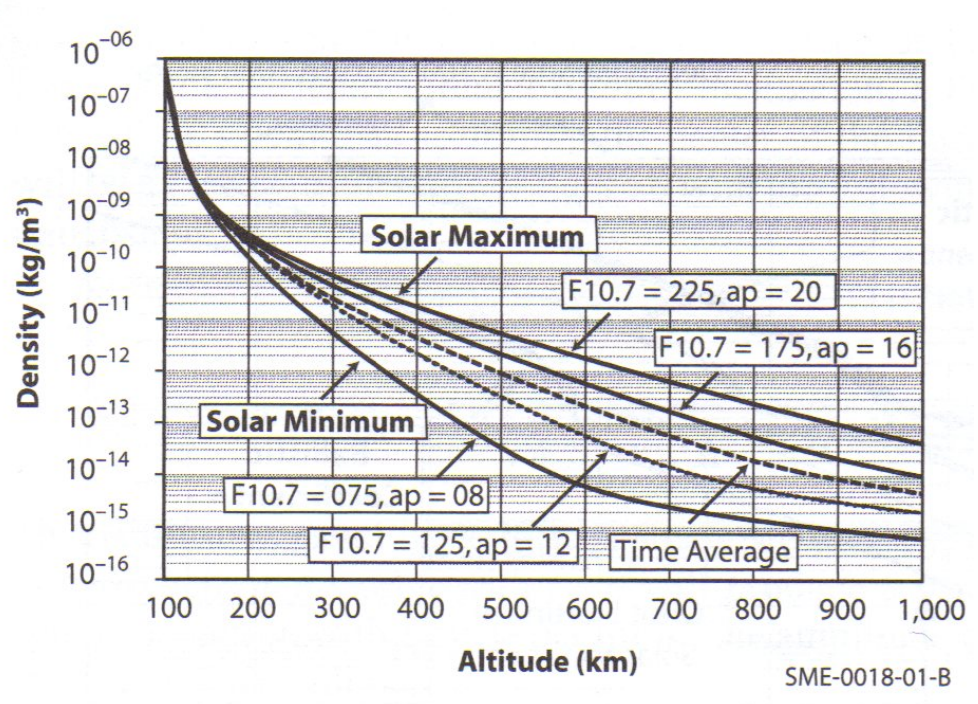

Figure 3.3: Atmospheric density vs. altitude for various F10.7 values [73]

3.3 Deorbit Analysis

A higher fidelity deorbit analysis was conducted to determine the required length of the booms in order to deorbit a satellite within the 25 year international guideline. This analysis used the General Mission Analysis Tool (GMAT), developed by NASA Goddard Space Flight Center [78], and which generally results in shorter deorbit times than the NASA Debris Analysis Software required by the FCC [79]. GMAT requires only an input of coefficient of drag, C_D, and drag area in order to propagate the orbit lifetime. A conservative value of C_D was determined using Direct Simulaton Monte Carlo (DSMC) for a pyramid sail that osciallates about the maximum drag attitude. The chosen value was C_D = 1.8, which corresponds to a pyramid with an apex half-angle of $\phi = 70°$ and a total angle of attack of 30° [80]. The satellite drag area was assumed to be the base area of the pyramid and the orbit history was simulated starting from a 1,100 km circular orbit for different boom lengths. The gravity model was set to JGM-2 of degree 4 and order 4 and the atmosphere model was MSISE-90. The stopping condition was set to 110 km altitude because that is generally the altitude where the lifetime becomes very short [73]. Figure 3.4 shows the results for the ESPA-class system with a total mass of 180 kg. A drag area of 177 m^2 is adequate to deorbit this system within 25 years, therefore, the full-scale design has 10 m long booms.

3.4 Boom Loading Analysis

This section describes the analysis to develop the structural requirements for the booms. SHEARLESS booms developed at NASA Langley were chosen because of their small volume in the stowed configuration. As shown in Figure 3.5, SHEARLESS booms are comprised of two tape springs inside of a polymer sleeve. The tape springs have the freedom to slide relative to one another within the sleeve, allowing them to be wrapped around a smaller diameter hub without damage [59]. The operational loads were estimated using a

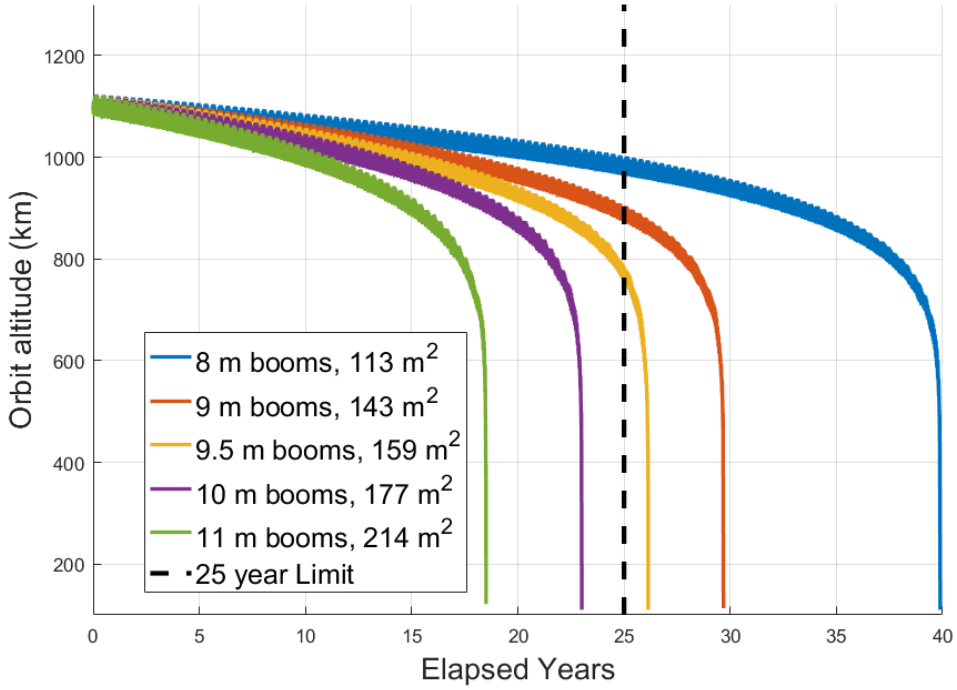

Figure 3.4: GMAT simulation results for a 180 kg satellite starting at an altitude of 1,100 km with different drag areas. Drag sail assumed to have $\phi = 70°$

procedure developed by Fernandez in 2014 [81] and modified for the square pyramid shape for this system. Then, the estimated loads were used to determine the strength requirements of the booms.

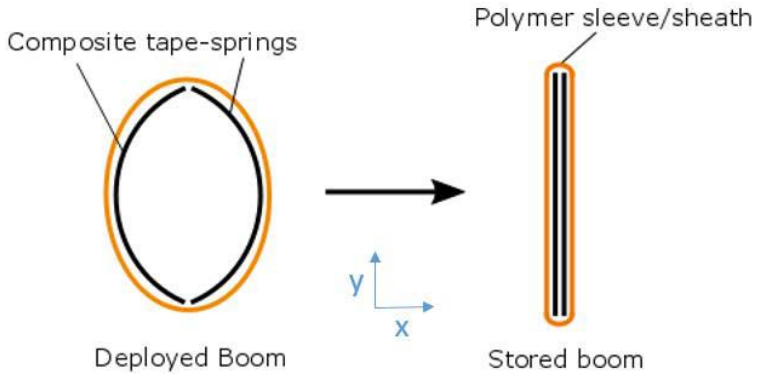

Figure 3.5: SHEARLESS boom in the stored and deployed state [59]

3.4.1 Operational Loads

The expected loads that each boom will be subjected to during normal operation while in orbit are estimated in the following sections. The boom structure needs to be able to withstand different combinations of these loads during the various phases of the mission. Two coordinate systems were used to describe the loads: the body fixed coordinate system shown in Figure 3.6, and the boom fixed coordinate system shown in Figure 3.7, where a compression load is in the positive y-direction. The boom frame is fixed to the boom between the first and fourth sail quadrants.

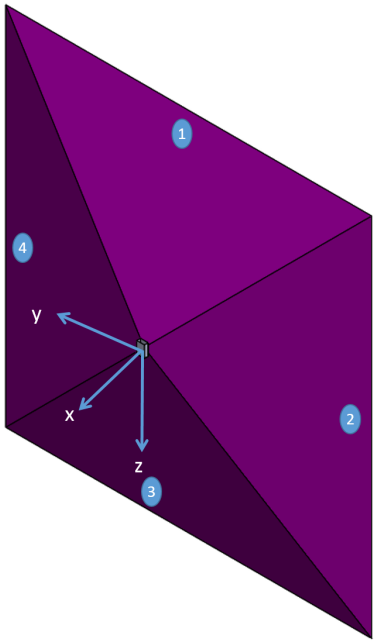

Figure 3.6: Body fixed coordinate system with sail quadrants labeled

The coordinate tranformation from the boom frame into the body frame is accomplished by two rotations, shown in Figure 3.8. The first rotation is about the b_3 axis by the apex half-angle to offset the boom from the plane of the front of the satellite to which the body frame is fixed, creating the temporary coordinate system of b_1', b_2', b_3'. The second rotation is 45° about the b_1' axis to align the sail edges with the body frame coordinate system. These rotations are described mathematically by Equation (3.3) to get the transformation matrix

Figure 3.7: Boom fixed coordinate frame used to analyze the loads.

from the boom frame to the body frame. Rotations are ordered right to left for correct matrix multiplication. To reverse the coordinate transformation, take the inverse of the rotation matrix, $C_{BN} = C_{NB}^{-1}$.

$$C_{NB} = \begin{bmatrix} 1 & 0 & 0 \\ 0 & \cos\frac{\pi}{4} & -\sin\frac{\pi}{4} \\ 0 & \sin\frac{\pi}{4} & \cos\frac{\pi}{4} \end{bmatrix} \begin{bmatrix} \cos\phi & \sin\phi & 0 \\ -\sin\phi & \cos\phi & 0 \\ 0 & 0 & 1 \end{bmatrix} \tag{3.3}$$

Sail Tension

In all membrane structures, it is important to ensure that the membrane is taut to reduce wrinkling and billowing during operation. Each sail quadrant is suspended at three points, each of the outer corners connected to a boom tip and the apex is mounted to the spacecraft itself. The tension in the sail produces reaction forces at each of these mounting points, as shown in Figure 3.9. Greschik et al. [82] proposed that the reaction forces can be approximated by assuming that the interior of an inscribed polygon is uniformly and isotropically stressed with the nominal skin stress, σ_{skin}. This stress is transferred to the corners of the membrane by Equation (3.4) where F_A is the force applied to the boom tip, t is the membrane thickenss, A is the quadrant area, s is the circumference, and α_c is the corner angle [82].

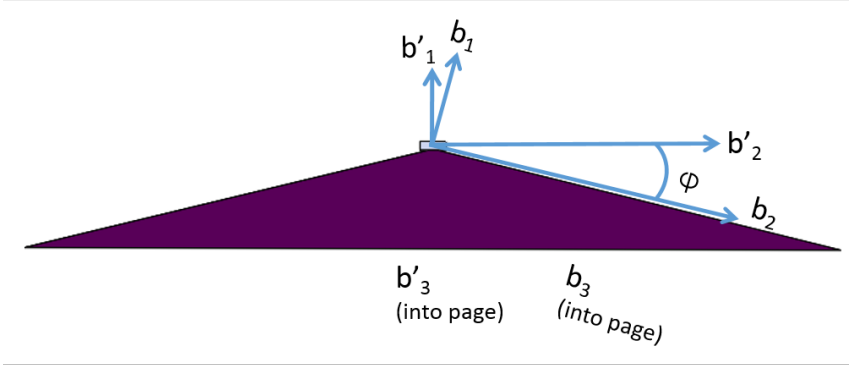

(a) First rotation about b_3 axis

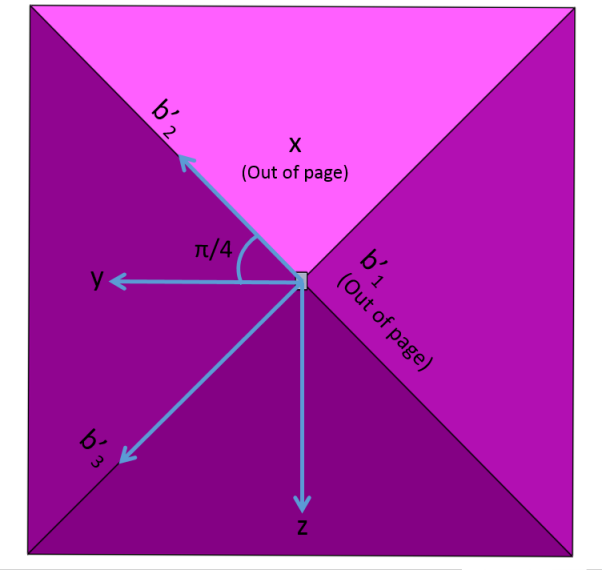

(b) Second rotation about b_1' axis

Figure 3.8: Diagrams of the two rotations required to go from the boom frame to the body frame

$$F_A = 4\sigma_{skin} t(A/s)\cos(\alpha_c/2) \tag{3.4}$$

This analysis assumes that the nominal skin stress $\sigma_{skin} = 1$ psi $= 7$ kPa. Experimental and computational analyses show that membrane stresses in solar sails generally range from $\sigma_{skin} = 1 - 5$ psi $= 7 - 35$ kPa in order to flatten membrane creases, minimize billowing, and provide general tension during thermal variations [83, 84, 85, 86, 87, 88, 89]. The low end of that range was selected because tension is a low priority for drag sails [81].

The simplifications to Equation (3.4) described by Greschik et al [82] and Fernandez

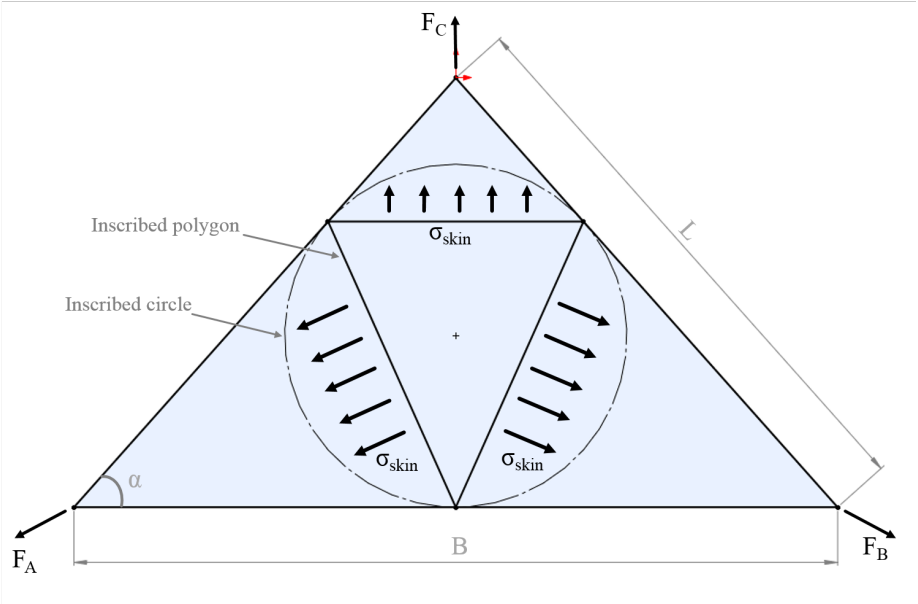

Figure 3.9: Diagram of the tensioned sail membrane with corner loads and nominal skin stress.

[81] cannot be applied in this case because they both assume a planar sail. For the $[PS]^2$ system, the membrane forces for each of the two membranes attached to a specific boom need to be rotated into the boom frame via the body frame from the plane of each sail. Figure 3.10 shows the reaction forces on the boom tips from the two sail membrane quadrants. The body frame rotation is most easily conducted using angle ψ, defined in Figure 3.10 as the angle between the plane of the sail quadrant and the bottom of the pyramid. It is also the complement of γ, as defined in Figure 3.1. Equation (3.5) describes the relationship between ψ and ϕ. Equations (3.6) and (3.7) describe the forces on the boom tip in the boom frame from sail quadrants 1 and 4, respectively.

$$\psi = \frac{\pi}{2} - \tan^{-1}\left(\frac{\sqrt{2}}{2}\frac{\sin\phi}{\cos\phi}\right) \tag{3.5}$$

$$\vec{F}_{A1}^{B} = F_A * C_{NB}^{-1} * \begin{bmatrix} \sin\frac{\alpha}{2}\cos\psi \\ \cos\frac{\alpha}{2} \\ \sin\frac{\alpha}{2}\sin\psi \end{bmatrix} \tag{3.6}$$

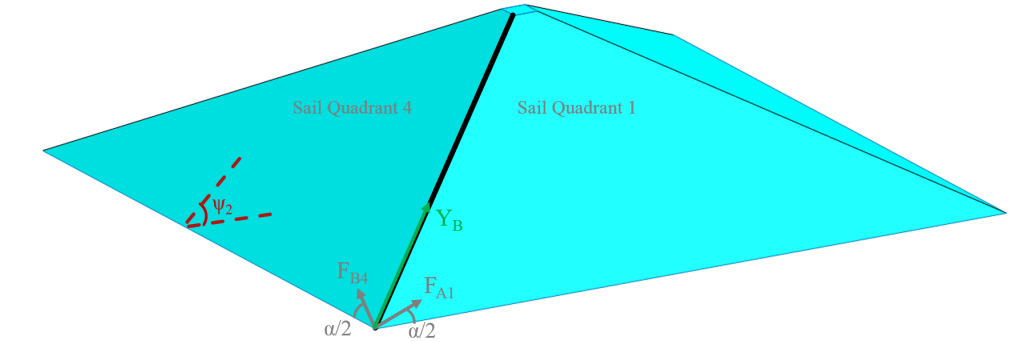

Figure 3.10: The reaction forces on the boom tip from two sail membrane quadrants.

$$\vec{F}_{B4}^{B} = F_A * C_{NB}^{-1} * \begin{bmatrix} \sin\frac{\alpha}{2}\cos\psi \\ \sin\frac{\alpha}{2}\sin\psi \\ \cos\frac{\alpha}{2} \end{bmatrix} \tag{3.7}$$

To calculate the bending moments, both forces have the same lever arm given by:

$$\vec{d} = \begin{bmatrix} 0 \\ -L \\ 0 \end{bmatrix} \tag{3.8}$$

So, the total forces and bending moments due to sail tension can be calculated as:

$$\vec{F_{ST}} = \vec{F_{A1}^{B}} + \vec{F_{B4}^{B}} \tag{3.9}$$

$$\vec{M}_{ST} = \vec{d} \times \vec{F}_{A1}^{B} + \vec{d} \times \vec{F}_{B4}^{B} \tag{3.10}$$

Aerodynamic Drag Force

Aerodynamic drag force is the external force being harnessed to deorbit the host spacecraft, therefore it will be the largest load experienced by the sail. In LEO, the aerodynamic forces experienced by the spacecraft are in the free molecular flow regime, also known as

rarefied aerodynamics, which is characterized by a density low enough that the continuum assumption is no longer valid [90]. Fernandez assumed a simplified drag force model by multiplying Equation (3.1) by spacecraft mass [81]. For the $[PS]^2$ system, the higher fidelity approximation used in the stability analysis described in Chapter 5 is used instead. This approach integrates the coefficients of pressure and shear pressure described by Hart et al. [90] over the surface of sail quadrants 1 and 4 to calculate the aerodynamic forces in the body frame. For each sail quadrant, the aerodynamic forces are divided by 3 to account for equal loading on the three mounting points, then they are rotated and combined into forces and moments in the boom frame in the procedure described in the previous section.

For the purpose of creating requirements, the loads should be worst case scenario for nominal activity in order to ensure the system survives, and for this case there are two factors: altitude and attitude. Drag force increases as the altitude decreases because the density of the atmosphere increases, therefore the worst case altitude is the lowest operational altitude for the system. As mentioned previously, an altitude of 110 km is generally agreed to be the end of a satellite's orbital lifetime and the beginning of its re-entry phase.

The worst case attitude is the attitude where the force in each direction is a maximum. This was not discussed by Fernandez [81] because for a flat sail, the worst case is also the maximum drag attitude where the sail is perpendicular to the flow. The forces on the boom were calculated for all three orientation angles ranging from 0° - 90°. It was quickly determined that rotating about the x-axis 45°(θ_1) would align the boom in question with the axes so rotations in the other directions will ensure the flow is more directly acting on the boom. The forces and moments about each axis were plotted to find the values of rotation about y-axis (θ_2) and z-axis (θ_3) to maximize the values. Figures 3.11 and 3.12 show the forces that were large enough to be significant; the others either were orders of magnitude smaller or did not vary with the angles. The x-force has the largest value when $\theta_2 = 10°$ and $\theta_3 = 0°$, called Case 1. The maximum y-force is when $\theta_2 = 0°$ and $\theta_3 = 45°$, called Case 2. The forces and moments were calculated at both locations.

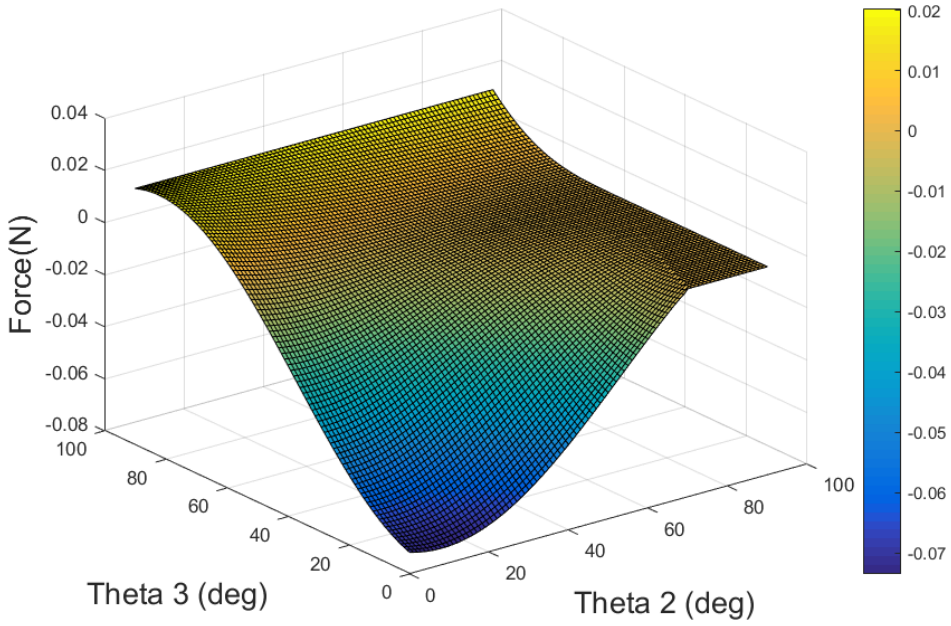

Figure 3.11: The forces in the x-direction with varied rotations about the y and z axes.

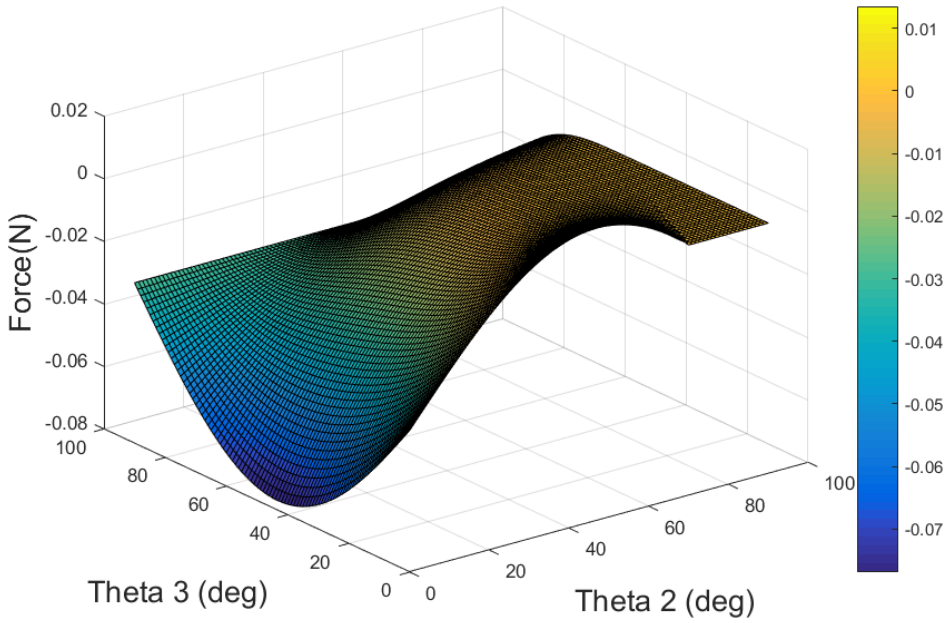

Figure 3.12: The forces in the y-direction with varied rotations about the y and z axes.

Solar Radiation Force

Force from solar radiation pressure on the sail was also calculated by using the equations that will be discussed in Chapter 5, but in agreement with the assessment by Fernandez [81]. This force is not large enough to be significant from a boom loading persepctive, especially since the sail membrane will be transparent to reduce its impact on stability.

Thermo-elastic Loads

Thermal variations are a concern for all spacecraft designers, especially for large appendages like drag sails. One concern involves the difference in the coefficient of thermal expansion (CTE) between the booms and the sail membrane. This has resulted in the common practice of using extension springs to mount the membrane to the booms in order to account for thermal variations in the sail size [61, 46, 91, 92].

This change in membrane size imparts a load on the boom tips that depends on the maximum temperature change, ΔT_{max}, defined as the difference between the hot and cold cases. This value can be calculated from a detailed orbit thermal analysis, but McInnes derived an equation to estimate the sail temperature in sunlight based on attitude [93]. This equation assumes the sail does not transmit light, which is valid for reflective solar sails. In the case of drag sails, a transparent membrane is a valid design solution, so the following equations are defined in terms of the membrane absorptance, $\tilde{\alpha}$, instead of reflectance, $\tilde{r}$. The variables are defined in Table 3.3.

$$T_{sun} = [\frac{\tilde{\alpha}}{\varepsilon_f + \varepsilon_b} \frac{W_E}{\sigma_{SB}} (\frac{R_E}{r})^2 \cos\theta_{ss}]^{1/4} \tag{3.11}$$

For a conservative value of the thermo-elastic loads, the maximum largest value of temperature change is desired. Equation (3.11) was calculated for a range of pitch angles (θ_{ss}) and the maximum value was taken as T_{max}. The lowest temperatures a drag sail experiences is when it is in eclipse behind the Earth. Fernandez modified Equation (3.11)

to calculate this temperature [61] as shown in Equation (3.12) where F_{12} is the view factor between the sail's surface and Earth's surface. The view factor was varied between 0 and 1, then the lowest temperature value was taken as T_{min}.

$$T_{shadow} = [\frac{\tilde{\alpha}}{\varepsilon_f + \varepsilon_b} \frac{Q_E F_{12}}{\sigma_{SB}}]^{1/4} \tag{3.12}$$

Table 3.3: Parameters used for the thermo-elastic load analysis

Property	Values Used
Solar Energy Flux at Earth (W_E)	1368 $\frac{J}{m^2-s}$
Energy Flux emitted from Earth (Q_E)	236 W/m^2
Stefan- Boltzman Constant (σ_{SB})	$5.670\,367 \times 10^{-8}$ $\frac{W}{m^2-K^4}$
Distance from Sun to Earth (R_E)	149597870 km
Distance from Sun to sail (r)	149597620 km
Absorptance of the sail ($\tilde{\alpha}$)	0.0579
Surface Emissivity of front of the Sail (ε_f)	0.29
Surface Emissivity of back of the Sail (ε_b)	0.29
Pitch angle of sail relative to the sun line (θ_{ss})	0°- 90°

Once ΔT_{max} was estimated, the change in the length of the sail membrane can be calculated, assuming it is an isotropic material with a constant coefficient of thermal expansion, $\alpha_{s,CTE}$. This change of length is described by Equation (3.13), where L is the boom length.

$$\Delta L_{TH} = L\alpha_{sCTE}\Delta T_{max} \tag{3.13}$$

This change in sail length is imparted to the boom tip, assuming the extension spring used to mount the sail will extend the same distance. The worst case scenario is the cold case, therefore if this spring has a spring constant K_{sp}, the force on the tip of the boom can be expressed by Equation (3.14).

$$F_{TH} = F_{cold} = \Delta L_{TH} K_{sp} \tag{3.14}$$

Thermally-Induced Bending Moment

Another concern is the thermal variation within the booms themselves due to unequal heating, causing the booms to deflect a noticable amount due to their slenderness. Stolhman and Loper investigated thermal deflections on carbon fiber and elgiloy TRAC booms and showed that the deflections due to thermal variation can be significant, with carbon fiber booms experiencing a noticeably smaller thermally induced curvature [56]. This section utilizes the process derived by Fernandez [61] to calculate the steady state bending moment imparted on a carbon fiber boom due to thermal variation.

The following equations calculate the thermal bending moment for the specific case of a boom under a tip load. The boom is modeled as a thin walled cylinder of radius R_{sh} and wall thickness t_{sh}. This is a good assumption for SHEARLESS booms, with R_{sh} being the shell radius, since they have an approximately circular cross section. The thermal model assumes one dimensional conduction around the circumference and heat loss on the external surface due to radiation. An approximate solution for the steady state temperature is given by Equation (3.15) with the thermal time constant of a tube being defined by Equation (3.16).

$$\Delta T_{SS} = \frac{\tilde{\alpha}_{cf} S_0 \tau_{tube}}{\rho c t_{sh}} \tag{3.15}$$

$$\tau_{tube} = \left[(k/\rho c R_{sh}^2) + (4\sigma_{SB}\varepsilon_{em}/\rho c t_{sh}) \cdot (\tilde{\alpha}_{cf} S_0 / \pi \sigma_{SB} \varepsilon_{em})^{3/4} \right]^{-1} \tag{3.16}$$

Equation (3.17) describes the steady state moment due to thermal heating, which was obtained by integrating Equation (3.15) over the cross section of the boom. Table 3.4 defines and lists the values of the parameters used in this analysis, assuming the boom to be uncoated carbon fiber reinforced polymer. The solar heat flux value assumes the worst

case scenario of the Sun's rays striking parallel to the boom normal [61].

$$M_{TH_{SS}} = \frac{1}{2}\pi E \alpha_{cf,CTE} t_{sh} R_{sh}^2 \Delta T_{SS} \tag{3.17}$$

Table 3.4: Properties of a flexible carbon fiber reinforced polymer boom [61]

Property	Value used for CFRP
Solar Heat Flux (S_0)	1357 W/m^2
Stefan-Boltzman Constant (σ_{SB})	$5.670\,367 \times 10^{-8}$ $\frac{W}{m^2-K^4}$
Tube Wall Thickness (t_{sh})	0.215 mm
Cross-Sectional Tube Radius (R_{Sh})	19 mm
Density of CFRP (ρ)	1592 kg/m^3
Surface Absorbtivity ($\tilde{\alpha}_{cf}$)	0.95
Surface Emissivity (ε_{em})	0.88
Thermal Conductivity (k)	22 $\frac{W}{m-K}$
Coefficient of Thermal Expansion ($\alpha_{cf,CTE}$)	2.1
Specific Heat Capacity (c)	674 $\frac{J}{kg-K}$
Young's Modulus (E)	167 GPa

Deployment Loads

Deployment is another phase of the mission that places significant loads on a drag sail. Loads arise when the sail resists being unfolded due to the booms extending. The actual loads imparted are not well understood because of the complications involved in replicating deployment on the ground for measurment purposes. These complications include air resistance, offloading the gravity of the system, and frictional forces in the setup. In his deployment load formulation, Fernandez assumes a quasi-static deployment where the deployment is very slow and the satellite is stationary [81]. For larger versions of the $[PS]^2$ the deployment will be controlled by a motor, so the speed of the deployment is valid, but the stationary satellite assumption might not be true. A higher fidelity simulation of the deployment should be conducted in the future.

Arya and Pellegrino [94] developed a procedure to measure the deployment loads in a quasi-static deployment in which they packaged the membrane around a central supporting

hub and replaced the booms with synchronized linear postioners to provide the deployment forces. Their two main conclusions. First, thinner membranes will require larger deployment forces because electro-static forces cause the layers of the membrane to stick together. This also causes the deployment to be asymmetric. Second, they concluded that there are two phases to a deployment: the initial phase with low but variable stiffness and the final phase with higher stiffness as the tension of the membrane begins to take effect. Thicker (25 μm) membranes generally behave like plates, while thinner (7.5 μm) membranes display membrane behavior.

The method to estimate deployment forces described by Fernandez uses a similar procedure to the procedure derived for tension described in Equations (3.6) - (3.10). The difference is that the corner angle, α_c, is replaced by a halyard angle, α_{haly}, that is defined in terms of instantaneous boom length throughout the deployment as seen in Equation (3.18). α_{haly_0} is the initial halyard angle and c is a parameter that determines the final halyard angle α_{haly_f} as defined by Equation (3.19).

$$\alpha_{haly}(t) = \alpha_{haly_0} + cL(t) \tag{3.18}$$

$$c = (\alpha_{haly_f} - \alpha_{haly_0})/L \tag{3.19}$$

The behavior of the deployment force is solved by iterating over an increasing boom length to display how the forces and moment develop. Figure 3.13 shows the forces and moments calculated using L = 10 m, α_{haly_0} = 5°, and α_{haly_f} is the corner angle defined by Greschik [82]. The small magnitude of the force in the z-direction is the result of the force from each of the two sail quadrants cancelling out.

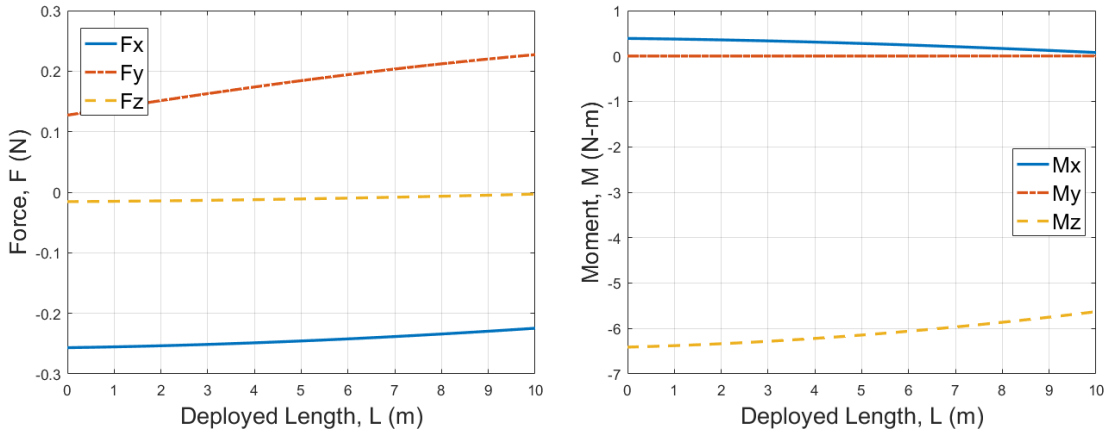

(a) Deployment forces (b) Deployment moments

Figure 3.13: Simulated force components (a) and bending moment components (b) during sail deployment plotted over the length of the boom, 10 m.

Design Load Cases

In order to calculate the ultimate loads that a boom will encounter in operation, the loads discussed in this section need to be combined into load cases because the $[PS]^2$ will not encounter all of the loads at one time.

Loads were calculated for the ESPA-class $[PS]^2$ with a factor of safety of 2.5. The ESPA-class system has an apex half-angle of $\phi = 70°$ and boom length of $L = 10$ m. The sail membrane is assumed to be transparent Corin with a nominal skin stress of $\sigma_{skin} = 7$ kPa, membrane thickness of $t = 5$ µm, absorptance of $\tilde{\alpha} = 0.0579$, and coefficient of thermal expansion of $\alpha_{s,CTE} = 68 \times 10^{-6}$ ppm/°C. The spring constant for the mounting springs was assumed to be $K_{sp} = 0.0226$ N-m. Table 3.4 shows the properties of carbon fiber booms, Table 3.5 summarizes the forces and moments, and Table 3.6 explains the moments for the combined load cases.

3.4.2 Boom Structural Requirements

Structural requirements for slender booms usually come in the form of axial, bending, and torsional stiffness in four main quantities: EA, EI_{xx}, EI_{yy}, and GJ_x. These provide

Table 3.5: Summary of the loads experienced by a drag sail with 10 m long booms, 70° apex half-angle, and clear sail membrane.

Label	Description	F_x (mN)	F_y (mN)	F_z (mN)	M_x (mN-m)	M_y (mN-m)	M_z (mN-m)
A	Sail tensioning	-568.73	570.62	0.00	0.00	0.00	-5701.73
B	Aerodynamic Drag (Case 1)	-183.50	-47.70	0.00	0.00	0.00	-1822.75
C	Aerodynamic Drag (Case 2)	-34.16	-191.95	0.00	0.00	0.00	-325.95
D	Solar Radiation Pressure	0.04	0.05	-0.02	0.17	-0.00	0.42
E	Thermal-Elastic (Cold case)*	-10.32	10.35	0.00	0.00	0.00	-103.43
F	Thermal-Elastic (Hot Case)**	0.00	0.00	0.00	0.00	0.00	-7.27
G	Deployment (Final loads)	-561.52	568.00	-7.68	76.54	0.15	-5629.75

* No thermal bending

** Thermal-induced bending only

Table 3.6: Combined loading cases for a drag sail with 10 m long booms, 70° apex half-angle, and clear sail membrane

Situation	Cases	M_x (mN-m)	M_y (mN-m)	M_z (mN-m)
Deployment in Sun	F+G	76.54	-0.152	-5637.01
Deployment in Shadow	G	76.54	-0.152	-5629.74
Operational in Sun (1)	A+B+D+F	0.17	-0.002	-7531.33
Operational in Sun (2)	A+C+D+F	0.17	-0.002	-7627.49
Operational in Shadow (1)	A+B+D+E	0.17	-0.002	-6034.52
Operational in Shadow (2)	A+C+D+E	0.17	-0.002	-6130.68

parameters for minimum stiffness to ensure the booms will survive the required loads. This section will describe a method for calculating the critical loads where the booms will fail and compare them to the required loads calculated in the previous section. Then, the results of this method will be discussed for the CubeSat-class and ESPA-class missions.

Description

The goal of this analysis is to create system level requirements and calculate a margin of safety for the design to enable preliminary dimensioning of the booms. For the structural design, the loads primarily responsible for failure are the in-plane and out-of-plane bending moments and the axial compression force (M_x, M_z, F_y). An estimate of the failure in these directions can be made using a unidirectional buckling analysis. Therefore, following the

procedure described by Fernandez [81], a boom failure criterion will be defined for system level requirements and a calculation of a margin of safety of the design. The maximum loading envelope will take the form of an ellipsoid with the critical loads ($M_{x,crit}$, $F_{y,crit}$, $M_{z,crit}$) as the semi-principal axes. To enforce consistent units, it is important to replace the compression force with a virtual moment that has a unit lever arm, $M_{y,crit} = F_{y,crit} * 1$ [81].

The first step is to determine the minimum loads that the booms are required to withstand. As Table 3.6 demonstrates, the largest in-plane bending moment (M_x) is experienced during the deployment of the sail, regardless of lighting. The largest out-of-plane bending moment (M_z) is experienced during nominal operation in the sunlight with an attitude of $\theta_1 = \theta_3 = 45°$ and $\theta_2 = 0°$. The torsional moment (M_y) is negligible. The bending strength requirements for the ESPA-class system are: $M_{x,req} = 0.076$ N-m, $M_{y,req} = 1.5x10^{-4}$ N-m, and $M_{z,req} = 7.627$ N-m.

The failure ellipsoid is represented in M_x-M_y-M_z space with $M_{x,crit}$, $M_{y,crit}$, $M_{z,crit}$ being the semi-principal axes of the ellipse (a,b,c). Therefore, the equation of the ellipse is defined by Equation (3.20). A factor of safety (FoS) can be introduced by dividing each critical moment by the value to shrink the failure ellipse, and therefore the design space.

$$\frac{M_x^2}{M_{x,crit}^2} + \frac{M_y^2}{M_{y,crit}^2} + \frac{M_z^2}{M_{z,crit}^2} = 1 \tag{3.20}$$

To verify the design meets the requirements, the required loading envelope can be plotted in the M_x-M_y-M_z space as a parallelepiped where the corner locations are the required bending moment values as shown in Figure 3.14. If all four of the corners are located within the failure ellipse, the design is valid. Figure 3.15 demonstrates that the design is valid for a FoS of 1, but not 2.5, specifially looking at the isometric view and the M_y vs. M_x view on the top left. In order to visually demonstrate this, the values of $M_{x,crit}$, $M_{y,crit}$, $M_{z,crit}$ were arbitrarily chosen since the actual critical values are orders of magnitude larger than the required values [81].

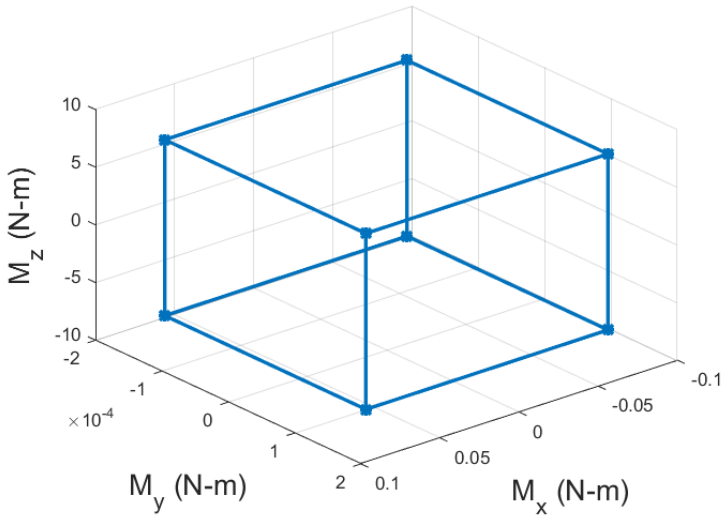

Figure 3.14: The required bending moment parallepiped for the ESPA-class $[PS]^2$.

It is possible to quantify the distance between the required loads and the failure ellipse, known as the Margin of Safety (MoS). First, one must determine the constant, p, to multiply the required moments vector by in order to intersect with the failure ellipse. To solve for this, multiply the left hand side of Equation (3.20) by the square of the FoS and the multiplier constant p, as shown in Equation (3.21) [81].

$$\frac{M_x^2 FoS^2 p^2}{M_{x,crit}^2 FoS^2 p^2} + \frac{M_y^2 FoS^2 p^2}{M_{y,crit}^2} + \frac{M_z^2 FoS^2 p^2}{M_{z,crit}^2} = 1 \tag{3.21}$$

Find a common denominator and solve for p to get Equation (3.22). The convention for MoS is for positive values to designate valid designs and negative values to designate invalid designs. This is achieved by $MoS = p - 1$, consequently, MoS is defined by Equation (3.23) and can be multiplied by 100 to yield a percentage value [81]. For the example case shown in Figure 3.15, the MoS for FoS = 1 is 1.27 or 127% and for FoS = 2.5, MoS = -0.63 or 63%.

$$p = \sqrt{\frac{M_{x,crit}^2 M_{y,crit}^2 M_{z,crit}^2}{FoS^2 (M_x^2 M_{y,crit}^2 M_{z,crit}^2 + M_y^2 M_{x,crit}^2 M_{z,crit}^2 + M_z^2 M_{x,crit}^2 M_{y,crit}^2)}} \tag{3.22}$$

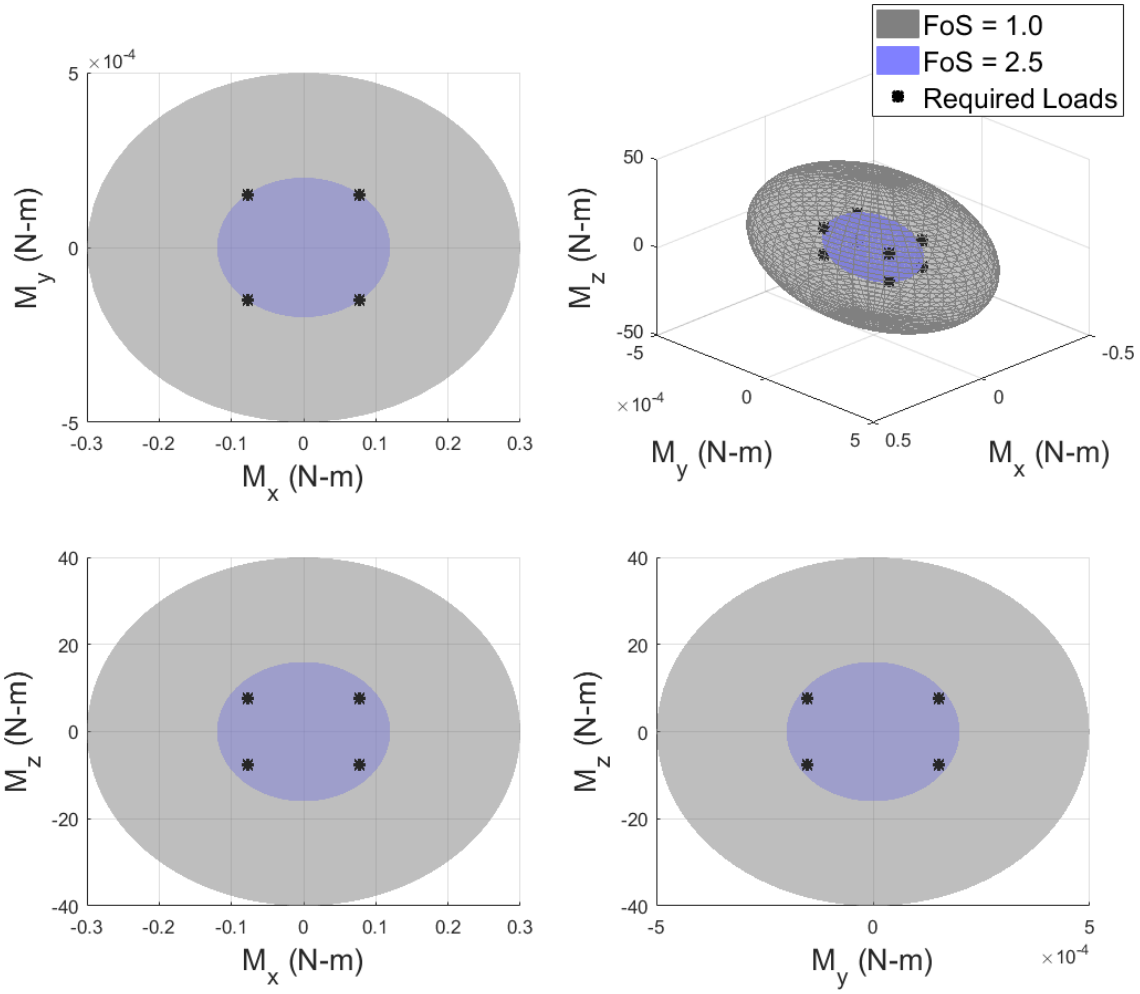

Figure 3.15: The required bending moment parallepiped inside the example failure ellipse for two different FoS values.

$$MoS = \sqrt{\frac{M_{x,crit}^2 M_{y,crit}^2 M_{z,crit}^2}{FoS^2(M_x^2 M_{y,crit}^2 M_{z,crit}^2 + M_y^2 M_{x,crit}^2 M_{z,crit}^2 + M_z^2 M_{x,crit}^2 M_{y,crit}^2)}} - 1 \quad (3.23)$$

Results

SHEARLESS booms were chosen for the $[PS]^2$ system mainly for stowed volume constraints which fixed the stowed height for both the ESPA-class and CubeSat-class systems. This analysis was used to select the cross-section and verify that the stiffness of the chosen booms was adequate. This section describes the procedure used to calculate the critical

bending moment values for SHEARLESS booms, shows the actual failure ellipsoid for the ESPA-class system, and shows the results of this analysis for the CubeSat-class system.

As mentioned previously, the three loads that are the most likely to cause the boom to fail are M_x, M_z, and F_y. The first two will cause failure when the stress due to bending is greater than the yield stress. The third is a compressive load which can cause the compressive stress to exceed the yield stress or bend the beam sideways, also known as buckling. For long slender beams like the booms in this case, buckling causes failure much sooner than compressive stress.

Bending stiffness is defined as EI, or Young's modulus times moment of inertia. The first quantity is a material property, the second is based on geometry. The Young's modulus of the carbon fiber composite used for the SHEARLESS booms is E = 51.0×10^9 Pa[1]. The moments of inertia were calculated using the equations developed by Fernandez [59] and the coordinate system from Figure 3.7, so $I_{xx} = I_{11}$ and $I_{yy} = I_{33}$ as shown in Equations (3.25) and (3.24), where R_{sh} is the radius of one tape spring half, t_{sh} is the thickness of the tape spring half, and α_{sh} is the subtended angle of the tape spring. For the ESPA-class system, $R_{sh} = 19$ mm, $t_{sh} = 0.215$ mm, and $\alpha_{sh} = 135.7°$.

$$I_{11} = R_{sh}^3 t_{sh}[\alpha_{sh} - \sin\alpha_{sh}] \tag{3.24}$$

$$I_{33} = 2R_{sh}^3 t_{sh}[\frac{\alpha_{sh} + \sin\alpha_{sh}}{2} - \frac{2 - \cos\alpha_{sh}}{\alpha_{sh}} + \alpha_{sh}\{\frac{\sin(\alpha_{sh}/2)}{(\alpha_{sh}/2)} - cos(\alpha_{sh}/2)\}] \tag{3.25}$$

Stress due to bending is calculated by the flexure formula, which can be solved for the critical moment to get Equation (3.26) where σ_a is the allowable stress (yield stress divided by the factor of safety), and c is the distance from the center of the boom to the edge in the direction the force is applied [95]. For $M_{x,crit}$, the variables used are I_{11} and c_z. For

[1]Value provided in personal communication from Juan Fernandez of NASA Langley Research Center.

$M_{z,crit}$, the variables are I_{33} and c_x.

$$M_{crit} = \frac{\sigma_a I}{c} \tag{3.26}$$

The critical load where a beam will start to buckle is shown in Equation (3.27), where k is the non-dimensional buckling parameter that is determined by the end conditions of the beam. In this case, the boom was assumed to have one end clamped and one end free so $k = 1/4$ [95].

$$F_{y,crit} = k\pi^2 \frac{EI_{33}}{L^2} \tag{3.27}$$

Using the values discussed throughout this section, the values for $M_{x,crit}$, $M_{y,crit}$, and $M_{z,crit}$ for the ESPA-class system can be calculated. Figure 3.16 shows the failure ellipse created using the actual critical values, and all of the required values appear on top of each other meaning, that the boom is over-designed in case there are unexpected loads experienced during the lifetime of the system.

For the CubeSat-class system, there are only a few differences that affect the calculations discussed in this section. The boom length is shorter, $L = 1$ m; the boom cross section is smaller, $R_{sh} = 8$ mm, $t_{sh} = 0.215$ mm, and $\alpha_{sh} = 138.33°$; and finally, the sail membrane material is CP1 instead of Corin, so the coeffient of thermal expansion is $\alpha_{CTE,CP1} = 51x10^{-5}$ ppm/°C. Table 3.7 shows the combined load cases and Figure 3.17 shows the failure ellipse. Once again, it is obvious that the MoS is significantly large.

3.5 Sail Membrane Thickness Requirements

Deployable thin membrane structures are attractive for applications like solar and drag sails because the majority of the deployed area is created by the lightweight and thin membranes with a high packing efficiency. The thickness can range between 2.5 - 25 μm. Polymers commonly used for this purpose are normally abreviated and also referred to by their

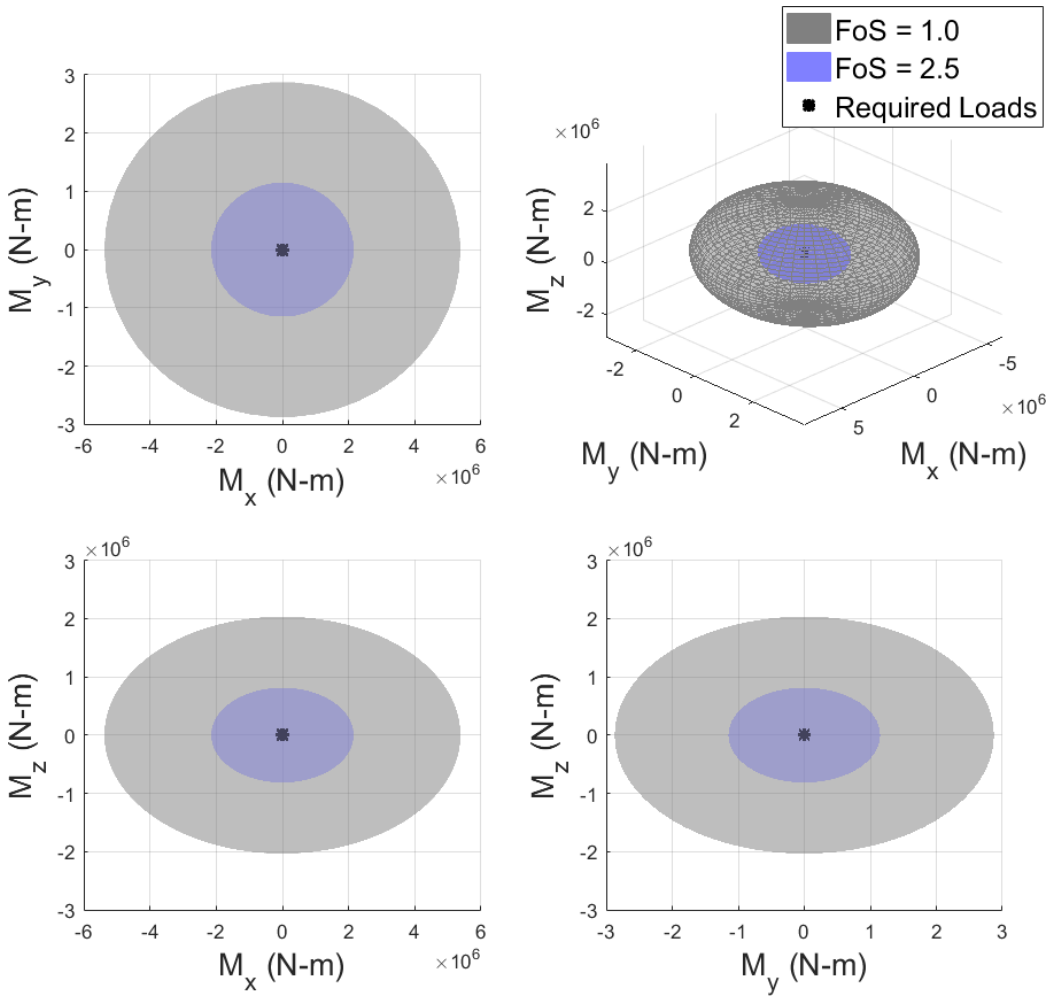

Figure 3.16: The required bending moment parallepiped for the ESPA-class $[PS]^2$ inside the actual failure ellipse for two different FoS values.

Table 3.7: Combined loading cases for a drag sail with 1 m long booms, 70° apex half-angle, and clear sail membrane

Situation	Cases	M_x (mN-m)	M_y (mN-m)	M_z (mN-m)
Deployment in Sun	F+G	0.7458	-0.0152	-57.9046
Deployment in Shadow	G	0.7458	-0.0152	-57.6074
Operational in Sun (1)	A+B+D+F	0.0002	-2.28e-5	-60.3228
Operational in Sun (2)	A+C+D+F	0.0002	-2.28e-5	-60.8189
Operational in Shadow (1)	A+B+D+E	0.0002	-2.28e-5	-58.7956
Operational in Shadow (2)	A+C+D+E	0.0002	-2.28e-5	-59.2917

registered trade names: Polyethylene terephthalate (Mylar®), Polyimide or PI (Kapton®, LARC™ CP1, Corin®), Polycarbonate or PC (Lexan®), Polyethylene naphthalate or PEN

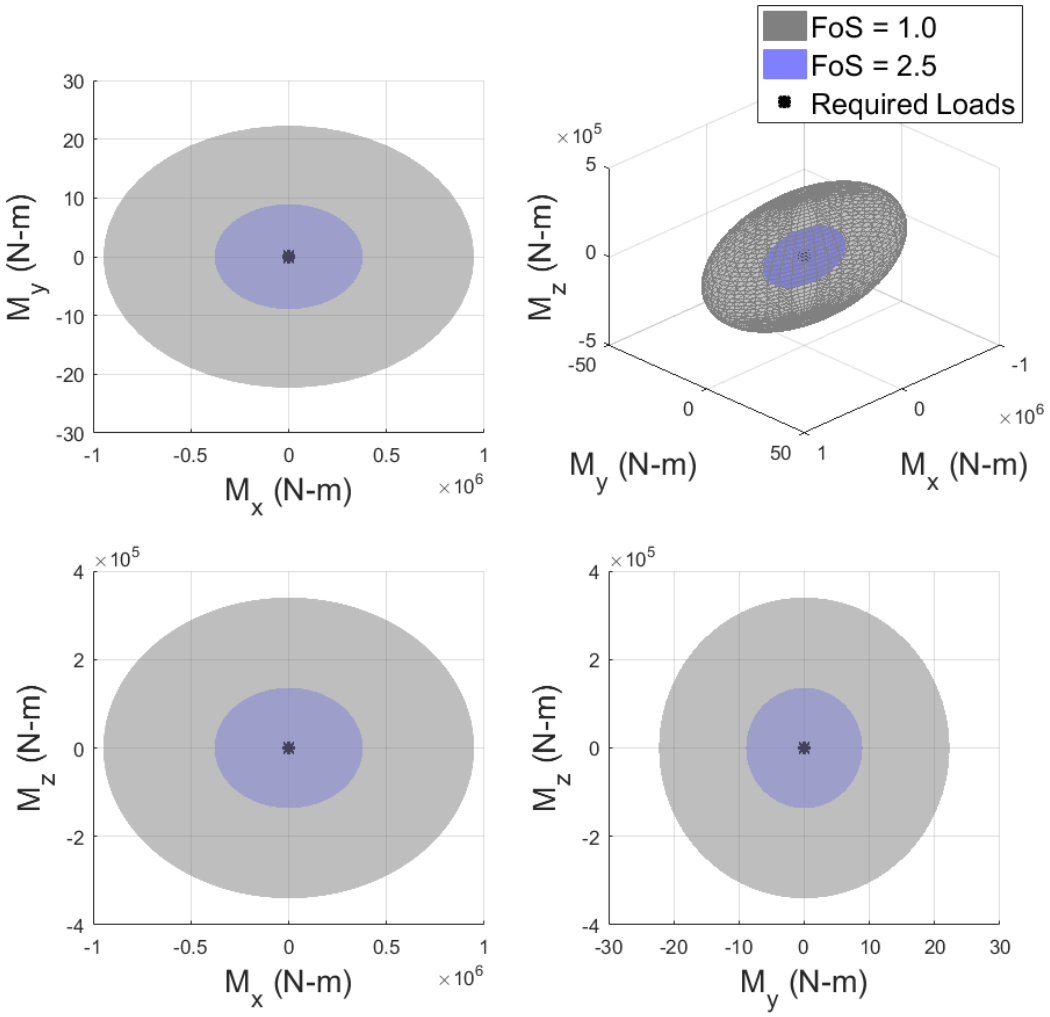

Figure 3.17: The required bending moment parallepiped for the CubeSat-class $[PS]^2$ inside the actual failure ellipse for two different FoS values.

(Teonex®), etc. [61]. The most commonly used are the first four, which will be referred to by their trade names: Mylar, Kapton, CP1, and Corin. While CP1, Kapton, and Corin are all polymides, the chemistry is slightly different, which changes some of their material properties and their price [96, 97]. There is a trade-off between price of the material and the required thickness for the mission. Some of these materials cannot be manufactured as thin as others to ensure the required strength, but as this section describes, that is not the only factor driving membrane thickness and material selection.

For LEO spacecraft, the largest threat to sail membranes is the material eroding due to the atomic oxygen (AO) in the atmosphere. This can be mitigated either by making

the membrane thicker and reducing the packing efficiency, or by using a material that is more resistant to erosion and thereby increasing the cost of the membrane. Tennyson [98] explained that atomic oxygen is the dominant gaseous species from 200 - 650 km altitude, and the AO number densities vary with orbital inclination and day/night cycles. When comparing an equatorial orbit and a polar orbit, both at an altitude of 400 km, the satellite in the equatorial orbit experiences up to 12% more AO flux than the one in the polar orbit [98]. For most polymers, atomic oxygen causes surface erosion, but it can also produce a passivating layer that protects the underlying substrate, such as the formulation of silicon-dioxide. Silver is the only metal that has been observed to have a measureable erosion [98].

The standard parameter used to measure the reaction rate of a material to atomic oxygen is erosion yield, R_e, calculated by Equation (3.28) where M = mass loss (g), A = exposed area (cm^2), F = atomic oxygen fluence ($atoms/cm^2$), and ρ = material density [98]. Table 3.8 lists the erosion yield of the four main materials mentioned earlier. These values were determined experimentally on the International Space Station during the test series called Materials International Space Station Experiments (MISSE) [99, 100].

$$R_e = \frac{M}{AF\rho} \tag{3.28}$$

Table 3.8: Erosion yield values for the common membrane materials

Material	Erosion Yield ($cm^3/atom$)	Reference
Mylar	3.01×10^{-24}	[100]
Kapton	3.05×10^{-24}	[99]
CP1	1.91×10^{-24}	[100]
Corin	3.05×10^{-26}	[99]

Thickness loss can be estimated using the nomogram shown in Figure 3.18. It was created by Tennyson [98] using experimental values based on the atomic oxygen fluence that is seen by a membrane when it is at a certain altitude for a number of days. This chart

uses an average atmospheric model of the AO number density and flux values [98]. In order to read this, one finds the number of days on the horizontal axis and the altitude on the left vertical axis, and then find the matching atomic oxygen fluence line, and trace that to the erosion yield line that corresponds to the membrane material. Finally, read the thickness loss off the right vertical axis. Figure 3.18 shows an example of a CP1 membrane at an altitude of 400 km for just over 100 days. By following the red arrows, one can see that the membrane would lose 21 μm in thickness. For the following analyses, Mylar is not included because the value is simlar to Kapton. The erosion yield of CP1 is rounded to 2.0×10^{-24} cm^3/atom, and the erosion yield of Corin is rounded to 5.0×10^{-26} cm^3/atom to match the figure.

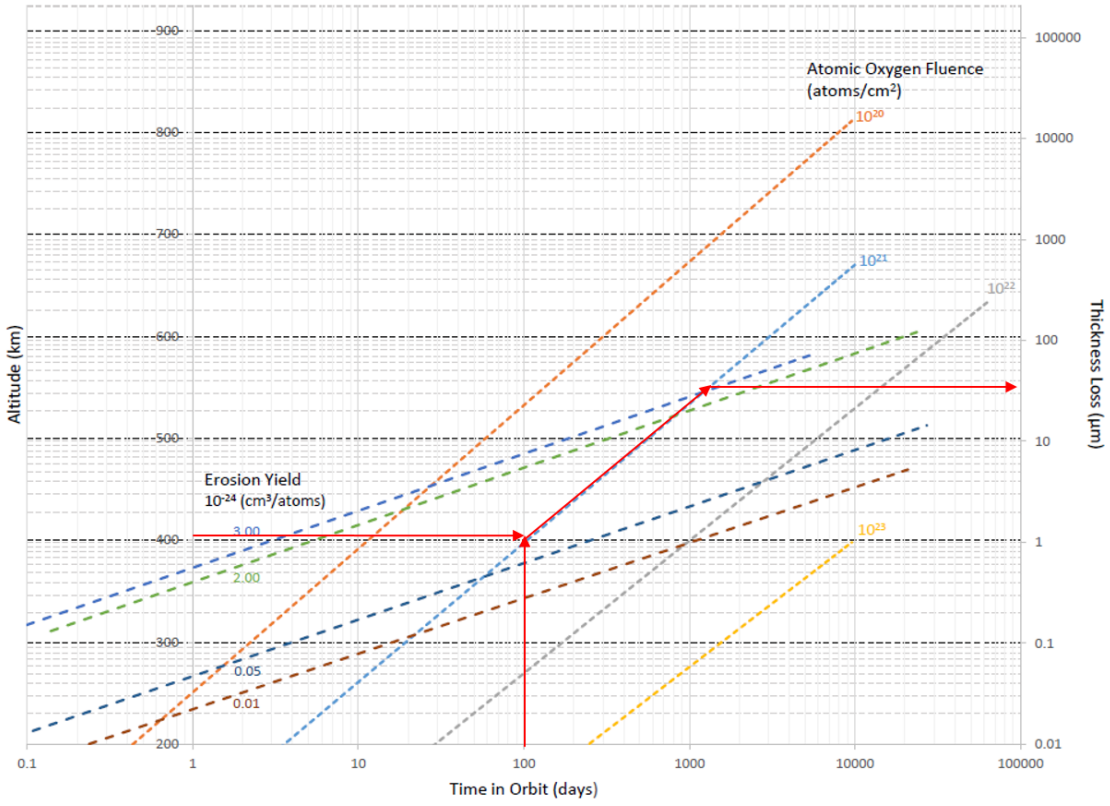

Figure 3.18: Nomogram for estimating polymer thickness loss as a function of altitude, time in orbit, and erosion yield (adapted from [98, 61]). Erosion yield for Kapton is approximately 3×10^{-24}, CP1 is approximately 2×10^{-24} cm^3/atoms [96], and Corin is approximately 5×10^{-26} cm^3/atoms [97].

Figure 3.18 predicts thickness loss for sails at a constant altitude, but drag sails traverse

many altitudes over their lifetimes. Thickness loss for this drag sail is estimated using the method describe by Fernandez [61] where the thickness loss is considered progressive and increases as the altitude decreases. The deorbit prediction is taken from the GMAT simulation shown earlier to estimate the number of days spent in each altitude region. Table 3.9 and Table 3.10 summarize the estimated thickness loss in each altitude range by using the lowest altitude in the range in the nomogram for a conservative estimate. Table 3.9 uses the simulated deorbit of an ESPA-class satellite with a mass of 180 kg, 10 m booms, inclination of 87.9°, and an initial altitude of 1,100 km. Table 3.10 uses the simulated deorbit of a CubeSat-class satellite with a mass of 12 kg, 1 m booms, inclination of 87.9°, and an initial altitude of 865 km. Most CubeSat-class satellites will be launched to altitudes closer to 600 km, so this process was repeated and determined that a CP1 membrane would lose about 32 μm of thickness and a Corin membrane would lose about 1 μm. This analysis shows that different membrane materials could be used depending on the deorbit profile of satellite. It can be seen that the ESPA-class satellite requires a thinner sail than the CubeSat class because the total deorbit time is less, and specifically it spends less time in the lower altitudes where there is more thickness loss.

Table 3.9: Total thickness loss of Kapton, CP1, and Corin membranes used to deorbit a 180 kg ESPA-class satellite with 10 m booms from a 1,100 km initial altitude orbit.

Altitude Range (km)	Time at this Altitude (days)	Thickness Loss (μm) Kapton	CP1	Corin
1100-600	8200	85	45	1.20
600-500	140	8	5	0.15
500-400	35	10	6	0.20
400-300	10	15	9	0.25
300-200	2.5	18	10	0.30
Total	8387.5	136	75	2.10

Table 3.10: Total thickness loss of Kapton, CP1, and Corin membranes used to deorbit a 12 kg Cubesat-class satellite with 1 m long booms from a 865 km initial altitude orbit.

Altitude Range (km)	Time at this Altitude (days)	Thickness Loss (μm) Kapton	CP1	Corin
865-600	8700	85	45	1.20
600-500	210	11	7	0.20
500-400	52	15	8	0.20
400-300	12	18	10	0.30
300-200	2	15	8	0.25
Total	8976	144	78	2.15

CHAPTER 4
AEROSTABILITY ANALYSIS

When the drag sail was chosen as the deorbit device type, there was concern about consistent drag area in the passive system, which led to the selection of an aerodynamically stable design of a square pyramid. This chapter discusses a simulation that investigates the effect of different apex half-angles on stability. There are two different phases of the analysis: a simplified model that assumes constant applications of the disturbance torques, known as the wind tunnel model, and a higher fidelity simulation that includes orbital motion.

4.1 Assumptions

The inputs to the simulation are orbital elements, start date and time, and the physical properties of the sail-satellite system. As with the deorbit analysis mentioned in Chapter 3, the system is in a circular orbit inclined at 87.9°, starting on July 1, 2020 at 12:00 pm. The mass of the satellite portion is set to 180 kg to be consistent with an ESPA class satellite. The boom length is set to 10 m to achieve a 177 m^2 drag area for an apex half-angle of 70°. To simplify the calculations, it is assumed that the satellite and drag sail system consist of a series of flat plates that behave like rigid bodies without self-reflection to allow the disturbance torques to be calculated with analytical equations.

Atmospheric density is modeled using the Jacchia 1970 formulation [74]. This requires estimates for the F10.7 and geomagnetic index for the simulation date. Those values are selected from the Future Solar Activity Estimates table published by Marshall Space Flight Center in June 2016 [101]. The values used are for the 95 percentile statistical confidence for the future predictions.

Since the simulation start date is fixed, the position of the Sun in relation to the Earth is also fixed at the start of the orbital motion simulation, but the vector relative to the

sail changes as the sail moves through its orbit. The solar radiation pressure contribution depends on the right ascension of the ascending node of the orbit, (Ω). For perspective, when $\Omega = 100°$, the orbit plane is nearly aligned with the Sun vector, as seen in Figure 4.1. When the simulation is long enough, the Sun vector will change as Ω precesses and the Earth moves around the Sun.

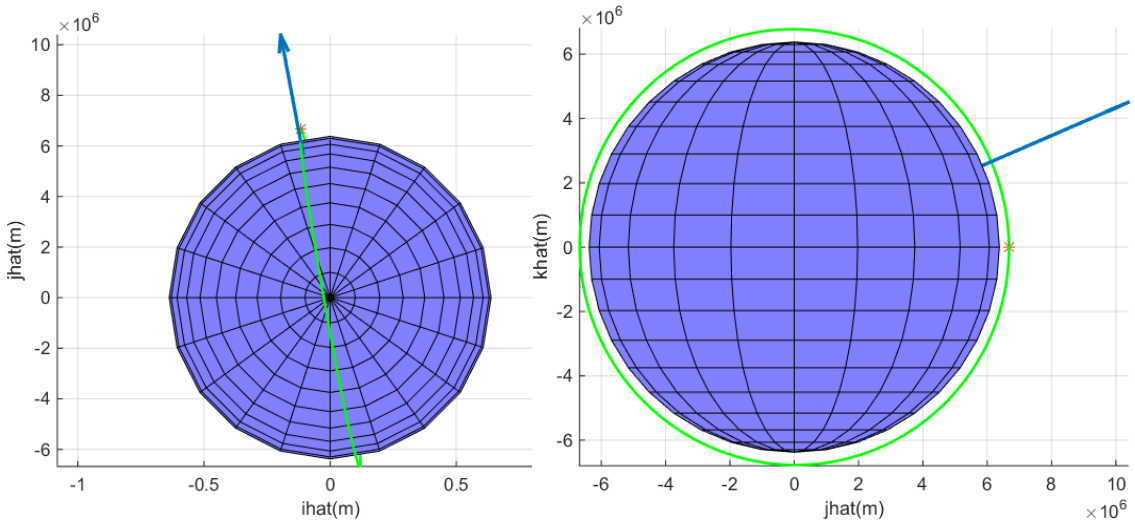

(a) (b)

Figure 4.1: The Sun position on July 1, 2020 at noon, and the orbit with $\Omega = 100°$.

4.2 Coordinate System

The coordinate system follows conventional flight dynamics body axes with the x direction along the longitudinal axis of the vehicle, and the y and z directions forming a right-handed set perpendicular to the x-axis [102]. This coordinate system can be seen in Figure 4.2a. The flow frame has f_1 in the direction of movement, f_3 pointing in the nadir direction, and f_2 completing the right hand set. Rotation of the solar sail is defined by angle of attack, α, and side slip angle, β. These can be seen in Figures 4.2b and 4.2c. Note that β is defined as positive for a negative rotation about the z-axis. Stability is determined by looking at the total angle of attack, α_T, which is the total angle between the x axis and the f_1 axis, and is defined in Equation (4.1). The sail is considered stable if $\alpha_T < 90°$ for the length of

the simulation. In order to remain stable, restoring moments are required to ensure the sail comes back to the maximum drag attitude if perturbed. This means a negative restoring moment about the y-axis (pitch) for positive perturbations in α, and a positive restoring moment about the z-axis (yaw) for perturbations in β.

$$\alpha_T = \cos^{-1}(\hat{f}_1 \cdot \hat{x}) \tag{4.1}$$

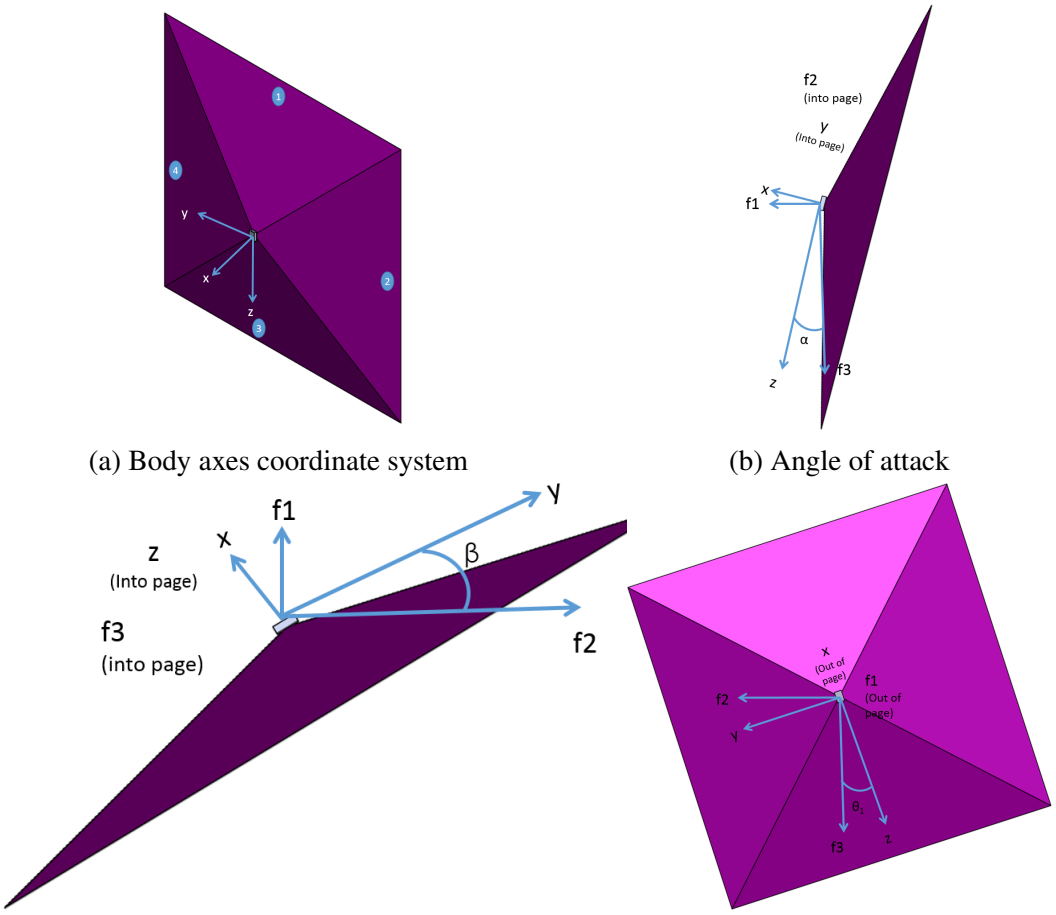

(a) Body axes coordinate system

(b) Angle of attack

(c) Side slip angle

(d) Roll angle

Figure 4.2: Definition of coordinate system and orientation angles used in the simulation.

4.3 Torque Definitions

There are three main torques that act on a satellite in orbit that will disturb its attitude. This section describes how they are calculated in this simulation.

The aerodynamic forces and moments are calculated using the procedure described by Schaaf and Chambre [103] where the coefficients of pressure and shear pressure shown in Equations (4.2) and (4.3) are integrated over the surface of each plate, where V_∞ is the freestream velocity of the air, T_∞ is the freestream static temperature of the air in Kelvin, T_w is the temperature of the surface, and σ_N and σ_T are the momentum accommodation coefficients in the normal and tangential directions. These equations were later presented in a modified format by Bird [104]. Equation (4.5) defines the angle γ_1 as the angle between the freestream and the vector parallel to the surface. The function $erf(x)$ is the error function which is found when integrating the normal distribution [105].

$$C_p = \frac{1}{s^2}\left[\left(\frac{2-\sigma_N}{\sqrt{\pi}} s\sin(\gamma_1) + \frac{\sigma_N}{2}\sqrt{\frac{T_w}{T_\infty}}\right) e^{-(s\sin\gamma_1)^2} + \left\{(2-\sigma_N)\left((s\sin\gamma_1)^2 + \frac{1}{2}\right) + \frac{\sigma_N}{2}\sqrt{\frac{\pi T_w}{T_\infty}} s\sin\gamma_1\right\}(1+\mathrm{erf}(s\sin\gamma_1))\right] \tag{4.2}$$

$$C_\tau = -\frac{\sigma_T \cos\gamma_1}{s\sqrt{\pi}}\left[e^{-(s\sin\gamma_1)^2} + \sqrt{\pi} s\sin\gamma_1\,(1+\mathrm{erf}(s\sin\gamma_1))\right] \tag{4.3}$$

$$s = \frac{V_\infty}{\sqrt{2RT_\infty}} \tag{4.4}$$

$$\sin\gamma_1 = -\hat{V}_\infty \cdot \hat{n} \tag{4.5}$$

The gravity gradient torque for the system is calculated using Equation (4.6), where $\vec{R}_c$ is the position vector of the center of mass of the sail system from the Earth's center, and $\hat{I}$

is the inertia dyadic of the sail-satellite system [106].

$$\vec{M} = \frac{3\mu}{R_c^5}\vec{R}_c \times \hat{I} \cdot \vec{R}_c \tag{4.6}$$

The solar radiation pressure (SRP) torque is calculated in a similar procedure as the aerodynamic torques, by substituting the normalized vector between the sail and the Sun for the normalized velocity vector and substituting Equation (4.7) and (4.8) [107] for Equation (4.2) and (4.3). $P_{rad} = 4.563 \times 10^{-6}$ N/m^2 is the nominal solar radiation pressure constant at 1 AU from the Sun [106], $\tilde{r}$ is the reflectance, $\tilde{\alpha}$ is the absorptance, $\varepsilon = 0.95$ is the fraction of photons to be reflected specularly, ϵ is the emissivity of the front and back of the sail depending on the subscript, and B is the non-Lambertian coefficient of the front and back of the sail. Equation (4.9) defines the angle between the normal vector of the sail and the unit vector from the Sun to the sail. Notice that this is defined opposite of γ_1 used in the aerodynamic formulas. These equations were dervied by Forward [107] in 1989 without assumptions on material properties, as opposed to the equations later used by McInnes [93] that assume a reflective sail to analyze SRP on solar sails.

$$C_n = P_{rad}\left[(\tilde{r} + \tilde{\alpha} + \tilde{r}\varepsilon)\cos^2\gamma_2 + B_f(1-\varepsilon)\tilde{r}\cos\gamma_2 + \tilde{\alpha}\frac{\epsilon_f B_f - \epsilon_b B_b}{\epsilon_f + \epsilon_b}\cos\gamma_2\right] \tag{4.7}$$

$$C_t = P_{rad}\left(\tilde{r} + \tilde{\alpha} - \tilde{r}\varepsilon\right)\cos\gamma_2 \sin\gamma_2 \tag{4.8}$$

$$\cos\gamma_2 = -\hat{\mathbf{e}}_\odot \cdot \hat{\mathbf{n}} \tag{4.9}$$

4.4 Equations of Motion

The equations of motion for this simulation involve both the attitude dynamics of the system and propagation of the system in its orbit. These equations are modified in order to isolate the behavior due to different torques, specifically by the creation of "Wind Tunnel Mode" that ignores orbital motion and changes in the external forces. Aerodynamic damping is included in order to capture the attitude to which the system trims. Another addition to the dynamics is shadowing for both solar radiation pressure and aerodynamics. This self-shadowing will be described at the end of this section.

4.4.1 Moments of Inertia

To calculate the dynamics of a system, the moments of inertia much be calculated first. To accomplish this, the system was divided into nine components: the satellite is modeled as a solid rectangular prism with a constant density, four isosceles triangle sail quadrants with negligible thickness, and four booms modeled as hollow cylinders. The overall inertia matrix is determined by calculating the inertia tensor for each component in its local frame, then rotating to the overall body frame shown in Figure 4.2a, applying the parallel axis theorem to move the reference axes to the center of mass of the system, and finally, taking the sum of all components.

The first step is to calculate the center of mass of each component in the body frame, then combine these values to determine the center of mass for the system. Since all of the components are assumed to be simple geometric shapes of uniform density, this is a matter where the geometric center is the center of mass. The overall center of mass is shown in Equation (4.10).

$$ {}_B\underline{r}^{B^*} = \frac{\underline{r}^{sa} * m_{sat} + m_{sail} * \sum_{i=1}^{4} \underline{r}^{si} + m_{boom} * \sum_{i=1}^{4} \underline{r}^{bi}}{m_{sat} + 4 * m_{sail} + 4 * m_{boom}} \tag{4.10} $$

The satellite (sa) is assumed to already be in the body frame. Using the equations

defined by Kane and Levinson [108], the inertia matrix about the center of mass (B^*) in the body frame (B) is described in Equation (4.11), where w_{sat} is the width in the y axis, H_{sat} is the height in the z axis, and l_{sat} is the length in the x axis.

$$ {}_B\mathbf{I}^{sa/B^*} = \frac{m_{sat}}{12} \begin{bmatrix} w_{sat}^2 + H_{sat}^2 & 0 & 0 \\ 0 & l_{sat}^2 + H_{sat}^2 & 0 \\ 0 & 0 & w_{sat}^2 + l_{sat}^2 \end{bmatrix} \tag{4.11} $$

For the sail quadrants ($s1 - s4$), the inertia matrix for an isosceles triangle is defined by the base width, b_{sail}, and the triangular height, (h_{sail}). The moment of inertia for a planar triangle about its center of mass is shown in Equation (4.12). The origin of the local coordinate system is located at the center of mass of the triangle with the local z-axis pointing up through the apex, the local y-axis pointing to the right, and the local x-axis is out of the plane [108].

$$ {}_s\mathbf{I}^{s/s^*} = m_{sail} \begin{bmatrix} \frac{b_{sail}^2}{24} + \frac{h_{sail}^2}{18} & 0 & 0 \\ 0 & \frac{h_{sail}^2}{18} & 0 \\ 0 & 0 & \frac{b_{sail}^2}{24} \end{bmatrix} \tag{4.12} $$

The booms ($b1 - b4$) are approximated as hollow cylinders where the local z-axis is the axis of rotational symmetry and the local x and y axes complete the right handed set. The inertia matrix in this local coordinate system about the center of mass is described in Equation (4.13), where r_o is the outer radius, r_i is the inner radius, and L is the length of the boom [109].

$$ {}_b\mathbf{I}^{b/b^*} = \frac{m_{boom}}{2} \begin{bmatrix} \frac{3(r_o^2+r_i^2)+L^2}{6} & 0 & 0 \\ 0 & \frac{3*(r_o^2+r_i^2)+L^2}{6} & 0 \\ 0 & 0 & r_o^2 + r_i^2 \end{bmatrix} \tag{4.13} $$

The next step is to define the rotation matrices for each component to rotate the inertia

matrix from the local frame to the body frame. To do this, the sail quadrants will be referred to by the labels $s1 - s4$, shown in Figure 4.2a, and the booms labeled $b1 - b4$ correspond to the boom between the sail quadrant of the same number and the quadrant incremented up. For example, boom $b1$ is between sail quadrants $s1$ and $s2$, and boom $b3$ is between sail quadrants $s3$ and $s4$, etc. These rotation matrices are defined by a series of Euler Angle rotations shown in Equations 4.14- 4.16 [110].

$$\mathbf{R}_1(\theta) = \begin{bmatrix} 1 & 0 & 0 \\ 0 & \cos\theta & \sin\theta \\ 0 & -\sin\theta & \cos\theta \end{bmatrix} \tag{4.14}$$

$$\mathbf{R}_2(\theta) = \begin{bmatrix} \cos\theta & 0 & -\sin\theta \\ 0 & 1 & 0 \\ \sin\theta & 0 & \cos\theta \end{bmatrix} \tag{4.15}$$

$$\mathbf{R}_3(\theta) = \begin{bmatrix} \cos\theta & \sin\theta & 0 \\ -\sin\theta & \cos\theta & 0 \\ 0 & 0 & 1 \end{bmatrix} \tag{4.16}$$

For the sail quadrants there are two rotations: the first to align the local x-y plane with that of the body frame through the angle ϕ', which is the angle from the x-y plane to the plane of each sail quadrant. The second rotation aligns the x-y axes with the body frame. Rotations from the local sail frames to the body frame are shown in Equation (4.17). The boom rotations match the sails of the same number, but an additional 45° needs to be added

to the final $\mathbf{R}_1$ rotation. This is shown in Equation (4.18).

$$
\begin{aligned}
{}^{B}\mathbf{C}^{s1} &= \mathbf{R}_2(-\phi') \\
{}^{B}\mathbf{C}^{s2} &= \mathbf{R}_1(90°)\mathbf{R}_3(-\phi') \\
{}^{B}\mathbf{C}^{s3} &= \mathbf{R}_1(180°)\mathbf{R}_2(\phi') \\
{}^{B}\mathbf{C}^{s4} &= \mathbf{R}_1(270°)\mathbf{R}_3(\phi')
\end{aligned}
\tag{4.17}
$$

$$
\begin{aligned}
{}^{B}\mathbf{C}^{b1} &= \mathbf{R}_2(-\phi') \\
{}^{B}\mathbf{C}^{b2} &= \mathbf{R}_1(135°)\mathbf{R}_3(-\phi') \\
{}^{B}\mathbf{C}^{b3} &= \mathbf{R}_1(225°)\mathbf{R}_2(\phi') \\
{}^{B}\mathbf{C}^{b4} &= \mathbf{R}_1(315°)\mathbf{R}_3(\phi')
\end{aligned}
\tag{4.18}
$$

These rotations are combined with the inertia matrix of the specific component to convert it to the body frame. The inertia matrix needs to be both pre- and post-mutiplied by the rotation matrix because the inertia matrix is a tensor. For example, the inertia matrix of sail 1 about the center of mass of the sail in the body frame is described in Equation (4.19).

$$
{}_{B}\mathbf{I}^{s/s^*} = \left[{}^{B}\mathbf{C}^{s1}\right]^{T}\left[{}_{s1}\mathbf{I}^{s1/s1^*}\right]\left[{}^{B}\mathbf{C}^{s1}\right] \tag{4.19}
$$

Next, translate the center of each local coordinate system to the center of mass by the parallel axis theorem. The procedure described by Kane and Levinson [108] entails adding an inertia matrix relative to the center of mass of a fictitious particle with the mass of the system that is situated at the center of the local coordinate system, ${}_{B}\mathbf{I}^{s^*/B^*}$. The inertia matrix of sail 1 about the center of mass of the system in the body frame is described by Equation (4.20).

$$
{}_{B}\mathbf{I}^{s/B*} = {}_{B}\,\mathbf{I}^{s/s^*} + {}_{B}\,\mathbf{I}^{s^*/B^*} \tag{4.20}
$$

This inertia matrix, ${}_{B}\mathbf{I}^{s^*/B^*}$, is made up of inertia moments and inertia products similar

to a regular inertia matrix, as shown in Equation (4.21). These moments and products are a function of the loction of the center of mass, ${}_B\underline{r}^{B^*}$; the location of the center of mass of the component in question (in this case sail 1, ${}_B\underline{r}^{s1^*}$); the mass of the sail, m_{sail}; and the axes of the body coordinate frame. One inertia moment and one inertia product are described in Equations (4.22) and (4.23), respectively. The other four terms follow the same pattern.

$$ {}_B\mathbf{I}^{s^*/B^*} = \begin{bmatrix} I_{xx} & I_{xy} & I_{xz} \\ I_{xy} & I_{yy} & I_{yz} \\ I_{xz} & I_{yz} & I_{zz} \end{bmatrix} \tag{4.21} $$

$$ {}_BI_{xx}^{s^*/B^*} = m_{sail}[({}_B\underline{r}^{B*} - {}_B\,\underline{r}^{s1*}) \times \hat{x}]^2 \tag{4.22} $$

$$ {}_BI_{xy}^{s^*/B^*} = m_{sail}[({}_B\underline{r}^{B*} - {}_B\,\underline{r}^{s1*}) \times \hat{x}] \cdot [({}_B\underline{r}^{B*} - {}_B\,\underline{r}^{s1*}) \times \hat{y}] \tag{4.23} $$

Once the inertia matrices of all the components have been rotated and translated to be in the body frame about the center of mass of the system, the final step to calculating the total inertia matrix is summing all the matrices together, as in Equation (4.24). This should produce a diagonal matrix with all the products of inertia equal to zero since the body axes defined in Figure (4.2a) are principal axes. The terms on the diagonal are the moments of inertia that will be used in the differential equations described in the next section.

$$ \begin{aligned} {}_B\mathbf{I}^{B/B^*} = {}_B\,\mathbf{I}^{sa/B^*} + {}_B\,\mathbf{I}^{s1/B^*} + {}_B\,\mathbf{I}^{s2/B^*} + {}_B\,\mathbf{I}^{s3/B^*} + {}_B\,\mathbf{I}^{s4/B^*} \\ + {}_B\mathbf{I}^{b1/B^*} + {}_B\,\mathbf{I}^{b2/B^*} + {}_B\,\mathbf{I}^{b3/B^*} + {}_B\,\mathbf{I}^{b4/B^*} \end{aligned} \tag{4.24} $$

4.4.2 Attitude Dynamics

The simulation integrates the non-linear equations of motion of the system. There are three types of equations that are integrated: kinematic differential equations, dynamic equations

of motion including the disturbance torques, and orbital equations of motion to propagate the system through its orbit around Earth. The non-linear equations of motion for an orbiting rigid body about body-fixed principal axes described by Wie [106] are used. Equation (4.25) shows the kinematic differential equations which use the orientation angles from Figure 4.2 with $\theta_2 = \alpha$ and $\theta_3 = -\beta$. Equations (4.26) are the dynamic equations of motion including the disturbance torques described earlier [106].

$$\begin{bmatrix} \dot{\theta}_1 \\ \dot{\theta}_2 \\ \dot{\theta}_3 \end{bmatrix} = \frac{1}{\cos\theta_1} \begin{bmatrix} \cos\theta_2 & \sin\theta_1 \sin\theta_2 & \cos\theta_1 \sin\theta_2 \\ 0 & \cos\theta_1 \cos\theta_2 & -\sin\theta_1 \cos\theta_2 \\ 0 & \sin\theta_1 & \cos\theta_1 \end{bmatrix} \begin{bmatrix} \omega_1 \\ \omega_2 \\ \omega_3 \end{bmatrix} + \frac{n}{\cos\theta_2} \begin{bmatrix} \sin\theta_3 \\ \cos\theta_2 \cos\theta_3 \\ \sin\theta_2 \sin\theta_3 \end{bmatrix} \tag{4.25}$$

$$\begin{aligned} I_x\dot{\omega}_1 &= (I_y - I_z)\omega_2\omega_3 - 3n^2(I_y - I_z)\sin\theta_1 \cos\theta_1 \cos^2\theta_2 + M_{x,aero} + M_{x,SRP} \\ I_y\dot{\omega}_2 &= (I_z - I_x)\omega_1\omega_3 + 3n^2(I_z - I_x)\cos\theta_1 \cos\theta_2 \sin\theta_2 + M_{y,aero} + M_{y,SRP} \\ I_z\dot{\omega}_3 &= (I_x - I_y)\omega_1\omega_2 + 3n^2(I_x - I_y)\sin\theta_1 \sin\theta_2 \cos\theta_2 + M_{z,aero} + M_{z,SRP} \end{aligned} \tag{4.26}$$

There are four terms on the right hand side of each of the three dynamic equations of motion described in Equations (4.26). The first term describes the torque free dynamics of the system. The other three terms specifically represent a disturbance torque and can be removed from the equation to isolate the contributions of a specific torque. The second term is derived from the gravity gradient torque described in Equation (4.6) with the added contribution of the mean motion of the spacecraft in orbit (n). The third and fourth terms are aerodynamic torques and solar radiation pressure torques, respectively.

4.4.3 Orbit Propagation

For the orbit propagation, two perturbations were taken into account beyond the general two-body problem formulation: aerodynamic drag and the first term of Earth oblateness (J_2). Aerodynamic acceleration comes from the aerodynamic drag force in the flow direction (f_1), applied in the direction opposite of the velocity of the system relative to the atmosphere. The velocity relative to the atmosphere is calculated in Equation (4.27) with v as the orbital velocity, r as the orbital position, and $\dot{\theta}_G = 7.27x10^{-5}$ rad/s as the rotation rate of the Earth [110].

$$\dot{r}_a = \begin{bmatrix} v(1) + \dot{\theta}_G r(2) \\ v(2) - \dot{\theta}_G r(1) \\ v(3) \end{bmatrix} \tag{4.27}$$

The magnitude of the aerodynamic drag force is calculated for the disturbance torque, so the aerodynamic acceleration is assumed to be [110]:

$$\dot{v}_{aero} = \frac{F_{aero}(1)}{m_{sys}} * \frac{\dot{r}_a}{|\dot{r}_a|} \tag{4.28}$$

For Earth oblateness, only the first two terms are used. The first term corresponds to the traditional two-body problem, and the second is the J_2 term that has the greatest impact on orbital motion. The three components of acceleration due to gravity and Earth oblateness are shown in Equations (4.29), (4.30), and (4.31) where $r_E = 6378.14$ km is the equatorial radius of the Earth, $\mu = 398600.44$ km^3/sec^2 is the gravitational parameter of Earth, and $J_2 = 1082.64 \times 10^{-6}$ [110].

$$\dot{v}_{x,J_2} = \frac{-\mu r(1)}{|r|^3} \left[1 - J_2 * \frac{3}{2} (\frac{r_E}{|r|})^2 (5 \frac{r(3)^2}{|r|^2} - 1) \right] \tag{4.29}$$

$$\dot{v}_{y,J_2} = \frac{r(2)}{r(1)} \dot{v}_{x,J_2} \tag{4.30}$$

$$\dot{v}_{z,J_2} = \frac{-\mu r(3)}{|r|^3}\left[1 + J_2 * \frac{3}{2}(\frac{r_E}{|r|})^3(3 - 5\frac{r(3)^2}{|r|^2})\right] \tag{4.31}$$

The full equation of motion for the orbit propagation is shown in Equation (4.32).

$$\dot{v} = \dot{v}_{aero} + \begin{bmatrix} \dot{v}_{x,J2} \\ \dot{v}_{y,J2} \\ \dot{v}_{z,J2} \end{bmatrix} \tag{4.32}$$

For the final aspect of orbital motion, take into account the relative positions of the Earth, Sun, and sail to monitor when the sail moves into eclipse. Kelso [111] clearly explained the geometry and equations to determine if the satellite is in full shadow, known as Earth's umbra, or partial shadow, known as Earth's penumbra. Figure 4.3 demonstrates these concepts [111].

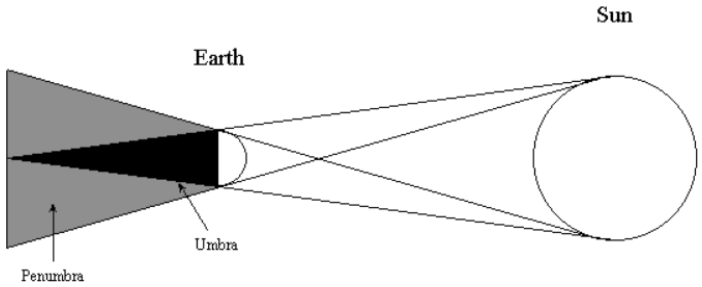

Figure 4.3: Diagram of the Earth-Sun shadow geometry that defines umbra and penumbra [111].

The calculations only rely on the radius of the Earth, $R_E = 6378.14$ km; the radius of the Sun, $R_S = 695,800$ km; the position vector of the satellite in ECI coordinate frame in km, $\vec{r}$; and the vector from the satellite to the Sun in ECI in km, $\vec{r}_{SS}$. first, determine the semi-diameters of the Earth and the Sun according to Equations (4.33), and (4.34), respectively. Then, calculate the angle between the center of the Earth and the Sun using Equation (4.35) [111].

$$\theta_E = \sin^{-1}(\frac{R_E}{|\vec{r}|}) \tag{4.33}$$

$$\theta_S = \sin^{-1}(\frac{R_E}{|\vec{r}_{SS}|}) \tag{4.34}$$

$$\theta_{shadow} = \cos^{-1}(\frac{\vec{r} \cdot \vec{r}_{SS}}{|\vec{r}| * |\vec{r}_{SS}|}) \tag{4.35}$$

The satellite is in umbra when $\theta_E > \theta_S$ and $\theta_{shadow} < (\theta_E - \theta_S)$. It is in penumbra when $|\theta_E - \theta_S| < \theta_{shadow} < (\theta_E + \theta_S)$ [111]. This is accounted for by multiplying the SRP force and moments by 0 if the satellite is in umbra, and 0.5 if it is in penumbra.

4.4.4 Wind Tunnel Mode

As part of this investigation, the behavior of the system was isolated from the orbital motion. This is called "Wind Tunnel Mode" because aerodyanmic flow direction is constant, similar to a wind tunnel test section. This means that all the orbital motion is turned off, including gravity gradient torques. The position of the Sun is determined by a single "Sun angle" in the $f_1 - f_2$ plane.

When converting from the full simulation, first is modify the equations of motion by setting the mean motion to zero, $n = 0$. This simplifies the kinematic differential equations shown in Equation (4.25) to the equations for a 3-2-1 body fixed rotation, shown in Equation (4.36). The dynamic equations of motion simplify to Equations (4.37), where both the aerodynamic and SRP torques can be set equal to zero depending on the situation desired. The time derivatives of the orbital position and velocity, $\dot{r}$ and $\dot{v}$, are also set equal to zero to eliminate the system's movement through space.

$$\begin{bmatrix} \dot{\theta}_1 \\ \dot{\theta}_2 \\ \dot{\theta}_3 \end{bmatrix} = \frac{1}{\cos\theta_1} \begin{bmatrix} \cos\theta_2 & \sin\theta_1 \sin\theta_2 & \cos\theta_1 \sin\theta_2 \\ 0 & \cos\theta_1 \cos\theta_2 & -\sin\theta_1 \cos\theta_2 \\ 0 & \sin\theta_1 & \cos\theta_1 \end{bmatrix} \begin{bmatrix} \omega_1 \\ \omega_2 \\ \omega_3 \end{bmatrix} \tag{4.36}$$

$$
\begin{aligned}
I_x\dot{\omega}_1 &= (I_y - I_z)\omega_2\omega_3 + M_{x,aero} + M_{x,SRP} \\
I_y\dot{\omega}_2 &= (I_z - I_x)\omega_1\omega_3 + M_{y,aero} + M_{y,SRP} \\
I_z\dot{\omega}_3 &= (I_x - I_y)\omega_1\omega_2 + M_{z,aero} + M_{z,SRP}
\end{aligned} \tag{4.37}
$$

The final modification is the vector between the sail and the Sun. For the orbital motion version, this vector depends on the right ascension of the ascending node of the orbit and it changes as the sail's movement is propagated. For Wind Tunnel Mode, the angle toward the Sun is treated as a constant throughout the simulation.

4.4.5 Damping

When a vehicle undergoes a rotation about the y-axis, which creates a pitching motion, the atmosphere creates a small damping effect to counteract it. This has been studied extensively for hypersonic flow in the Newtonian regime, where the air can be modeled as a continuum, for the purposes of re-entering the atmosphere on either Earth or Mars [112]. For both free-molecular flow and Newtonian, the aerodynamic loads are calculated by integrating the coefficient of pressure over the surface of the body. The former case was described in Equation (4.2) and the latter case can be simplified into Equation (4.38), where V_N is the velocity normal to the surface of the body. This can be written as $V_N = V_\infty \sin\gamma_1$ when you rearrange Equation (4.5).

$$
C_{P,Newton} = \frac{2V_N^2}{V_\infty^2} \tag{4.38}
$$

Schoenenberger et al. [112] accounts for the pitching moment by modifying V_N according to Equation (4.39), where $\vec{q}$ is the pitch rate, and $\vec{r}$ is the distance from the point about which the body is rotating. This modification means that the damping increases as the distance from the center of rotation increases.

$$
V_N = V_{N,\infty} + (\vec{q} \times \vec{r}) \cdot \hat{n} \tag{4.39}
$$

For Newtonian flow, it is sufficient to substitute Equation (4.39) into Equation (4.38), then integrate over the surface. For free molecular flow, both Equations (4.2) and (4.3) must be modified by replacing $s \sin \gamma_1$ with Equation (4.39).

In order to incorporate this modification into the simulation, each sail quadrant was divided into a grid according to the parameter dn. This parameter sets the number of divisions per side of each triangle, resulting in dn^2 smaller triangles on each sail while $\vec{r}$ is the distance from the center of mass of the satellite-sail system to the centroid of that triangle. For the investigations, $dn = 10$ is used to balance out the time required for a simulation run and the ability of the simulation to damp out the attitude oscillations. Tables 4.1 and 4.2 demonstrate this for the same case in Wind Tunnel Mode and with orbital motion. The total angle of attack was measured at the end of the simulation and with the peak closest to $\alpha = 22°$, which is about half of the initial angle of attack. The first case with $dn = 1$ corresponds to no damping, so the angle of attack grows instead of decreasing like in the other cases. It can be seen for both cases that for $dn > 10$ the increased accuracy is not significant enough for the increased run time.

Table 4.1: Damping grid parameter, dn, comparison for wind tunnel mode with aerodynamics and SRP. $\phi = 70°$, $\alpha_0 = 45°$, Sun angle $= 45°$, and $h = 400$ km.

dn	Final α	t($\alpha_0/2$)	$\alpha_0/2$	Run Time (min)
1	58.59°	N/A	N/A	1.54
5	1.217°	2813 secs	22.07°	1.61
10	1.279°	2815 secs	21.94°	3.52
20	1.282°	2815 secs	21.91°	10.03
30	1.281°	2810 secs	21.91°	20.59

4.4.6 Self-Shadowing

When investigating the stability of a system with a three dimensional shape, like a square pyramid, as opposed to a planar shape, it is important to realize that parts of the sail will block other parts from the flow (for aerodynamics) or the Sun (for SRP) as a result of self-

Table 4.2: Damping grid parameter, dn, comparison for orbital motion mode with aerodynamics and SRP. $\phi = 70°$, $\alpha_0 = 45°$, $\Omega = 45°$, and $h = 400$ km.

dn	Final α	t($\alpha_0/2$)	$\alpha_0/2$	Run Time (min)
1	48.5°	N/A	N/A	1.20
5	0.6696°	2510 secs	21.93°	1.04
10	0.6845°	2509 secs	21.83°	1.88
20	0.6844°	2513 secs	21.69°	4.71
30	0.6913°	2509 secs	21.8°	9.29

shadowing. Roberts and Harkness [113] describe four different aerodynamic shadowing regimes for a conical drag sail in terms of angle of attack. Figures 4.4 through 4.7 display the four regimes for a squard pyramid sail in the flow frame described earlier. These concepts are also used for shadowing from the Sun for the solar radiation pressure calculations using γ_2 from Equations (4.7) and (4.8) instead of total angle of attack, α_T.

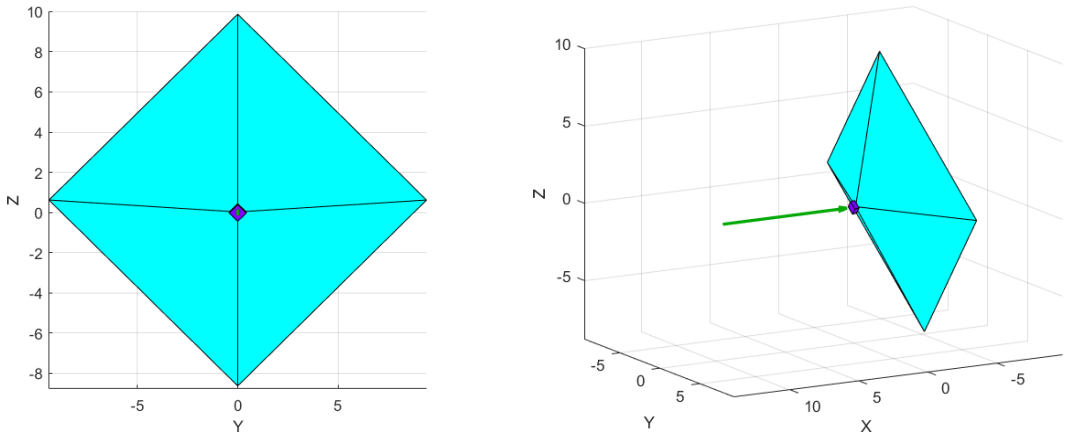

(a) Viewed along flow vector

(b) Isometric view with flow vector

Figure 4.4: Shadowing Regime 1 where the top surfaces (light blue) of all four sail quadrants are wetted by the flow ($\alpha_T < \phi$).

Regime 1 occurs when $\alpha_T < \phi$, and Regime 2 occurs when $\phi < \alpha_T < \pi/2$, where the self-shadowing begins. Figures 4.4 and 4.5 show that the back surfaces of the sail (dark blue) do not need to be taken into account because of the upper bound of $\alpha_T = \pi/2$. Regime 1 is the default attitude assumption where all of the top surfaces are visible to the flow. Regime 2 is accounted for by comparing the normal vector of each sail quadrant to the flow vector. If the dot product is negative, the sail quadrant is not facing the flow and

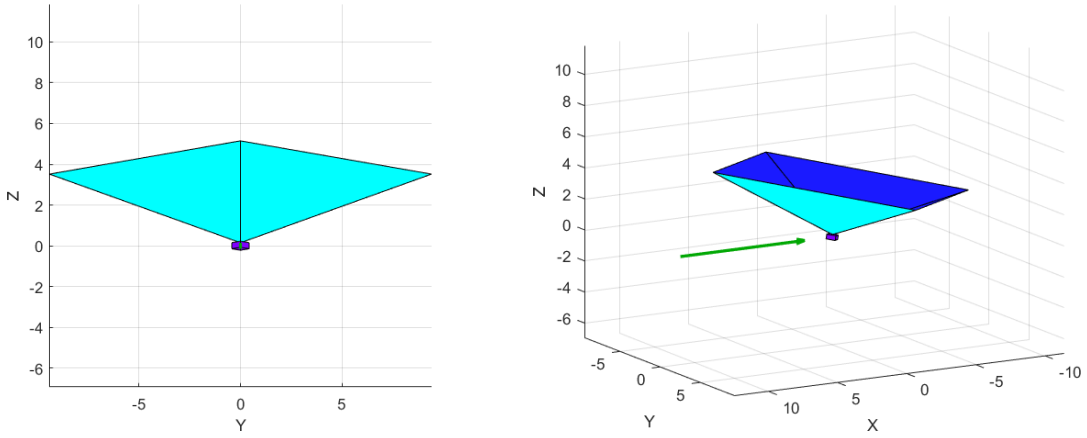

(a) Viewed along flow vector (b) Isometric view with flow vector

Figure 4.5: Shadowing Regime 2 where some of the quadrants are shadowed by the others ($\phi < \alpha_T < \pi/2$).

the aerodynamic contribution is set equal to zero. This is implemented using the Heaviside function as described by Hart et al. [90] which makes the aerodynamic force on each grid the value calculated by Equation (4.40).

$$F_{aero_i} = (C_{Pi} * \hat{n} + C_{\tau i} * \hat{t}) * A_i * H(-\hat{V}_\infty \cdot \hat{n}) \tag{4.40}$$

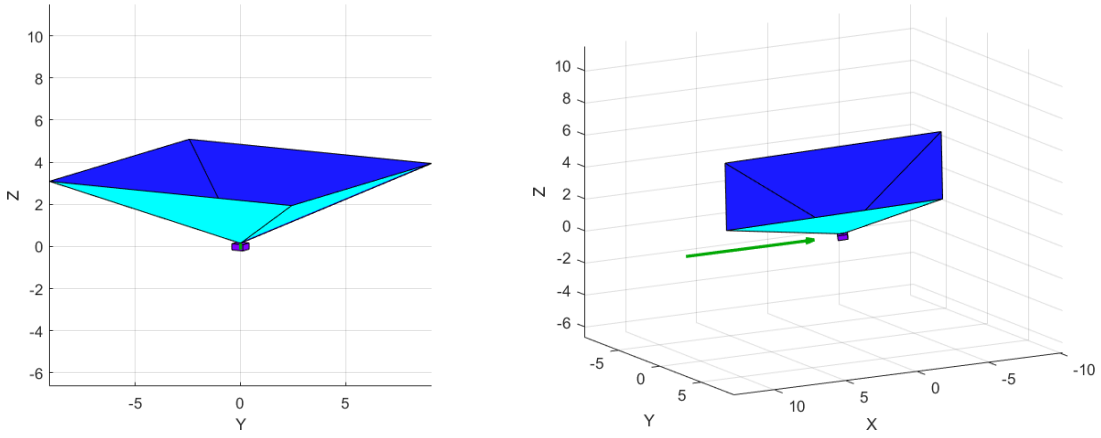

(a) Viewed along flow vector (b) Isometric view with flow vector

Figure 4.6: Shadowing Regime 3 where the bottom surfaces (dark blue) of some quadrants can be seen, but they are partially shadowed by the top surface (light blue) of the other quadrants ($\pi/2 < \alpha_T < \pi - \phi$).

Both Regimes 3 and 4 include contributions from the back surfaces of the sail quadrants

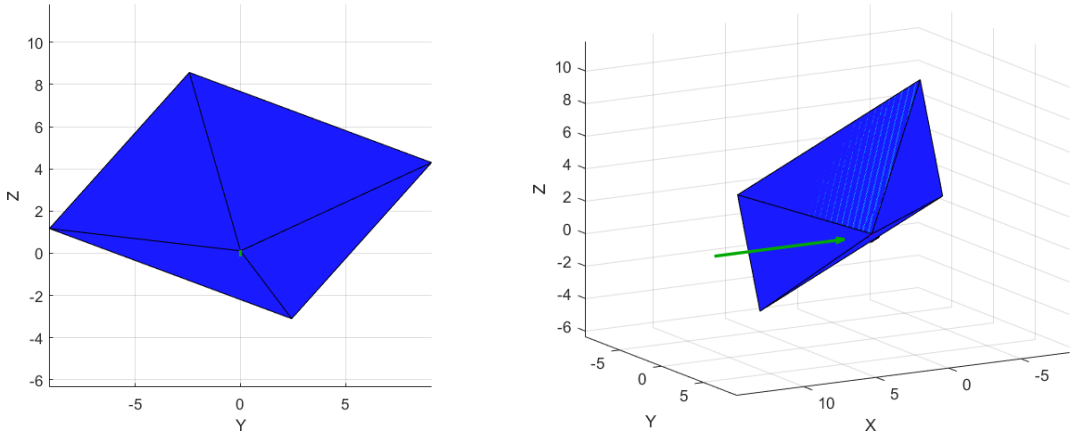

(a) Viewed along flow vector (b) Isometric view with flow vector

Figure 4.7: Shadowing Regime 4 where the bottom surfaces (dark blue) of all four sail quadrants are wetted by the flow ($\pi - \phi < \alpha_T < \pi$).

because they occur when $\alpha_T > \pi/2$. Regime 4 is the opposite of Regime 1, where the back surfaces of all four quadrants are visible to the flow. Contributions from self-reflection were not included to simplify the aerodynamics. In the simulation, if $\alpha_T > \pi/2$, then the aerodynamics and Heaviside function from Equation (4.40) are applied after replacing the sail normal vector with its negative, $\hat{n} = -\hat{n}$. The added complication of Regime 3 is also turning off the contribution of the grid sections located above the shadow lines, which are defined by projecting the edges of the leading sails onto the trailing sail.

There are three steps to projecting the edges to create the shadow lines. The first step is to determine the leading corner by taking the dot product between the flow vector and the position vector to each of the four corners. The smallest value (specifically the most negative) is the leading corner. To facilitate this discussion, Figure 4.8 shows the four sail quadrants labeled 1-4 counter-clockwise, with the corresponding corners following the quadrant. In the orientation pictured, corner 2 (C2) is the leading corner. This means that S2 and S3 are the leading sail quadrants with S1 and S4 the trailing quadrants.

The second step to determine the shadow line is to project the leading corner (C2) into the plane of each of the opposing sail planes (S1 and S4) along the flow vector. This is accomplished by finding a line through C2 in the direction of the flow, $\hat{f}$, using Equa-

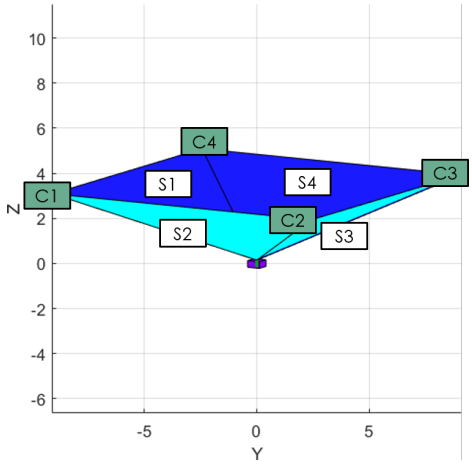

Figure 4.8: Shadowing Regime 3 viewed along the flow vector with the corners and sail quadrants labeled.

tion (4.41) where t is a parameterizing constant. Then, calculate the point where it intersects with the plane of the sail. For S1, the sail quadrant plane is defined by the normal vector $\hat{n}_{S1}$ and the point C1 using Equation (4.42). Substitute the components of Equation (4.41) into Equation (4.42), then solve for t to get Equation (4.43). Finally, substitute t back into Equation (4.41). This procedure is repeated for the other opposing corner for each sail. So in this example, C2 and C3 are projected onto S1, then C2 and C1 are projected onto S4.

$$\vec{L} = \begin{bmatrix} C2_x \\ C2_y \\ C2_z \end{bmatrix} + t \begin{bmatrix} f_x \\ f_y \\ f_z \end{bmatrix} \tag{4.41}$$

$$n_{S1,x}(x - C1_x) + n_{S1,y}(y - C1_y) + n_{S1,z}(z - C1_z) = 0 \tag{4.42}$$

$$t = \frac{\hat{n}_{S1} \cdot (C1 - C2)}{\hat{n}_{S1} \cdot \hat{f}} \tag{4.43}$$

The third step is to create the lines that define the edges of the shadow on S1 and S4. In order to make this procedure general, two lines are found on each sail. It can be seen in

Figure 4.8 that only one line is needed for S1, but since projected C2 is in the middle of S4, two lines are required. Using S4 as an example, the two lines are from projected C2 to projected C1, and from projected C2 to C3 (since it is already in the plane of S4). A grid section is visible to the flow if the centroid is on the opposite side of both shadow lines projected onto the plane of the sail from the origin of the body frame.

4.5 Results

Many cases were investigated with this simulation to determine the design apex-half angle of the $[PS]^2$ system and to understand the performance. Table 4.3 lists the input parameters that were varied. The final variable, Sun Angle, is the angle between the Sun and the flow vector in Wind Tunnel Mode, and corresponds to the right ascension of the ascending node of the orbital plane for the orbital motion simulation. For all of the cases, the simulation ran for 10 hours (36,000 seconds), which is a little more than 6 orbits.

Table 4.3: The input parameters for the simulation.

Parameter	Values
Altitude (h)	400, 500, 600 km
Apex Half-Angle (ϕ)	50°, 70°, 80°
Initial Angle of Attack (α_0)	0°, 10°, 45°, 120°
Sun Angle (SA or Ω)	0°, 45°, 90°, 100°

In the following sections, the behavior of α_T in each case is classified into one of five categories. Each category is assigned a color that is used in the figures to compile the results from the cases investigated. Table 4.4 provides the definition and associated color for each category, and Figure 4.9 shows examples of each category. There are two examples for marginally stable (orange) to demonstrate both halves of the definition. The vertical gray lines designate the start of a new orbit.

Table 4.4: Stability classification definitions with color assignment for plots.

Classification	Definition
Stable	Oscillations damp down to $< 10°$ and are periodic about $0°$
Relatively Stable	Oscillations about $0°$ with amplitudes $< 90°$ and decreasing, needs more time; Or trims to an angle $< 25°$
Marginally Stable	Amplitude of oscillations $< 90°$ and/or trims to angle $0° < \alpha_T < 90°$
Marginally Unstable	Amplitude of oscillations $< 90°$ for part of the simulation, then grows; Or trims to an angle $> 90°$
Unstable	Oscillations are large and random

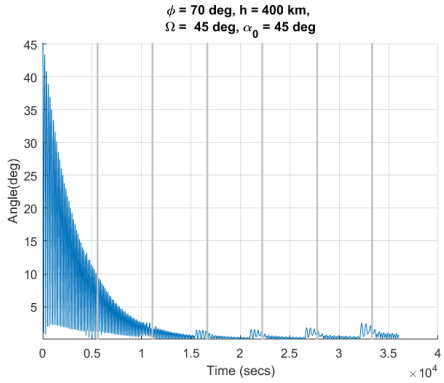

(a) Stable (green)

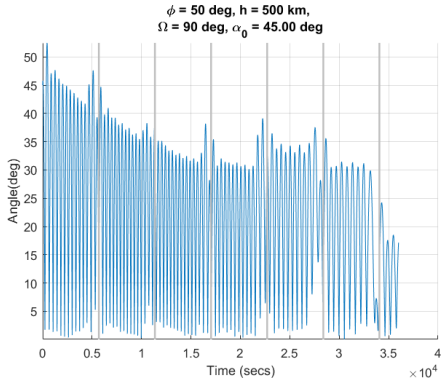

(b) Relatively Stable (light green)

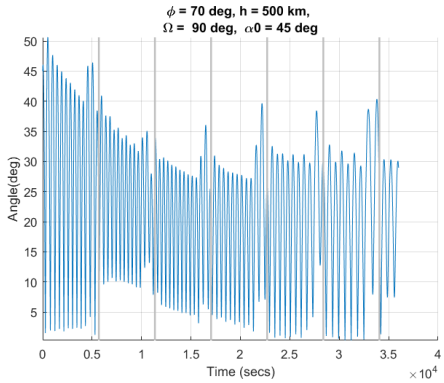

(c) Marginally Stable (yellow)

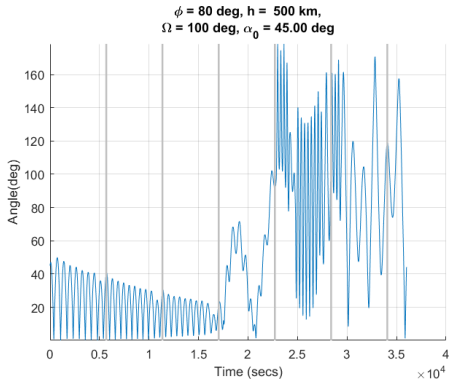

(d) Marginally Unstable (orange)

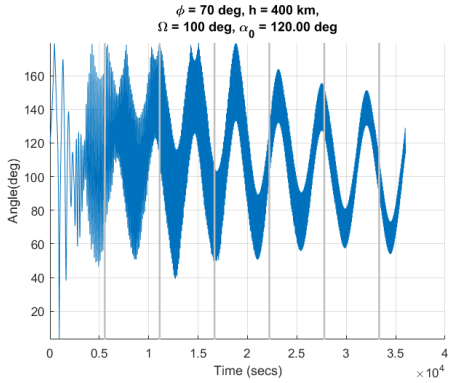

(e) Marginally Unstable (orange)

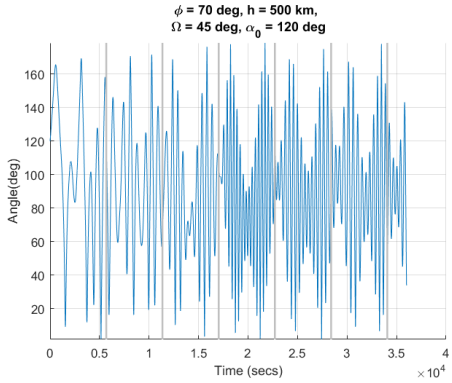

(f) Unstable (red)

Figure 4.9: Examples of each stability classification from the orbital motion simulation.

4.5.1 Sail Membrane Optical Properties

The initial design for the $[PS]^2$ system included a reflective membrane because the aluminum layer protects the membrane from atomic oxygen, and reflective membranes are commonly used for solar sails. The problem was that the reflective sail had a significantly increased contribution from SRP, disrupting the stability. The parameters used to calculate the SRP in Equations 4.7 and 4.8 for both a reflective sail and a transparent sail are listed in Table 4.5.

Table 4.5: Sail optical properties used in the SRP calculations for reflective and clear membranes.

Property	Reflective Sail*	Transparent Sail+
Reflectance ($\tilde{r}$)	0.85	0.0914
Absorptance ($\tilde{\alpha}$)	0.15	0.0579
Non-Lambertian coefficient front (B_f)	0.79	0.667
Non-Lambertian coefficient back (B_b)	0.667	0.667
Emissivity of the front (ϵ_f)	0.05	0.29
Emissivity of the back (ϵ_b)	0.55	0.29

* Properties of a reflective sail found in [93].
+ Properties of a clear sail were provided in personal communication with Brandon Farmer from Nexolve Corporation on June 14, 2017.

In the simulation, according to the classifications defined in Table 4.4, most of the cases at 400 km were relatively stable (light green), and the majority of the cases at 500 km were marginally stable or marginally unstable (yellow or orange). Figure 4.10 shows the total angle of attack plots, aerodynamic torque plots, and SRP torque plots for both a reflective sail and clear sail. Both use the same input parameters for the orbital motion simulation where $\phi = 70°$, $h = 500$ km, $\alpha_0 = 45°$, and $\Omega = 45°$. This case for the reflective sail is classified as marginally stable and the transparent sail is classified as relatively stable.

Contributing to the difference in stability is the increase in magnitude of the SRP torques. The SRP torques on a reflective sail are an order of magnitude higher than a clear sail (10^{-3} compared to 10^{-4}). It can be seen that this higher SRP makes the angle of attack initially increase by a few degrees, and requires restoring torques provided by the

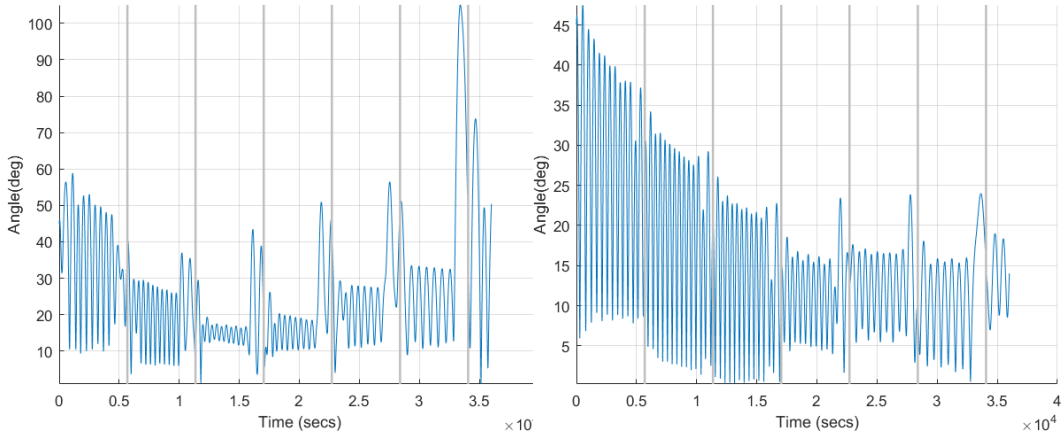

(a) α_T history of reflective sail (b) α_T history of transparent sail

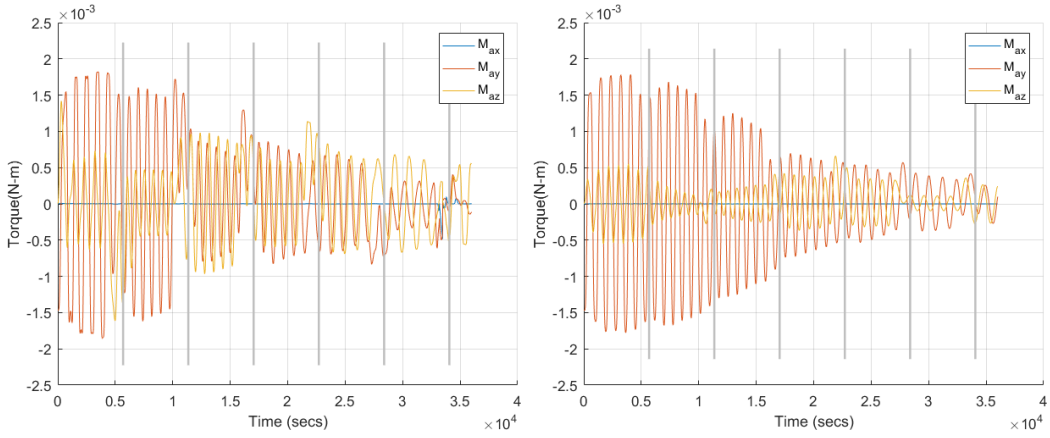

(c) Torque history of reflective sail (d) Torque history of transparent sail

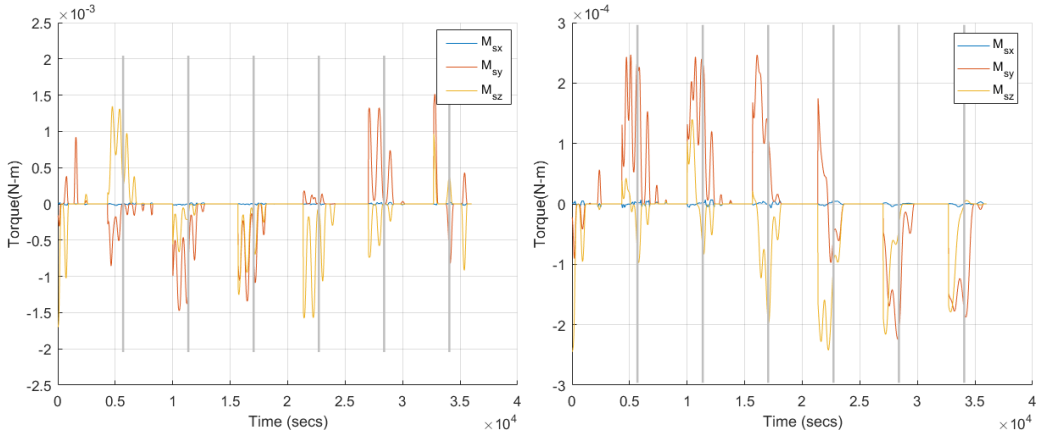

(e) SRP torque history of reflective sail (f) SRP torque history of transparent sail

Figure 4.10: Comparing the behavior of a reflective sail and transparent sail during the orbital motion simulation. $\phi = 70°$, $h = 500$ km, $\alpha_0 = 45°$, $\Omega = 45°$

aerodynamic forces to be about three times higher.

Another reason SRP causes the sail to become unstable is because it functions as a

step input every time the satellite-sail system moves out of eclipse. It can be seen at the end of each orbit that the SRP increases as the sail moves out of eclipse, triggering an increase in aerodynamic torques in the opposite direction and an increase in the total angle of attack. Larger torques cause faster oscillations, which can lead to instability. Figure 4.11 shows the same cases with a reflective sail and a transparent sail simulated for 2.5 days, or approximately 38 orbits. The reflective sail becomes moderately unstable while the transparent sail remains relatively stable.

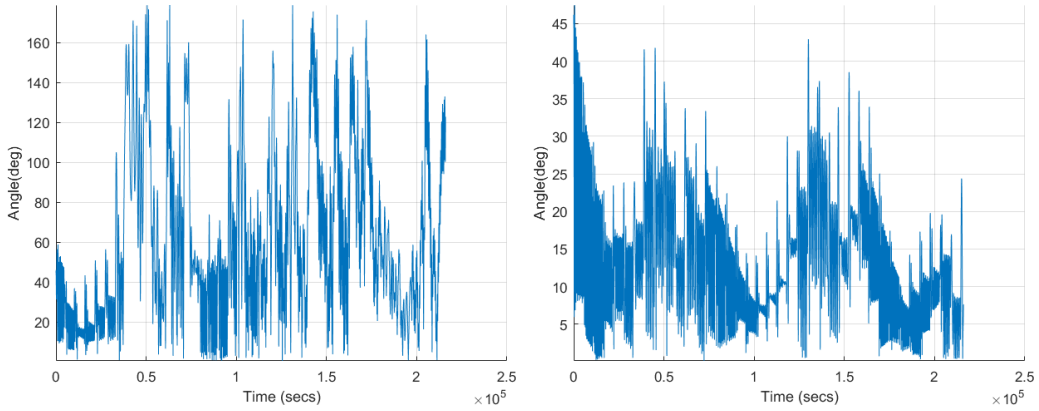

(a) Reflective Sail (b) Transparent Sail

Figure 4.11: Comparing total angle of attack history for reflective and transparent sails for simulation length of 2.5 days.

4.5.2 Wind Tunnel Mode

The purpose of Wind Tunnel Mode is to isolate the sail from variations due to the gravity gradient and non-cyclical SRP disturbance. It is used to investigate behavior of the different apex half-angles and verify the simulation performance. This is accomplished in two phases: aerodynamic forces only, then aerodynamics and SRP.

Aerodynamics Only

The results for the wind tunnel mode cases with only aerodynamics are summarized in Figure 4.12. Since the SRP is turned off, the Sun angle does not effect the result, so is not included. These plots show that the system is stable or relatively stable for altitudes of 500

km or below. The system is even able to flip itself over if it is deployed with the back facing into the flow ($\alpha_0 > 90°$). There is not a significant difference between the apex half-angles.

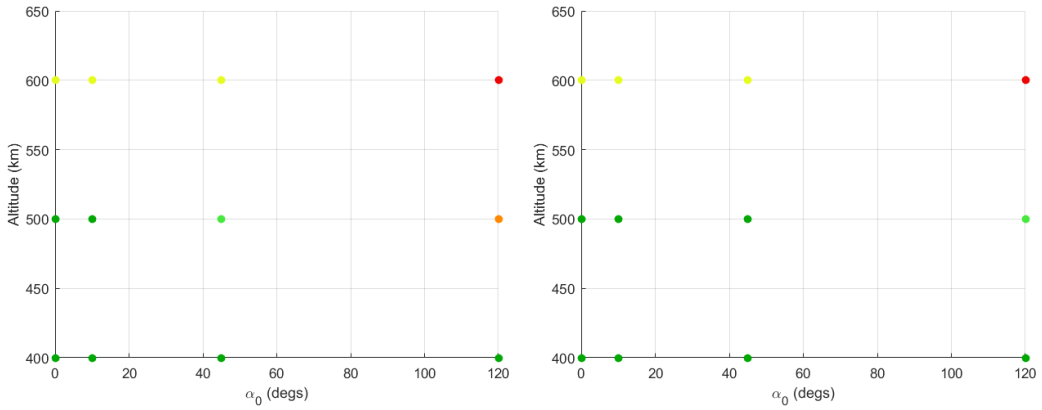

(a) $\phi = 50°$

(b) $\phi = 70°$

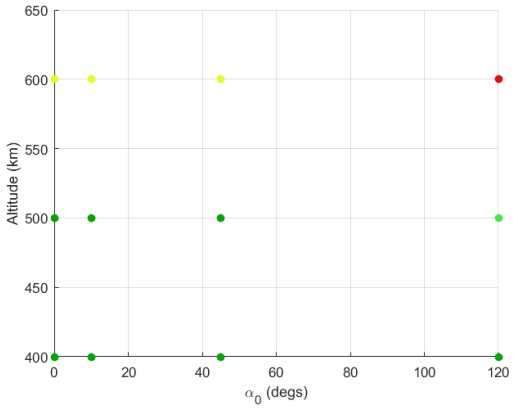

(c) $\phi = 80°$

Figure 4.12: Summary of the results from the wind tunnel simulation with aerodynamic and gravity gradient torques.

Aerodynamics and SRP

The results become more complicated when SRP is included, as shown in Figure 4.14. These plots show that at 500 km, SRP is large enough to disturb the stability of the system, but at an altitude of 400 km, the aerodynamic torques dominate enough that the sail flips over if it deploys backwards to the flow. The apex half-angle of 70° is stable the most often. An apex half-angle of 50° is the most likely to flip over at 400 km, but $\alpha_0 = 45°$ is only marginally stable at 500 km.

When the Sun angle is set to 0°, all of the cases are classified as stable for 400 km and 500 km, although an interesting behavior appears, shown in Figure 4.13. The results during the normal simulation length of 10 hours show the short term oscillations damp down to approximately 0, but the angle the system is oscillating about is slowly increasing. This appears as if it is becoming unstable, but when the simulation is run for longer a long term periodic behavior is discovered. The amplitude of the peak is slightly decreasing for each subsesquent peak, so it will probably damp out eventually. This behavior is also seen when there is an initial angle of attack, but it is not as obvious because the amplitude of this behavior is only a few degrees. This behvaior is not yet understood.

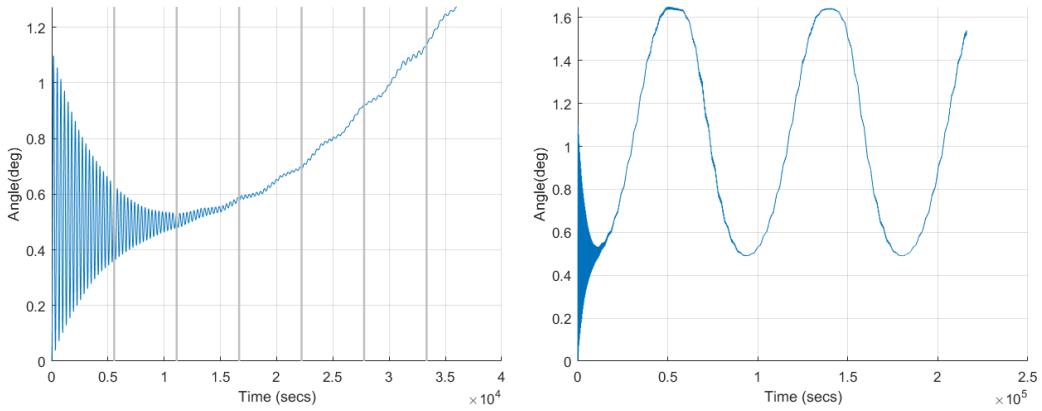

(a) Normal simulation length (10 hours) (b) Simulation length of 2.5 days

Figure 4.13: Long term periodic behavior when $\alpha_0 = 0°$ during wind tunnel mode.

4.5.3 Orbital Motion

The orbital motion version of the simulation has the highest fidelity in this investigation. This version of the simulation includes the gravity gradient torque for both simulations, and takes into account the relative positions of the Sun, Earth, and the moving spacecraft to include the satellite-sail system moving through the Earth's eclipse. The first analysis only includes aerodynamic and gravity gradient torques, and the second one includes all three disturbance torques. For orbital motion, the solar angle is replaced by the right ascension of the ascending node of the orbit.

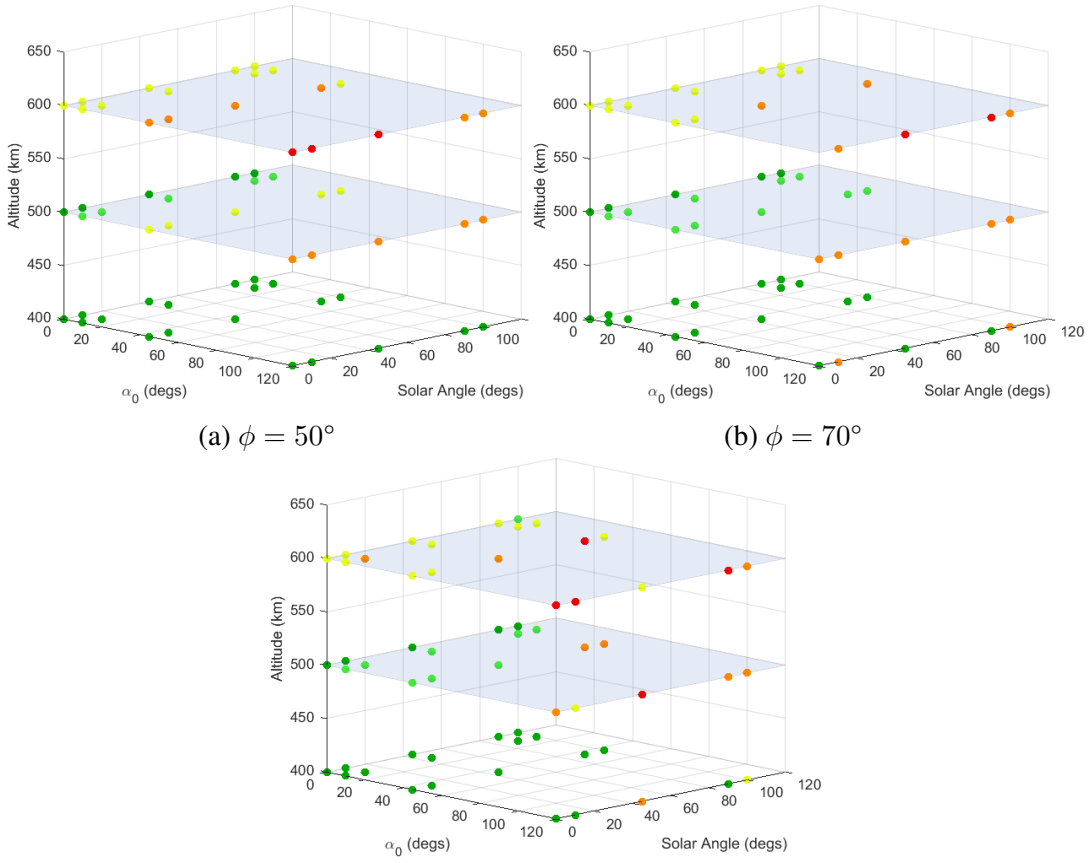

(a) $\phi = 50°$ (b) $\phi = 70°$

(c) $\phi = 80°$

Figure 4.14: Summary of the results from the wind tunnel simulation with aerodynamic, and solar radiation pressure torques.

Aerodynamics and Gravity Gradient

The results for the orbital motion simulation with aerodynamic and gravity gradient torques are shown in Figure 4.15, and the Ω of the orbit does not effect the results because the SRP is turned off. It can be seen that all three apex half-angles are either stable or relatively stable for 400 km and 500 km altitude, and marginally stable for 600 km. The aerodynamic torques are not quite strong enough to fully flip the sail when it starts at $\alpha_0 = 120°$ at an altitude of 600 km. There are more stable cases than wind tunnel mode meaning that the gravity gradient helps to stabilize the system.

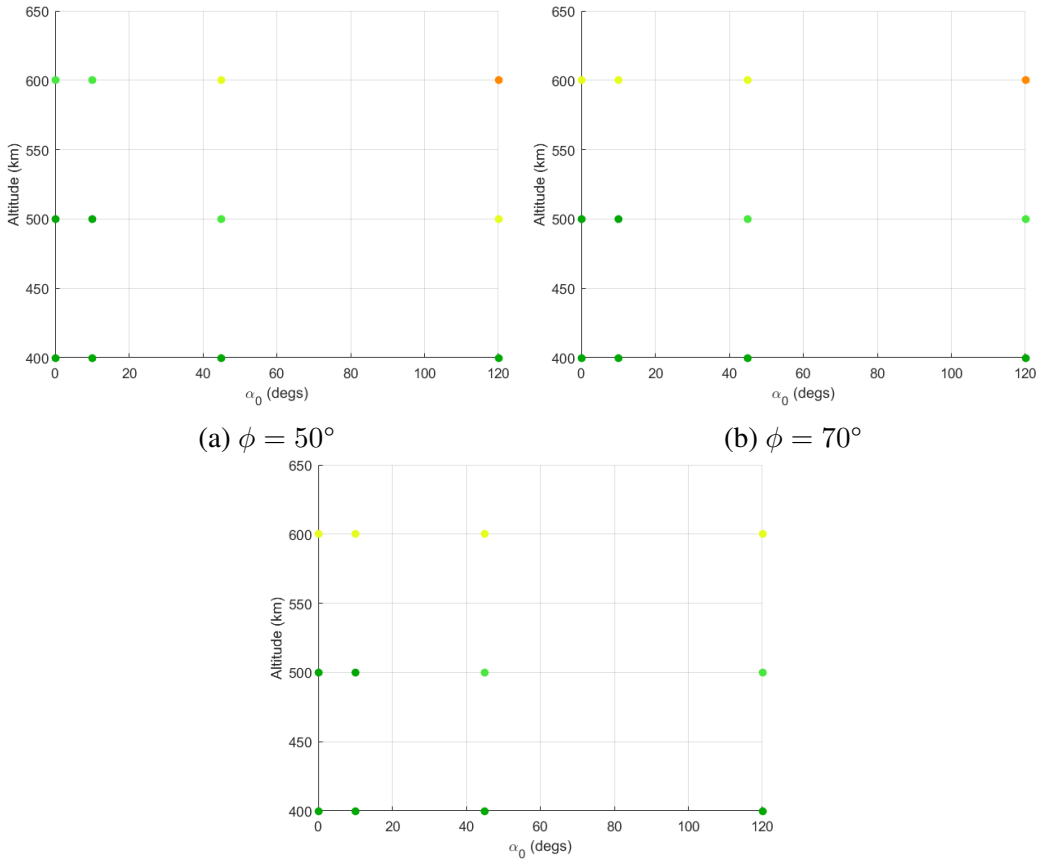

(a) $\phi = 50°$ (b) $\phi = 70°$

(c) $\phi = 80°$

Figure 4.15: Summary of the results from the full orbital motion simulation with aerodynamic and gravity gradient torques.

Aerodynamics, Gravity Gradient, and SRP

Adding SRP to the orbital motion simulation does not just add another torque as it did in wind tunnel mode because the SRP functions as a step input due to solar eclipse durations. This gives the SRP a greater capacity to disturb the stability. The results are summarized in Figure 4.16. At 400 km, most of the cases demonstrated that a sail that opens away from the flow will reorient itself facing the flow, but a few times the sail stabilized facing away or stabilized about an angle slightly offset from $\alpha_T = 0°$.

One example of a stable orbital motion case is shown in Figure 4.17 to demonstrate the effect of SRP. It can be seen by examing the SRP plot at the bottom that the satellite-sail system is in eclipse for the middle of the orbit. Although the initial angle of attack

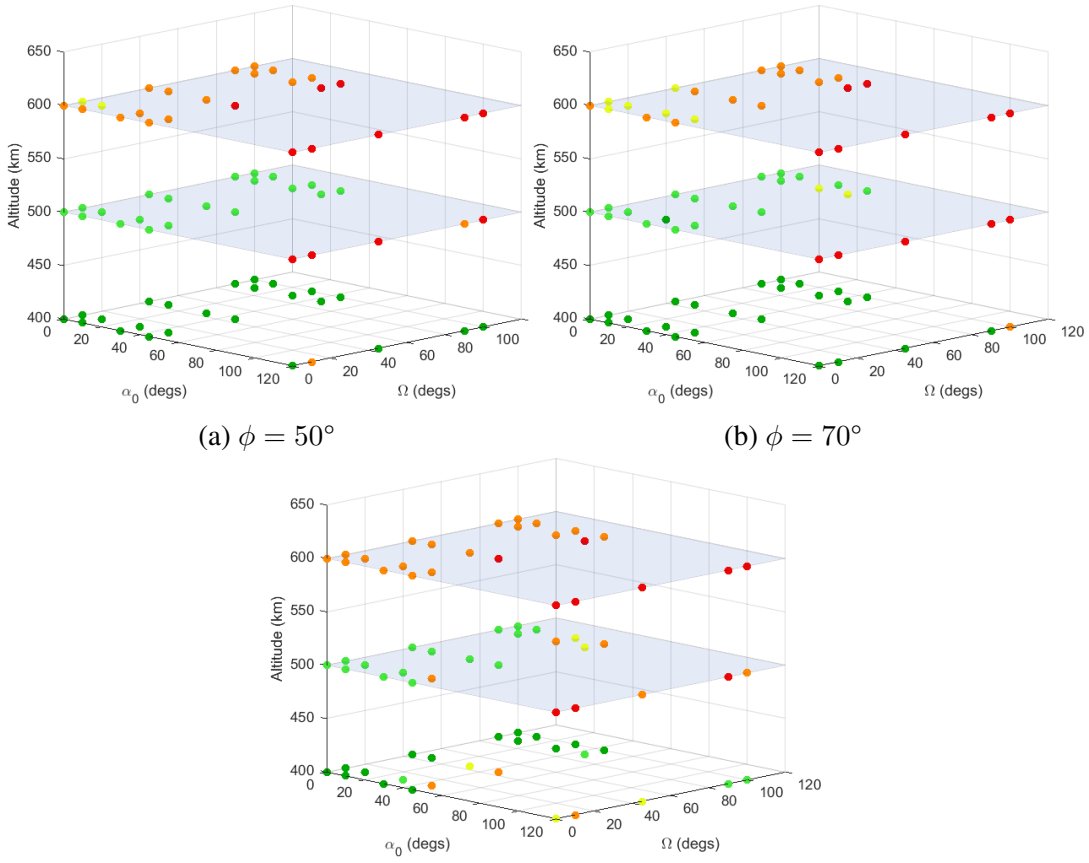

(a) $\phi = 50°$

(b) $\phi = 70°$

(c) $\phi = 80°$

Figure 4.16: Summary of the results from the full orbital motion simulation with aerodynamic, gravity gradient, and solar radiation pressure torques.

is $0°$, there is a slight disturbance from aerodynamics about the y-axis, which settles out. But, when the sail comes out of eclipse near the end of each orbit, the step input from SRP causes the aerodynamic torques to increase in the opposing direction to compensate, even though the aerodynamic torques are an order of magnitude higher than SRP. This is reflected in an uptick in the total angle of attack in the top figure. Overall, this is a small effect of only a couple of degrees, but is more significant when the aerodynamic torques are smaller at higher altitudes. That is why there are no stable cases at 600 km altitude.

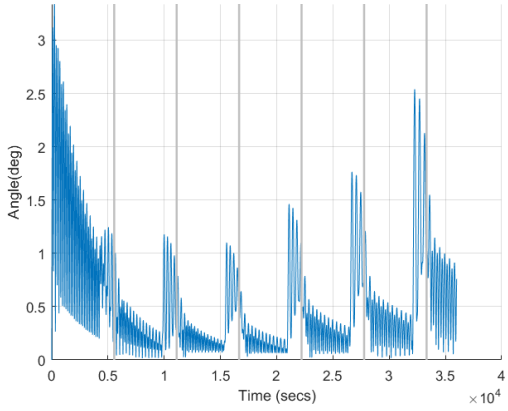

(a) Angle history

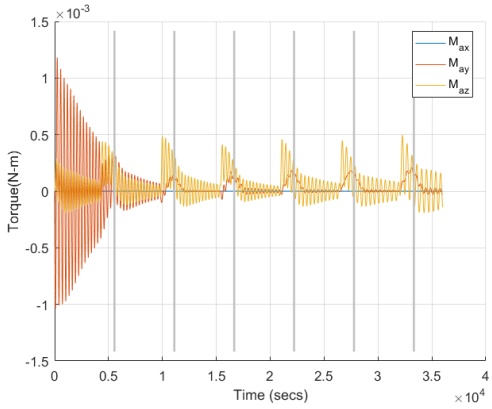

(b) Aerodynamic torque history

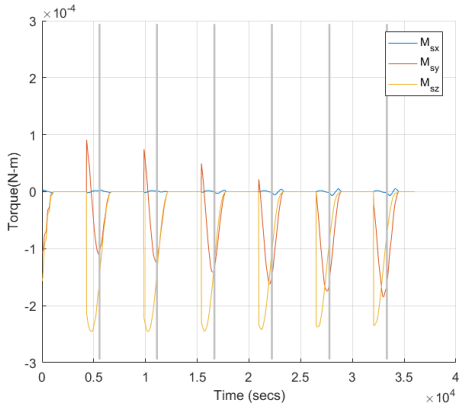

(c) SRP torque history

Figure 4.17: Behavior of a sail during the orbital motion simulation, specifically effects of SRP. $\phi = 70°$, $h = 400$ km, $\alpha_0 = 0°$, $\Omega = 45°$

4.6 Conclusions

For all four situations, $\phi = 50°$ is stable the most often, sometimes equal to $\phi = 70°$. $\phi = 80°$ has the fewest stable cases. This is in accordance with intuition because the

smaller the apex half-angle, the larger the distance between the center of pressure and the center of mass. The goal was to balance stability with drag creation, so the selected apex half-angle is $\phi = 70^\circ$ because the area of the base of the sail is larger for the same length booms.

This analysis is a good first attempt that clearly demonstrates the viability of aerodynamically stable designs for lower altitudes. Future work should replace the rigid body assumption with a flexible body model to increase the fidelity of the sail behavior. Also switching to a Direct Simulation Monte Carlo (DSMC) analysis will increase the fidelity of the aerodynamic forces.

CHAPTER 5
COMPONENT DESIGN AND PROTOTYPE TESTING

The $[PS]^2$ design has been established based upon the driving requirements and subsystem analyses discussed in Chapter 3. In this section, the design for the ESPA-class system is discussed, followed by the design and the prototype testing of the CubeSat-class system, specifically for the Aerodynamic Deorbit Experiment technology demonstration mission. The final section summarizes the differences between these two classes of systems.

5.1 ESPA-Class Design

The ESPA-class design of the drag sail in the deployed configuration is shown in Figure 5.1. In the stowed configuration, the full volume of the $[PS]^2$ assembly is 12 cm x 24 cm x 36 cm, equivalent to the 6U CubeSat standard, with a mass of 12 kg. The packaged volume of the system is sized based upon the boom dimensions, sizing of the four boom deployers, and accommodation of the four folded sail segments. The stowed volume of a deployable boom is determined by the stowed height and minimum wrap diameter, which are defined by the cross section and the maximum allowable strain of the materials, respectively [59]. As mentioned in the previous chapter, the SHEARLESS booms developed by NASA Langley were chosen for this system.

The SHEARLESS configuration selected is version 3 described by Fernandez in [59] because it is the version most thoroughly tested for mechanical properties. Both tape springs have the same design, with a radius of 19 mm, a subtended angle of 135.7°, and a three-ply carbon fiber layup of [45PW/0/45PW] [59]. The stowed height is 45 mm, and the minimum wrap diameter is 30 mm. Figure 5.2 shows the boom deployer, which measures 100 mm x 100 mm x 58 mm. The boom is mounted to, then wrapped around, a central hub that is able to spin freely with two guide rollers positioned to enforce the desired orienta-

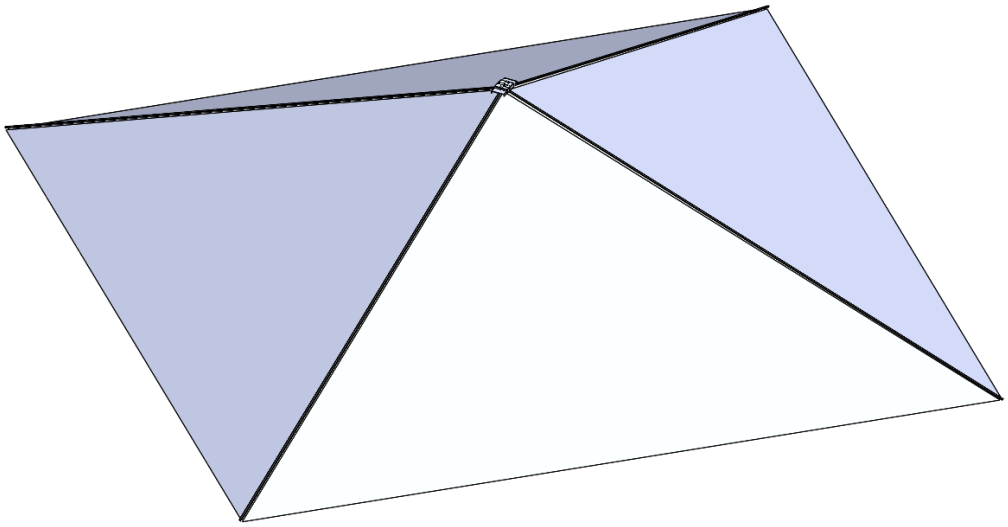

Figure 5.1: Deployed drag sail subsystem for the ESPA-Class concept.

tion of the boom. The design ensures the 70° apex half-angle for the square pyramid shape and supports the boom inside the deployer. Deployment of the 10 m booms will be controlled by a Faulhaber motor which regulates the deployment rate and helps to ensure that the booms are able to unfold the sail quadrants during deployment. It is important for the boom to regain its full cross section at the root when fully deployed in order to maximize its stiffness.

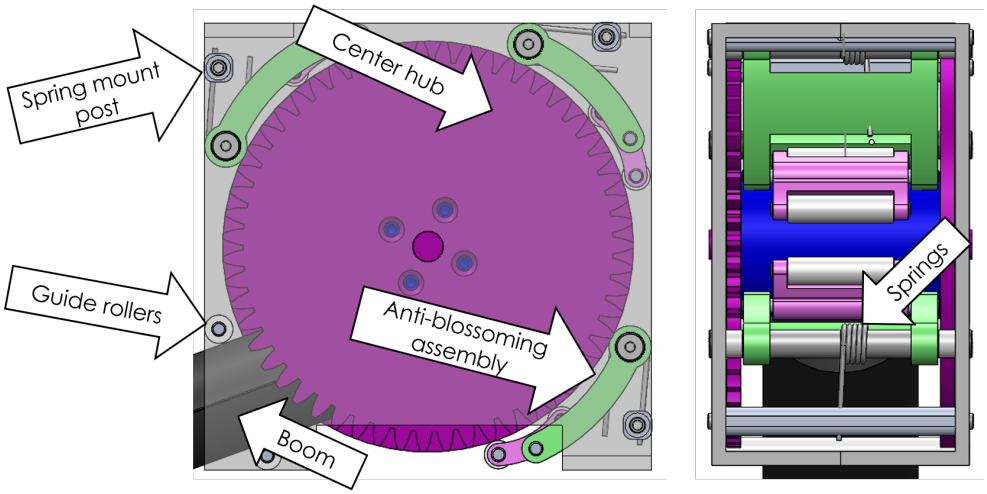

Figure 5.2: Labeled boom deployer for the ESPA-class concept

Rocker arms with hands are included in the deployer mechanism to prevent boom blossoming. Blossoming occurs when the coils of a boom do not rotate with the same angular velocity as the hub, rather, the layers slide with respect to each other and expand to a lower energy state. Blossoming typically occurs partway through the deployment and causes the boom to jam inside the deployer, risking damage to the boom at the root. A common way to prevent this is by applying a normal force to the outside of the boom roll at regular intervals around the circumference [61]. Figure 5.3 shows the anti-blossoming assemblies for the $[PS]^2$. Force is applied on the rocker arms by torsion springs that are restrained by the spring mount posts. Rocker hands are pressed against the outside of the boom roll continuously as the outer diameter shrinks while the boom deploys. The rocker arm and hand design enables six points of contact on the boom room while only needing three assemblies. If blossoming were to occur, it would begin as small bulges in the boom roll. The rocker hands can pivot around the bulges, allowing the boom to continue to deploy. In contrast, if using only a rocker arm, the deployment could potentially stall. Sobey and Lockett describe this as the most effective way to control blossoming, according to their testing [92].

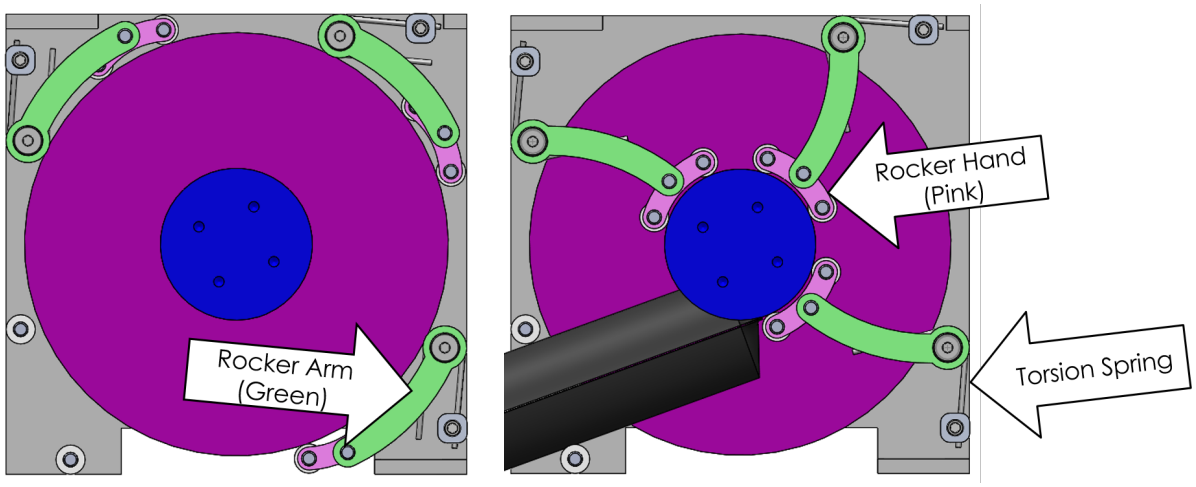

(a) Boom stowed (b) Boom deployed

Figure 5.3: The boom deployer shown with the boom stowed and deployed. Blossoming is prevented by the rocker hand that is attached to the rocker arm.

The sail membrane is divided into four membrane quadrants for ease of packaging, deployment, and survivability. Risks associated with the sail membrane are proper stowing and extraction from the drag sail assembly and degradation of the material following deployment due to the space environment. Corin is the selected sail material because it creates a protective layer of silicon dioxide as it is subjected to atomic oxygen erosion [98, 44], allowing the membrane to maintain structural integrity for long durations in space. Another option is to increase the thickness of the material to account for the erosion, which would make it more difficult to package. The sail membrane is packaged using the efficient Z-folding design which results in a long thin rectange that is wrapped around a spool, as was done for Nanosail-D and NEAScout [44, 114].

The estimated volume is 12 cm x 24 cm x 24 cm, including volume for batteries and an avionics board. Figure 5.4 shows the conceptual stowed assembly and two different layouts for the boom deployers are shown. Both configurations have adequate volume to accommodate sail quadrants that are Z-folded then rolled around a hub, as shown in Figure 5.5. Prototypes of each configuration will be built and tested to evaluate system performance and establish a baseline.

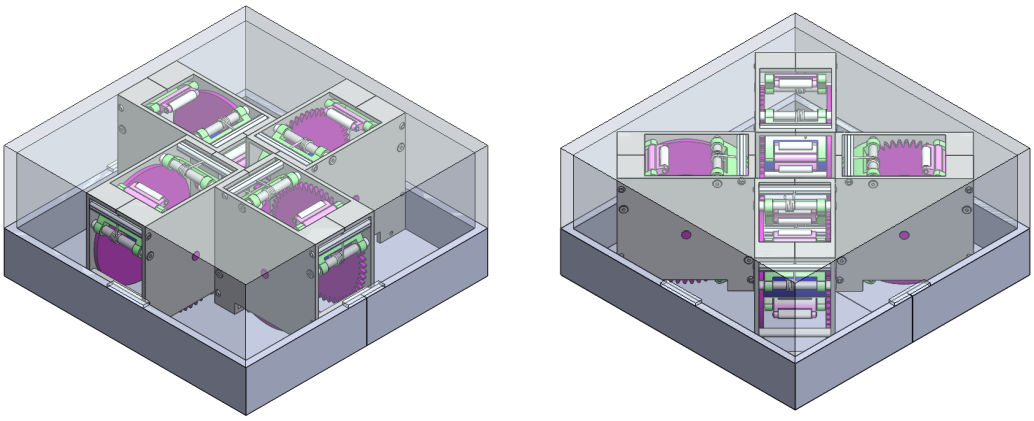

(a) Straight arrangement (b) Diagonal arrangement

Figure 5.4: The ESPA-class system with two different arrangments of the boom deployers.

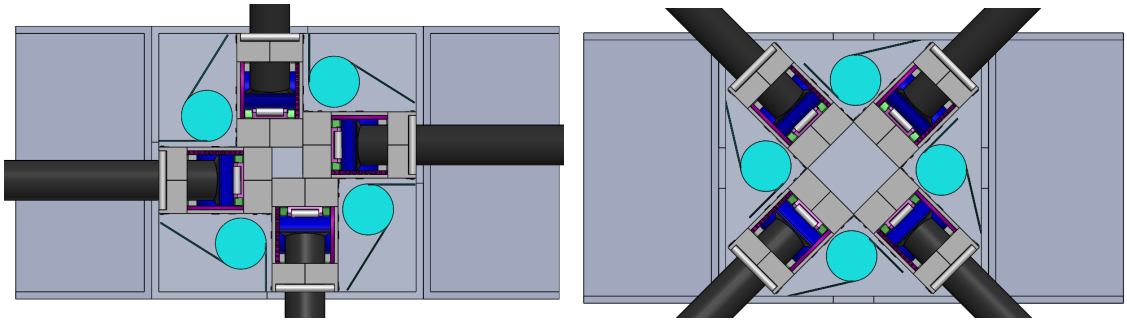

(a) Straight arrangement (b) Diagonal arrangement

Figure 5.5: The ESPA-class system viewed from the bottom, including conceptual sail membrane rolls.

5.2 CubeSat-Class Design

The CubeSat-class $[PS]^2$ system is designed to deorbit CubeSats ranging from 1U to 27U. A detailed design has been developed for the 0.5U (10 cm x 10 cm x 5 cm) assembly, which has 1 m boom lengths. This smallest version of the $[PS]^2$ is suitable for the deorbit of 1U, 3U, and 6U CubeSats, as shown in Table 3.1. The design is scaled upward to accommodate 12U and 27U CubeSats.

The 0.5U $[PS]^2$ assembly will be demonstrated in the Aerodynamic Deorbit Experiment (ADE) mission, planned for launch in 2019 as part of the United Launch Alliance STEM CubeSat program. ADE is a 1U CubeSat that will be deployed into a geosynchronous transfer orbit with an apogee altitude of 35,756 km and a perigee altitude of 185 km [115]. It is estimated that the CubeSat will deorbit within 80 days after deployment of the drag sail. Without a drag sail, the deorbit period would be seven years or more. ADE will fly an inertial measurement unit to measure the CubeSat attitude rates and acceleration during atmospheric drag passes. A camera integrated into one of the CubeSat side panels will be used to capture images of drag sail deployment. Figure 5.6 shows the design of the drag sail sub-system. The strict volume constraints of the ADE mission created a number of design challenges that will be discussed in the following sections.

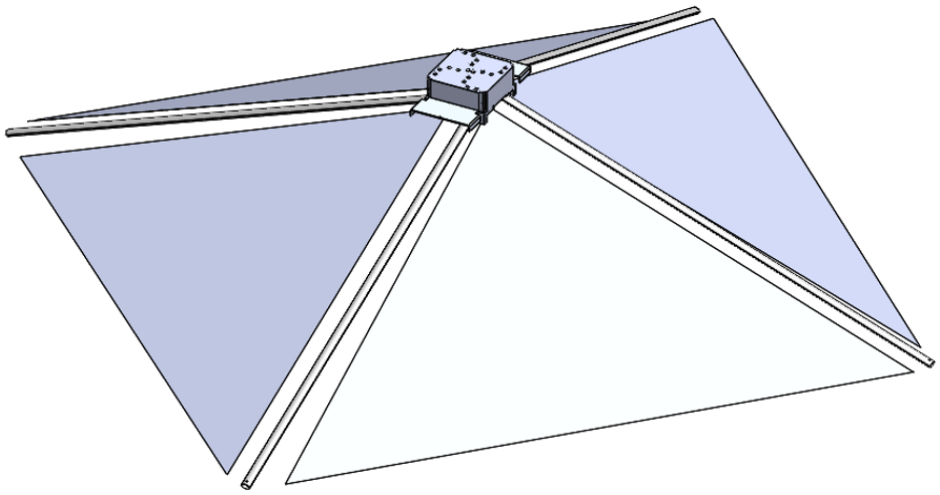

Figure 5.6: Deployed drag sail subsystem for the Aerodynamic Deorbit Experiment.

5.2.1 Design of Drag Sail Subsystem

The drag sail assembly is designed to be self-contained in-order to reduce CubeSat integration complexity, as shown in Figure 5.7. The outer casing includes the feet required by the CubeSat standard [116], and will take the load during launch. Two doors restrain the booms and sails; when deployment is iniated by a burn wire, they open. Each sail quadrant is folded separately and stored next to a boom deployer, as shown in Figure 5.8 where the sail compartments are outlined in yellow and the boom deployers are outlined in red.

NASA Langley engineers helped to design the SHEARLESS booms to fit within the volume constraint, which was a driving requirement for both the boom selection and the deployer design. One meter booms may be deployed using internal strain energy, which eliminates the need for a deployment motor and gears. The tape spring radius of 8 mm (5/16") was chosen to maximize the moments of inertia in both x and y directions (as defined in Figure 3.5) using the equations defined by Fernandez [59]. The final stowed height of the tape springs is stowed height of 20 mm. They are made from three-ply carbon fiber composites with a [45PW/0/45PW] layup. Four-ply layups were also investigated, but they were too thick to accommodate the full length of the boom in the deployer. The boom deployer, shown in Figure 5.9, is designed similarly to the full-scale system with a

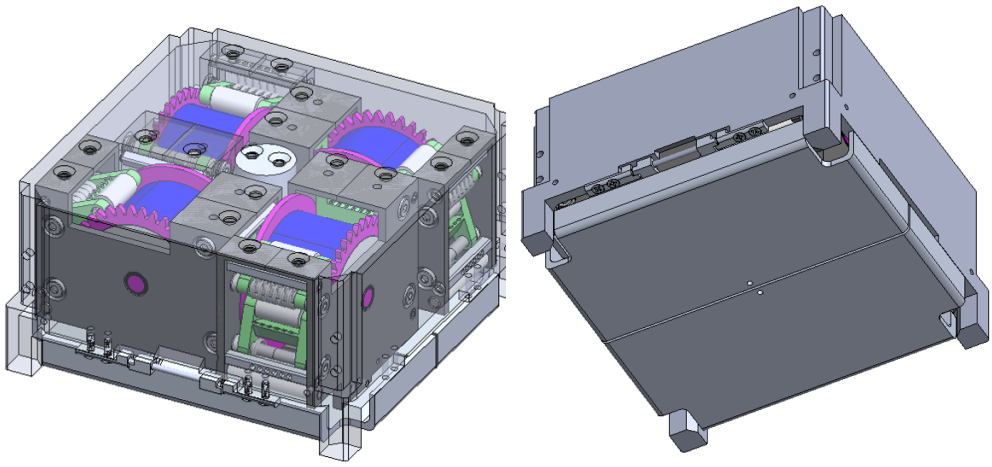

(a) (b)

Figure 5.7: (a) Top view of contained drag sail system with transparent outer casing and (b) bottom view to show doors.

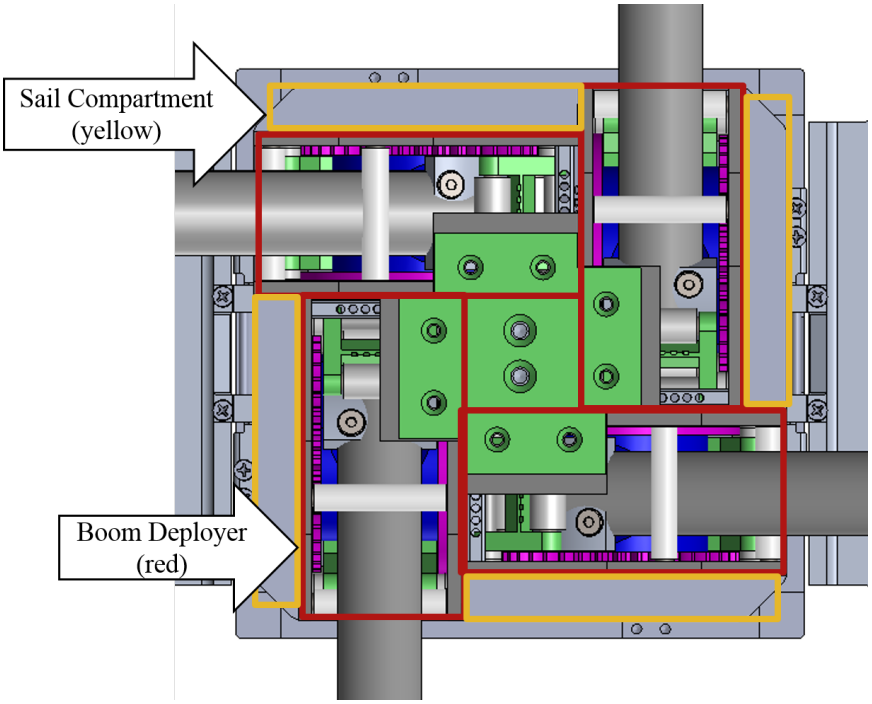

Figure 5.8: Bottom view of deployed drag sail assembly with sail quadrants hidden. Sail compartments are marked in yellow and boom deployers are marked in red.

freely rotating center hub and guide rollers positioned to ensure a 70° apex half-angle. The primary difference between the full-scale and cubesat systems is that the anti-blossoming assemblies only contain rocker arms, resulting in only one point of contact on the boom

roll per assembly. This design was necessitated by the deployer volume constraints, so a fourth anti-blossoming assembly was added to the system to compensate. Force is applied by torsion springs that are restrained by the spring mount posts. Each assembly is capable of holding up to six springs, but the actual number of torsion springs will be determined via prototype testing, as described in the following section.

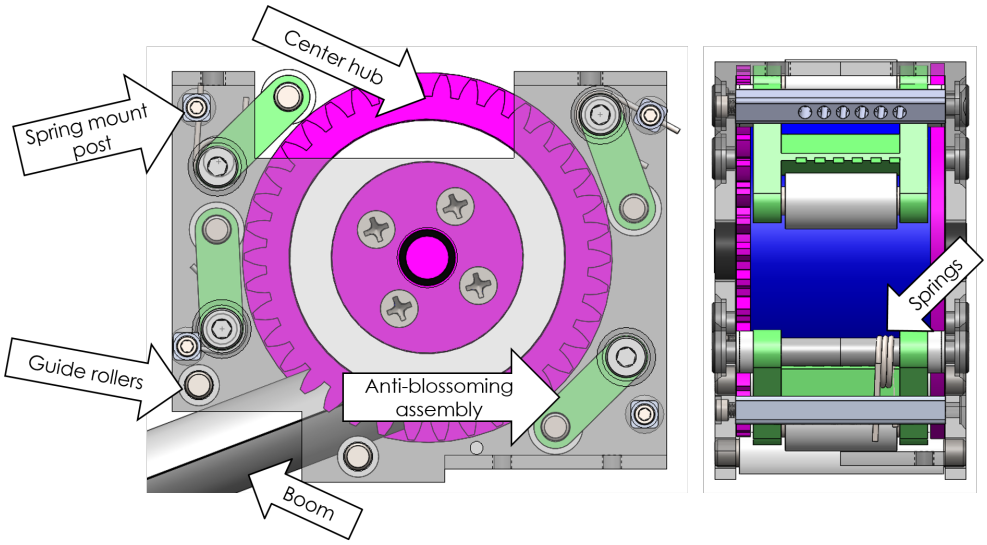

Figure 5.9: Boom deployer front view with transparent structure (left) and side view (right).

For the ADE mission, it was determined that 5 µm thick CP1 is adequate for the short mission duration [96]. For CubeSat missions with longer deorbit periods, Corin will be used as the sail material. The risk of the sail membrane being destroyed by collisions with micrometeoroids and orbital debris is mitigated by dividing the sail into four quadrants, and then adding ripstops to prevent the propgation of tears. Ripstops are created by making a grid of Kapton tape on the surface of the membrane; a tear is only able to propagate to the nearest line of kapton. Smaller grid sections reduce vulnerability to debris impacts, but locally increases the thickness of the membrane. Ripstop lines are not perpendicular to the folds or else they will stack on top of each other, increasing the folded size. With these design parameters in mind, the ripstop pattern was designed with evernly spaced lines parallel to the hypotenuse edges, as shown in Figure 5.10. If one of the square elements between ripstops is completely destroyed, only 12% of the quadrant area and 3% of the

total membrane area will be lost. The available volume for sail quadrants in the ADE system does not allow for the same rolled packaging scheme described for the full-scale system. Instead, the sail will be folded into the Frog Legs pattern, as proposed by Dalla Vedova, et al [117]. It consists of Z-folding the sail into a strip, then Z-folding the ends into the middle. This allows all three corners of the sail quadrant to be free for mounting, and provides minimal friction during deployment.

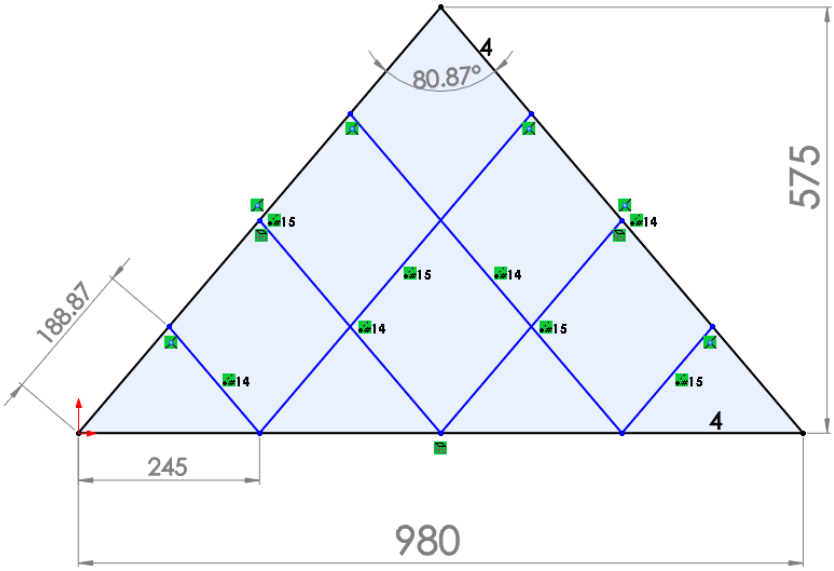

Figure 5.10: Sail quadrant ripstop pattern, dimensions in mm [118].

5.2.2 Prototype Testing

Prototype testing has been performed for the 0.5U $[PS]^2$ assembly. Initial fit-checks and unit-level boom deployment tests were performed using 3D printed materials. A number of iterations of the design that were printed on an Ultimaker 2+ machine with PLA, a MarkForged MK-2 machine with black nylon, a Stratasys Dimensions machine using PLA, and an Afinias H800 machine using ABS. Each printer used a different color material, as can be seen in Figures 5.11 and 5.12; the Ultimaker parts are grey, the MarkForged parts are black, and the Stratsys parts are cream. When the boom is spooled, the tape springs are

no longer the same length (see Figure 5.12). This is due to the fact that the tape springs slide relative to one another and it requires more flexibility in the design for mounting the sail quadrants to the boom tips. Testing of the boom deployer consisted of first assembling it with one spring per anti-blossoming assembly, rolling up the boom, and determining if the boom would freely deploy. It was determined that only one spring was needed per anti-blossoming assembly to prevent blossoming and to allow the boom to freely deploy. Subsequent engineering and flight unit boom deployers will be machined out of aluminum to provide strength and rigidity.

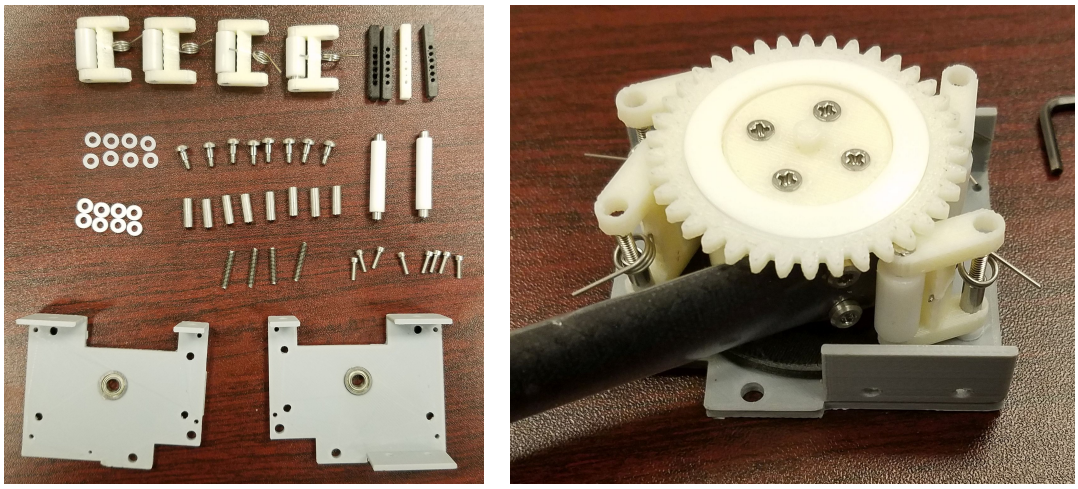

(a) (b)

Figure 5.11: PLA Deployer (a) fully disassembled and (b) partially assembled.

To facilitate boom deployment testing and integration with the spacecraft bus, boom winding mechanisms and boom locks are required. As shown in Figure 5.13, the boom locks slide onto the wall of the deployer frame and interfaces with the center hub gear to prevent deployment. The prototype boom lock was made out of three pieces of wood that were laser cut to the correct shape and then bonded together with epoxy. Figure 5.14 shows the gear winding assembly. The purpose of the frame is to provide alignment and restraint for the gear that interfaces with the gear flange. This has a hexagonal hole for an Allen wrench to be inserted and turn the gear to wind up the boom. This assembly requires the boom to be flattened and guided into the deployer as the center hub is being turned.

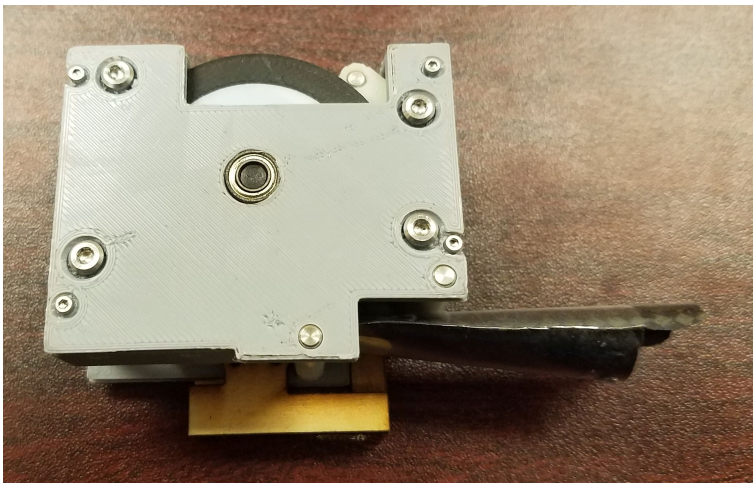

Figure 5.12: Assembled PLA boom deployer with fully stowed boom.

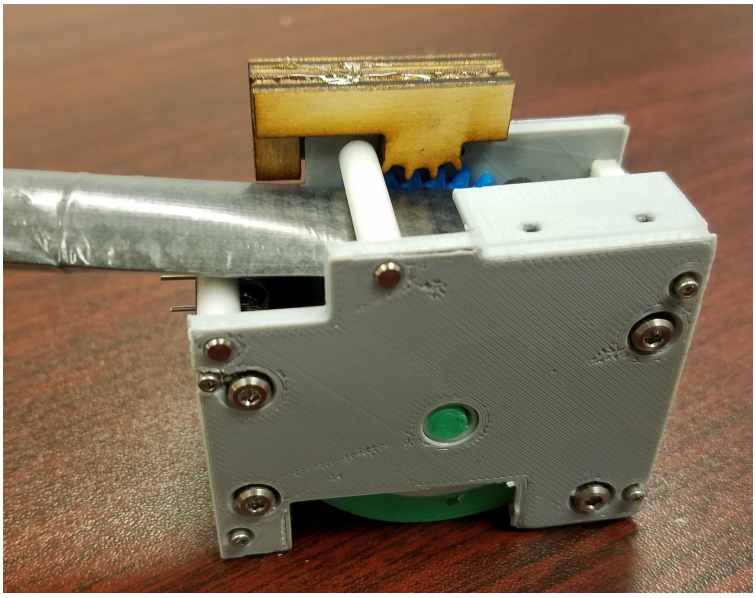

Figure 5.13: Boom partially stowed and held in place by the wooden boom lock prototype.

The sail prototype consisted of 5 µm thick CP1, shown in Figure 5.15. Edge reinforcements and ripstops were taped using 12.7 mm wide kapton tape. A teflon coated wire was used to create each fold by holding it tightly on top of the membrane while the unfolded membrane was passed over it. The wire was then pulled out of the fold and lain on the other side. Figure 5.16 shows the sail being folded with many volunteers ensuring the folds stay in place. The green Teflon wire can be seen in the bottom right corner as it is being held under tension. As more of the membrane was folded, binder clips were used to secure

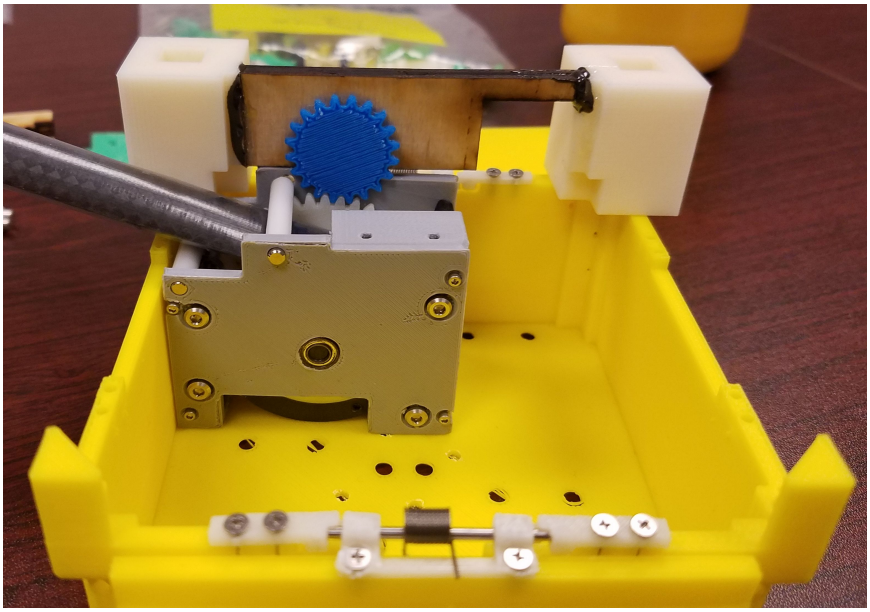

Figure 5.14: Gear winding assembly mounted on the payload frame interfacing with the boom deployer.

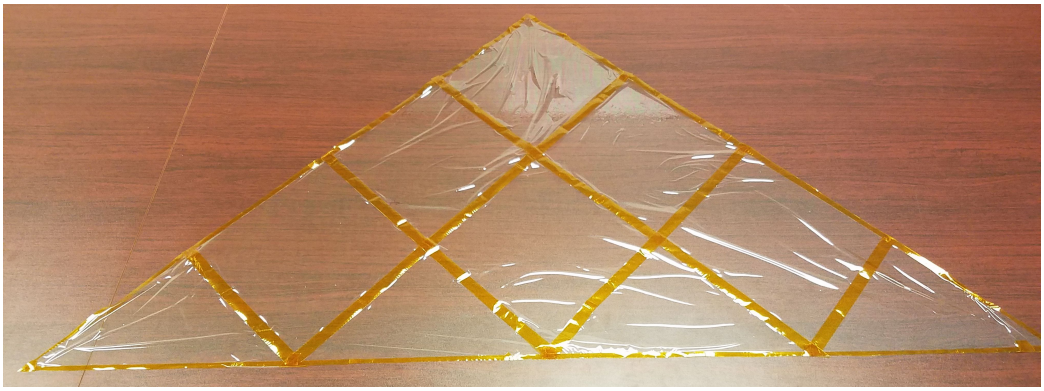

Figure 5.15: CP1 sail prototype with kapton ripstops [118].

the folds. Figure 5.17 shows the sail after the first folding phase. Note that the rip stops did not stack on top of each other, reducing the thickness of the folded sail. The next phase was to fold both sides of the sail into the center. Figure 5.18 shows the fully folded sail in the allocated volume of the 3D printed structure. The mounting points in the sail are located at each corner and are created by reinforcing the CP1 with two layers of kapton tape on each side, then mounting a grommet in each corner, as seen in Figure 5.19. A loop of wire is strung through the hole in the boom that is long enough to account for the mismatch of the rolled tape springs, then an extension spring is used to connect the wire to the grommet.

The springs keep tension on the sail membrane as it expands and contracts due to thermal effects. The foot of the sail membrane is mounted directly to the $[PS]^2$ assembly using a small loop of wire.

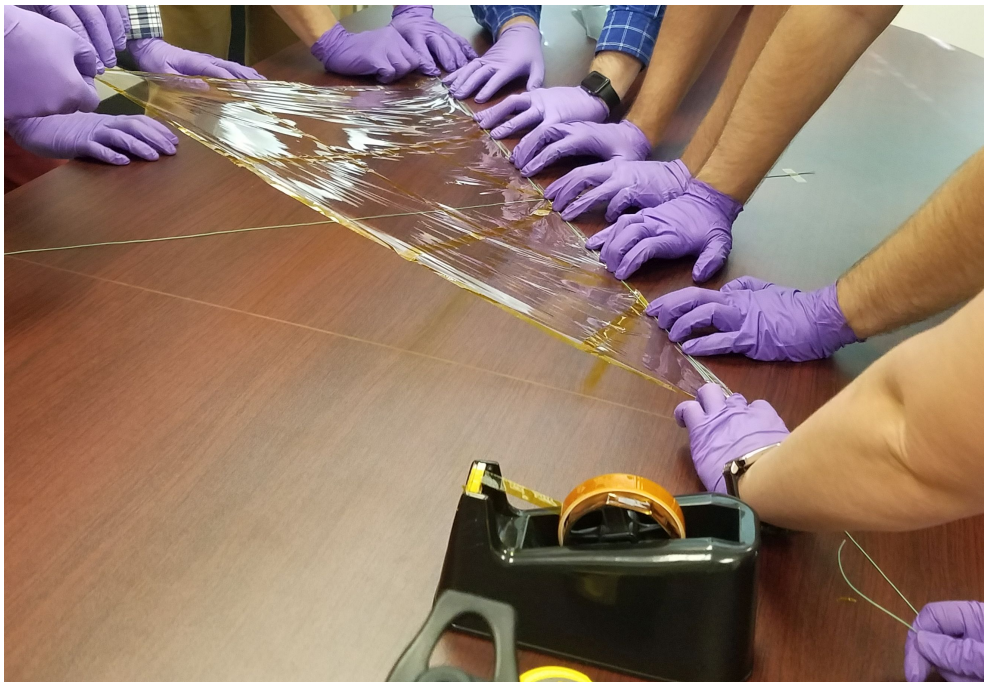

Figure 5.16: Folding process. Note the green Teflon wire used to define the folds [118].

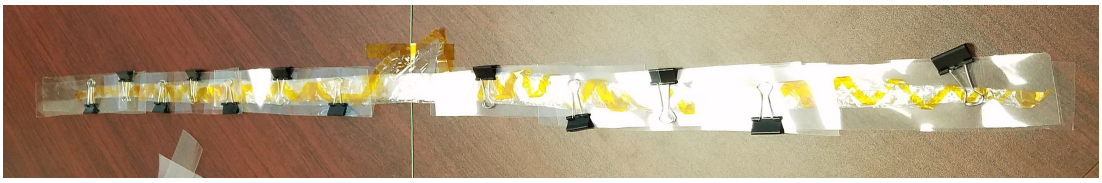

Figure 5.17: CP1 prototype after initial folding phase [118].

5.3 Design Differences between the ESPA-class and CubeSat-class

As mentioned previously, the highly constrained volume of the CubeSat-class system requires several modifications relative to the ESPA-class design. Table 5.1 summarizes the differences between the two systems. It is noted that the 10 m booms in the ESPA-class system provides a 125x increase in the effective drag area relative to the 1 m booms in

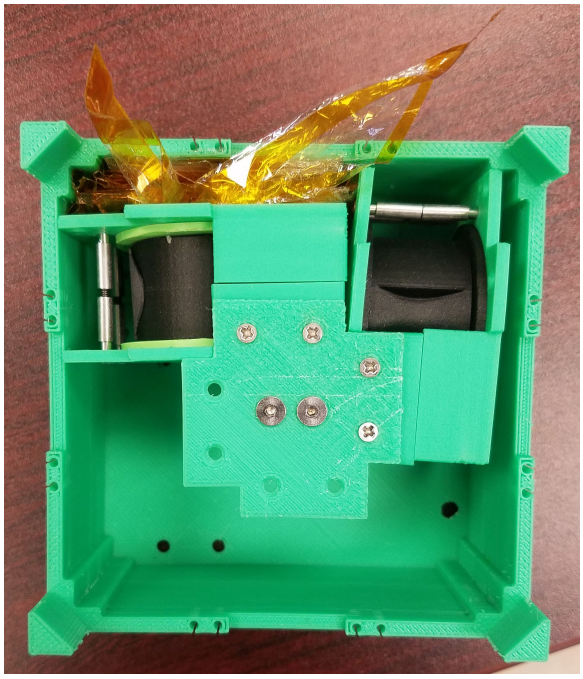

Figure 5.18: Fully folded CP1 sail quadrant in the allocated volume of a 3D printed prototype [118].

Figure 5.19: Grommet attached to the corner of the sail.

the CubeSat-class system. While ESPA-class system requires motor-controlled boom deployment, the larger volume eases the packaging constraints and allows for a more elegant

design for the anti-blossoming devices. Overall, the design scales well from the CubeSat-class to ESPA-class system [71].

Table 5.1: Summary of the design differences between the ESPA-class system and the CubeSat-class system.

Parameter	**ESPA-class**	**CubeSat-class**
System Mass	12 kg	0.75 kg
System Dimensions	112.5 x 240 x 240 mm	51.25 x 100 x 100 mm
System Volume	6.48×10^{-3} m^3	5.13×10^{-4} m^3
Apex Half-Angle	70°	70°
System Drag Area	143 m^2	1.13 m^2
Deployment Method	Motor driven	Internal strain energy
Boom Type	SHEARLESS	SHEARLESS
Boom Stowed Height	45 mm	20 mm
Boom Shell Radius	19 mm	7.94 mm
Boom Length	10 m	1 m
Boom Hub Diameter	33 mm	30 mm
Boom Deployer Size	100 x 100 x 58 mm	46 x 57 x 47.5 mm
Anti-Blossoming Mechanism	Two contact points each	One contact point each
Sail Material	Corin	CP1/ Corin
Sail Thickness*	2.5 μm	5 μm
Sail Folding	z-folded then rolled	Frog-legs

*Thickness loss estimated from the Nomogram in [98] and using Erosion Yield numbers from [99, 100]. Erosion Yield approximately CP1 = 2×10^{-24}, Corin = 5×10^{-26}.

CHAPTER 6
CHARACTERIZATION OF SHEARLESS BOOMS

A SHEAth-based Rollable LEnticular-Shaped and low-Stiction (SHEARLESS) composite boom is a type of deployable boom designed to have a high packing efficiency [119]. These booms are comprised of two composite tape springs coupled together by a tight-fitting flourinated ethylene propylene (FEP) sleeve to allow for thinner stowed booms and a smaller diameter around which they are wrapped. Previous testing with these booms included some torsion testing, but was mainly focused on the application of mounting and stowing the booms for a flight design. This research describes torsion and bending tests for two new cross sections to determine the mechanical properties. The goal of this testing is to provide data for the creation of a finite element model in order to enable satellite designers to evaluate if these booms will fulfill the requirements of specific missions and increase the usage on flight missions. To date, these booms have only been used on an Undergraduate Student Instrument Project experiment conducted by the University of Nebraska as a retractable boom design for sounding rocket payloads [120].

6.1 SHEARLESS Description

The SHEARLESS booms are categorized by the stowed height of the configuration. In this study two stowed heights were used: 45 mm and 20 mm. The parameters that fully define the cross section are listed in Table 6.1. Fernandez previously conducted torsion testing for a 45 mm boom with $R_{sh} = 16$ mm and $\alpha_{sh} = 161.1°$ [59], but a new test setup was desired. The smaller 20 mm booms were chosen for the tight volume requirements of the ADE mission described in Chapter 5. Both booms used the same layup directions for the composite, $[45°PW\backslash 0°\backslash 45°PW]$, but used different materials, resulting in different laminate properties that are summarized in Table 6.2.

Table 6.1: Cross-section parameters for the two SHEARLESS versions used in testing.

Boom Stowed Height	Shell Radius (R_{sh})	Shell Thickness (t_{sh})	Subtended Angle (α_{sh})
45 mm	19 mm	0.215 mm	135.7°
20 mm	7.94 mm	0.153 mm	138.3°

Table 6.2: The composite materials and resulting laminate properties for the two SHEARLESS booms.

Boom Stowed Height	Unidirectional Material	Plain Weave Material	E	G_{xy}
45 mm	MR60H	HTA40	47.0 GPa	27.4 GPa
20 mm	M46S	M30S	61.8 GPa	38.0 GPa

Since the two tape springs are not bonded together, there are three states that the tape springs can take inside the sleeve. The first is the fully coupled state where the edges of the tape springs are lined up for the entire length of the boom, as seen on the left in Figure 6.1. Shown on the right us the other extreme, known as uncoupled, where the edges are not lined up at all. The third state is the intermediate one, known as partially coupled, where the tape spring edges are lined up for part of the length of the boom, and not lined up for other parts. The coupled state should have the highest stiffness in both bending and torsion, and the uncoupled state the lowest. This is most noticeable in torsion. When the boom is flattened, stowed, then deployed, it will most likely be partially coupled. These characterization tests function to provide upper (fully coupled) and lower (fully uncoupled) bounds for both bending and torsional stiffness.

6.2 Theory

It is difficult to calcualte the theoretical bending and torsional stiffness for the SHEARLESS booms because the contribution of the sleeve is unknown. Fernandez estimated an area moment of inertia for a SHEARLESS boom about the x and y axes, as defined in Figure 6.1, by assuming the tape springs are fully coupled during bending. Equations (6.1)

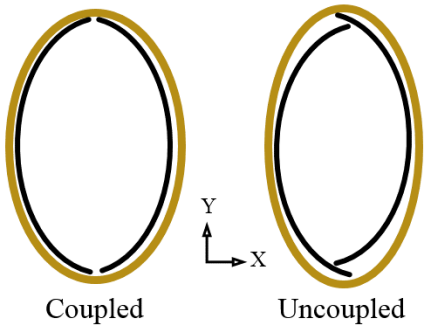

Figure 6.1: The two extreme states of the tape springs inside the sleeve.

and (6.2) are the result of taking the sum of the area moments of inertia of the individual tape springs [59].

$$I_{xx} = R_{sh}^3 t_{sh}[\alpha_{sh} - \sin\alpha_{sh}] \tag{6.1}$$

$$I_{yy} = 2R_{sh}^3 t_{sh}[\frac{\alpha_{sh} + \sin\alpha_{sh}}{2} - \frac{2 - \cos\alpha_{sh}}{\alpha_{sh}} + \alpha_{sh}\{\frac{\sin(\alpha_{sh}/2)}{(\alpha_{sh}/2)} - cos(\alpha_{sh}/2)\}] \tag{6.2}$$

For the torsional stiffness, the contribution of the sleeve is more significant. Lee and Fernandez [121] estimated the torsional constant for a closed cross section in Equation (6.3) and an open cross section in Equation (6.4) by using trigonometry to discretize the cross section of a generic boom into small rectangular sections. Let any given segment be denoted with the subscript $j = 1, ..., m$, where m is the total number of segments; l_j and t_j are the length and thickness of each segment. A_E is the total enclosed area in the closed section.

$$J_c = 4A_E^2 / \sum_{j=1}^{m} \frac{l_j}{t_j} \tag{6.3}$$

$$J_o = \sum_{j=1}^{m} \frac{1}{3} l_j t_j^3 \tag{6.4}$$

In this case, l_j is the arc length of the boom divided by m, and t_j is the thickness of the tape springs. The area moments of inertia values are combined with the laminate properties in Table 6.2 to determine the theoretical stifness values shown in Table 6.3.

Table 6.3: Theoretical stiffness values for the SHEARLESS booms.

Boom Stowed Height	EI_{xx}	EI_{yy}	GJ_c	GJ_o
45 mm	115.75 N-m^2	107.49 N-m^2	95.16 N-m^2	0.0082 N-m^2
20 mm	8.28 N-m^2	7.81 N-m^2	7.38 N-m^2	0.0017 N-m^2

The bending stiffness values are assumed to be an upper bound because the area moment of inertia assumes the booms are fully coupled. For torsional stiffness, SHEARLESS booms cannot be considered either fully open or fully closed because the sleeve provides a constraint, but the booms are not nearly as constrained as if the tape springs were bonded together. Therefore, the closed and open torsional stiffness values are considered to be upper and lower bounds respectively. The fully coupled case should behave similar to the closed cross section and the fully uncoupled case should behave simlar to the open section. A partially coupled boom should have a stiffness between the other two values.

6.3 Test Setups

Two test setups were used to obtain the mechanical properties of the booms. Torsion tests were conducted first because they are non-destructive and the length of the boom is not important. The bending test was conducted until the boom buckled, which is a failure of the boom, and was shown to sometimes damage the composite tape springs. Buckling is dependent on the length of the boom, so the samples were shortened from the torsion test to try to make the boom fail near the center. Both test setups were inspired by Leclerc et al at the California Institute of Technology [122].

A primary aim in the design of these test setups was to test booms with different cross sections with minimal alterations to the hardware and testing procedures. This was accomplished with the use of 3D printed clamps to mount the booms. Figure 6.2 shows the 3D printed clamp for the 20 mm boom in the torsion test setup. The piece mounted to the torque sensor has a plug that is inserted inside the end of the boom, then two outer pieces are attached on the outside to clamp the end and ensure it is fixed. All three pieces were designed for each specific boom cross section and can easily be redesigned for new shapes. The test setups were designed by Brandon Warren of the University of Nebraska, while the test data was collected and analyzed by the author of this dissertation.

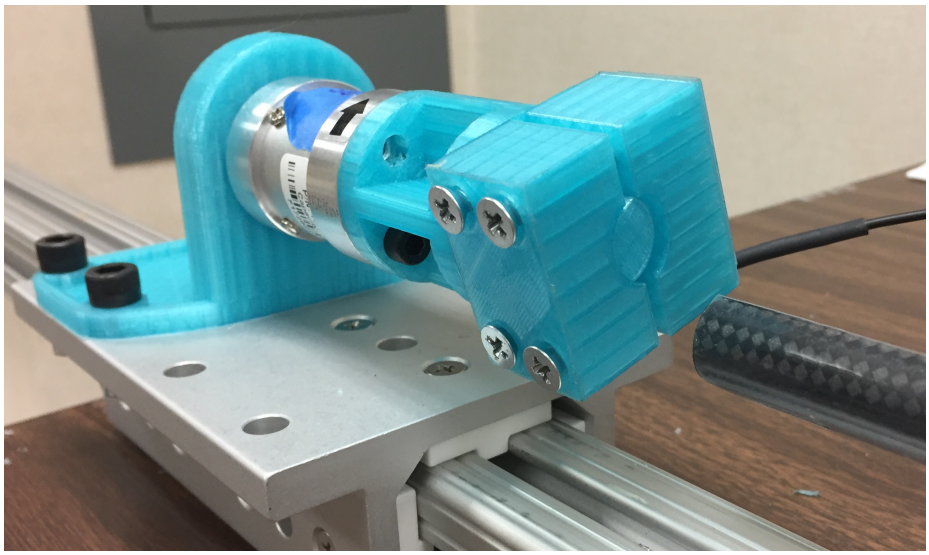

Figure 6.2: 3D printed boom clamp mounted to the fixed end of the torsion test rig.

6.3.1 Torsion Test

The main operational requirement for the torsion test setup is to apply the load through the centroid of the boom. Figure 6.3 shows the test setup with a 20 mm boom mounted. The apparatus consists of one fixed end (shown on the left) mounted to the base, and a rotating end (shown on the right) that is fixed to a motor that applies the torsional loads. Both ends include a torque sensor to measure the loads imparted on the boom. The angle of rotation was recorded from the encoder that drove the motor, and from a video of the rotating end of

the boom. A white flag was attached to the boom mount to enable tracking of the rotation.

The torsional stiffness was determined by finding the slope of the torque vs. twist curve using Equation (6.5). SHEARLESS booms do not have enough torsional stiffness to fail, so the booms were rotated 100°, held for five seconds, then rotated back to the starting position. Each boom was tested three times in the counter-clockwise direction and three times in the clockwise direction for when the tape springs are fully coupled and fully uncoupled. Each boom was also tested three times in the clockwise dirction when it was partially coupled, for a total of 15 tests for each boom. Two booms were tested for each size, all were about 1 m long.

$$GJ = (\frac{dM}{d\theta})L \tag{6.5}$$

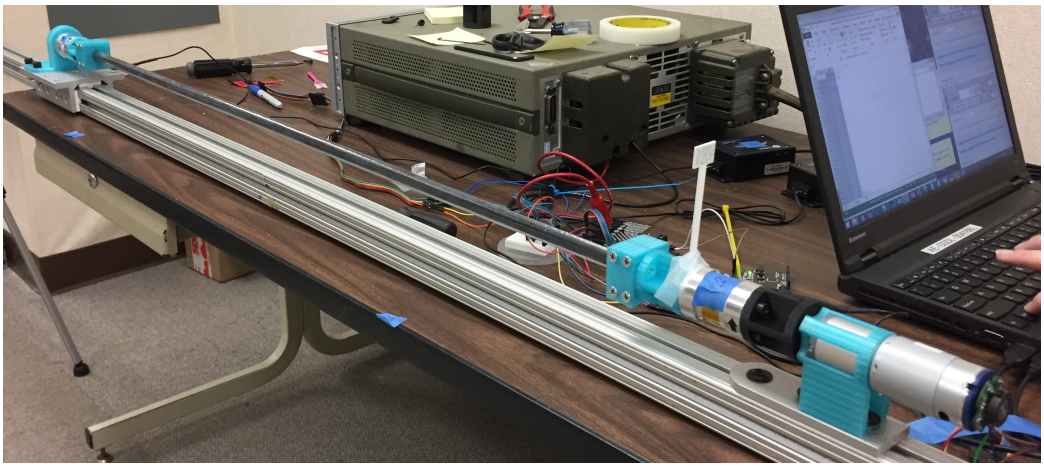

Figure 6.3: Torsion test setup with the fixed end on the left and the rotating end on the right.

6.3.2 Bending Test

The main requirement for the bending test is to apply equal angle to each end of the boom to ensure equal bending moments. This is accomplished by synchronizing the motors that are applying the displacement angles on each end. Figure 6.4 shows the bending test apparatus. The assembly is the same on each end with a motor that drives a 30:1 worm gear to rotate the line of action by 90°. Each end mechanism is mounted on ball bearing rollers to allow

the ends to move relative to each other as the boom length shortens due to the curvature of the boom under bending loads. A torque sensor is mounted underneath each boom end, on top of the linear gear, to measure the bending moment, which allows for claculation of the bending stiffness, according to Equation (6.6). The angles of each end were recorded by cameras looking down onto the end fixtures.

$$EI = (\frac{dM}{d\theta})L \tag{6.6}$$

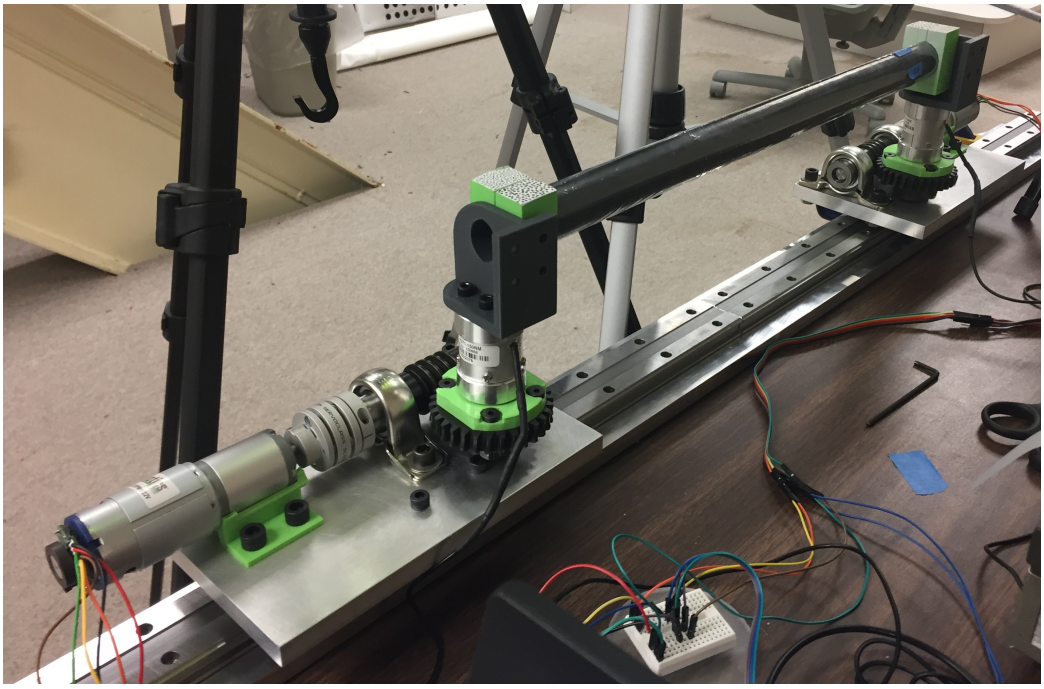

Figure 6.4: Bending test setup with a 45 mm boom mounted for in-plane bending.

Each boom was tested in four directions, +x, -x, +y, -y, according to the coordinate system in Figure 6.1. In-plane bending is the $\pm$x direction because one tape spring is bending equal sense and the other is bending opposite sense. Out-of-plane bending is in the $\pm$y direction because both tape springs are bending along the edges. The boom is mounted for an in-plane test in Figure 6.4, while Figure 6.5 shows a boom mounted for out-of-plane testing. The 3D printed mounts that connect the booms to the torque sensors were designed to allow the boom to be reoriented for testing a new direction without removing the clamps.

Each boom was rotated until it buckled, then the operator stopped the test and the boom was unloaded back to its starting position. Four booms of each size were tested, but since bending testing is destructive, no boom was tested for both coupled and uncoupled. A boom sample was given a state, then it was tested three times in each of the four directions, but only the result from the first test of each direction was used in the analysis. The 20 mm boom samples had an unsupported length of about 48 mm, and the 45 mm boom samples had a unsupported length ranging from 44 - 54 mm.

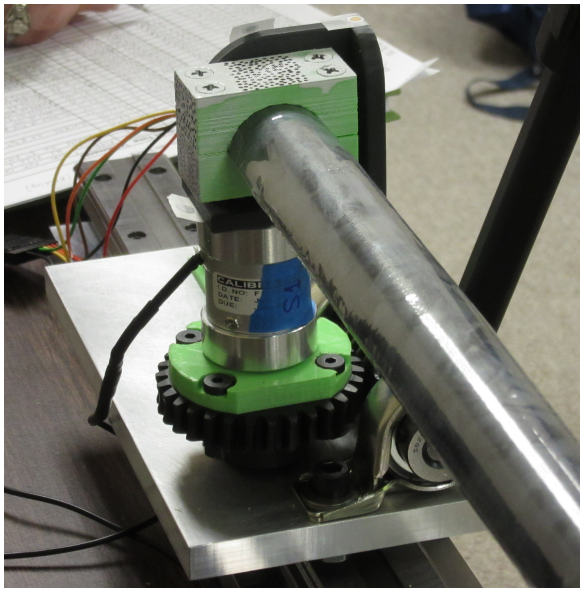

Figure 6.5: One end of a 45 mm boom mounted for out-of-plane bending.

6.4 Results

The testing was conducted during one week in August 2017. The unsupported length of each boom was recorded. The data from the test was compiled into three spreadsheets: encoder time and angle, sensor 1 time and torque, and sensor 2 time and torque. The sensor spreadsheets also recorded the system time from the clock of the computer running the tests. In order to sync the data from the three spreadsheets, the computer clock time was recorded when the test was started. The notes taken during testing can be found in Appendix A.

6.4.1 Photogrammetric Analysis of Angles

There are two ways to determine the angle vs. time: the first is by recording the angle that was commanded by the motor encoder, and the second is to measure it during testing. In this study, both were used. The latter was accomplished by taking video perpendicular to the rotation. Figures 6.6 and 6.7 show the view of the camera for each type of test. The angle was determined using an open source video analysis and modeling tool called Tracker that was developed as part of the Open Source Physics project [123]. It has the ability to track the location of points throughout a video, then measure the angle between three points over time. Figures 6.6 and 6.7 show the three points selected for the tests. The points are tracked by matching a selected template of pixels to those in a small search area of each frame of the video.

For the torsion tests, the angle was determined by tracking two stationary points on the end of the motor and one point on the flag. It was easy to find a point that could be tracked by the software because of the speckle pattern on the end of the flag.

For the bending tests, the three points were: one stationary point on the sled, one point at the axis of rotation at the end of the boom that is also stationary, and one point along the edge of the fixure that rotates with the boom. It was more difficult to find trackable points because these locations are on monochromatic parts. This was solved by taping colored dots with white borders in the desired locations. The cameras were positioned to ensure that all three tracker dots remained in the frame for the entire test.

The angle versus time data was offset so both the time and angle started at zero, then compared to the encoder data. There was a significant difference between what was commanded by the encoder and the angle actually imparted to the booms. This was especially apparent with the bending tests, indicating that there was too much play between the gear teeth. The data measured by Tracker was used in the analyses.

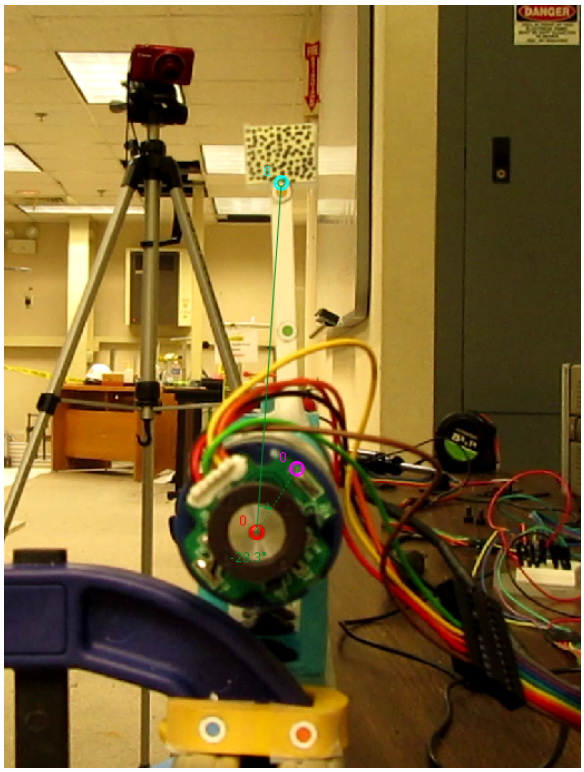

Figure 6.6: End view of torsion test with angle marked in Tracker.

6.4.2 Torsion Data Analysis

In order to analyze the data, first the information gathered from the tests was imported into Matlab. An input file was created with each line providing information about a different test so all of the tests can be analyzed at the same time. The values for the torsion tests are listed in Table 6.4. The next step was to determine the time when the loading of the boom finished. There was a five second pause at 100° rotation, so loading was complete when the difference between two consecutive angle values was less than -0.25. Then, the sensor data was synced with the start of the test by finding when the difference between the test start time and the sensor system time is less than 0.85 seconds.

In finding the slope of the torque versus twist curve to satisfy Equation (6.5), the twist of the boom is calculated according to Equation (6.7) to normalize the results according to boom length. The torque is the average value of the two sensors. One example of the resulting plot is shown in Figure 6.8. The value of tw_{break} mentioned in Table 6.4 is where

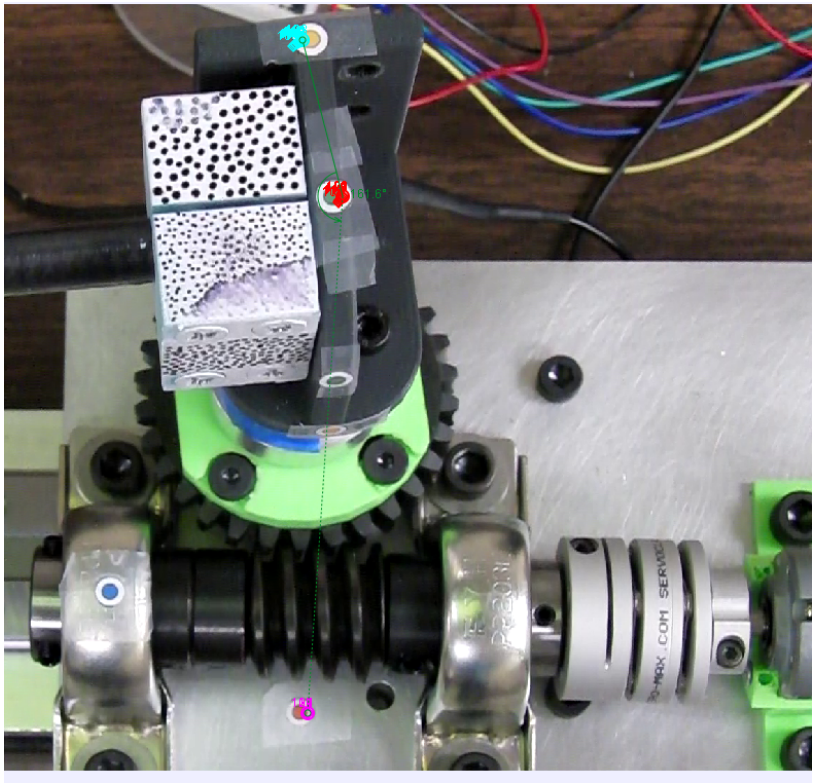

Figure 6.7: Top down view of end 1 during bending test with angle marked in Tracker.

Table 6.4: Information for each test in the torsion input file

Column Number	Data
1	Boom test name: i.e. Boom_45_1a_IP_T1
2	Unsupported length in mm
3	Start time converted into seconds from midnight: i.e. 2:01:10 PM = 50470
4	Filename and pathway for sensor 1 data
5	Filename and pathway for sensor 2 data
6	Filename and pathway for encoder data
7	tw_{break} - twist angle at which to separate the two trendlines
8	Direction of rotation (CCW, CW)
9	Sort - Categorized by boom size, and state
10	Trim - used to clip excess data at end

the two trendlines are split to capture the two phase behavior of the loading curve. The value of this parameter was chosen for each test to enable the trendlines to best match the slope of the data. Only tests where the first trendline is at least 15% of the test are used in

the summary values described later in this section.

$$Twist(t) = \frac{1}{L}\theta(t) \tag{6.7}$$

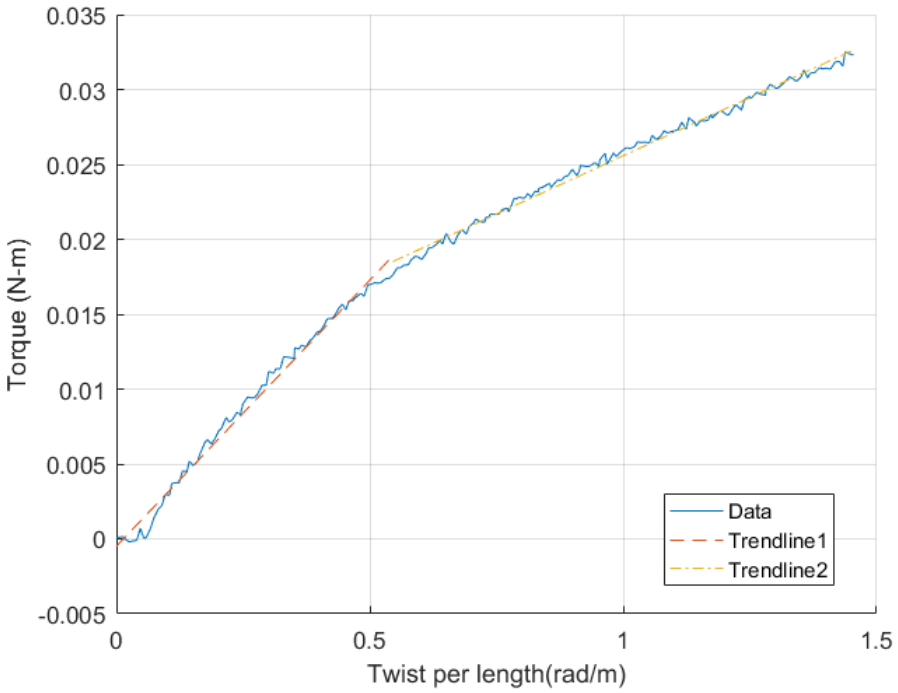

Figure 6.8: Torque vs. Twist plot for 20 mm Boom 3, partially coupled clockwise Test 14.

6.4.3 Bending Data Analysis

The process for analyzing the bending test data is similar to the torsion test. The parameters provided in the input file are listed in Table 6.5. In contrast to the torsion test, when the bending test was canceled by the operator, the arduino code printed a message on the output screen. This means that there is a NaN value at the time of cancellation when the encoder data is read by Matlab. The time of unloading is the time of the NaN value. To sync the sensors with the encoder, the process is the same, but the program looks for when the difference between the saved system time and the provided test start time is < -0.1 for the bending analysis. There was no need to take into account the worm gear when the angle

was determined from the video, but the encoder angle must be divided by 30 before it can be used.

Table 6.5: Information for each test in the bending input file

Column Number	Data
1	Boom test name: i.e. Boom_45_1a_IP_T1
2	Unsupported length in mm
3	Start time converted into seconds from midnight: i.e. 2:01:10 PM = 50470
4	Filename and pathway for sensor 1 data
5	Filename and pathway for sensor 2 data
6	Filename and pathway for angle data
7	t_{break} - time to break the data to limit the length of the trendline
8	Sort - Categorized by bending direction (IP, OP), boom size, and state
9	Direction - categorized by bending direction only (+x, -x, +y, -y)

The results are determined from the Torque vs. Curvature plot, one of which is shown in Figure 6.9. The curvature is the sum of the angles of the two ends divided by the length to normalize the vaules. The torque is half of the difference between the torque measured at each end. The value t_{break} from Table 6.5 is the time where the loading slope finished, and was determined by where the trendline fit the data the best. The time of unloading is after the boom buckled, and it can be seen that the linear behavior during loading changes once the boom buckles.

6.4.4 Torque Sensor Calibration

The torque sensor software allowed different units to be selected, but only linear units were available, so the data was collected in Newtons. The company was contacted about this discrepancy, and they suggested that the sensor was calibrated incorrectly. They recommended the sensors be tested to check if the units were input incorrectly or if the value was also incorrect. The suggested test was suspending a 1 kg mass at the end of a 10 cm lever arm and if the sensor read 0.98 N, the units of the measurements could be changed without modification. Figure 6.10 shows the implementation of this idea, and the sensor read a torque of 0.78 N. This showed that the sensors are measuring torque, but not accurately.

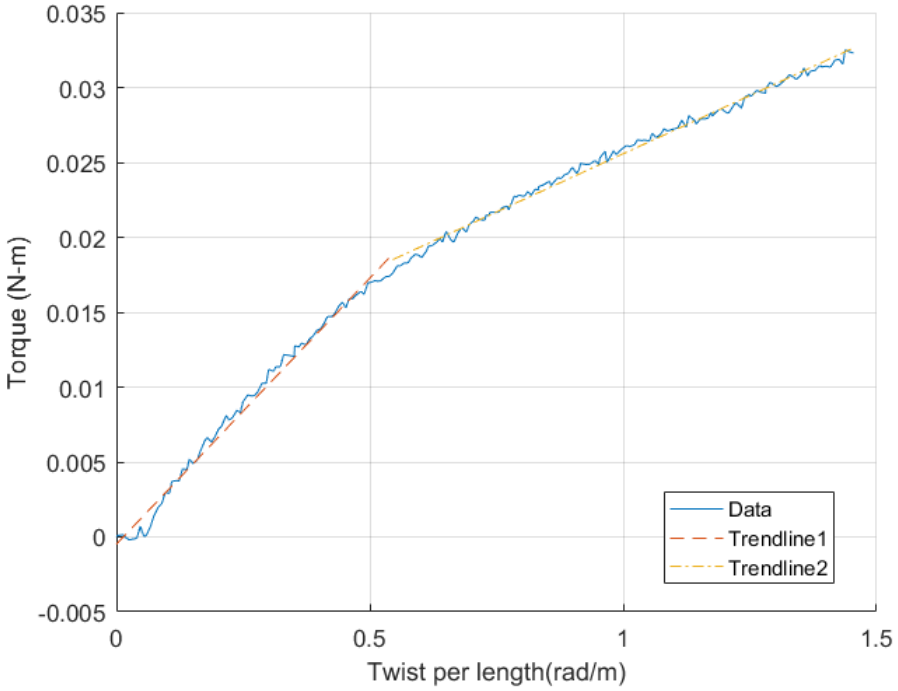

Figure 6.9: Torque vs. Curvature plot for 45 mm Boom 3b, decoupled out of plane bending test 14.

The slightly downward angle of the lever arm is not large enough to account for the large deviation in torque.

The next step was to redesign the test fixture to allow a torque screwdriver to apply a known value, and measure the sensor reading, as shown in Figure 6.11. The torque values in the SHEARLESS testing ranged from 0.002 N-m to 3.5 N-m, so three torque screwdrivers were used to test the sensor at a values ranging 0.3 to 6 N-m. The first two screwdrivers allowed a step size of 0.3 N-m, and the third had a step size of 0.5 N-m. The results were plotted with the screwdriver setting on the x-axis and the sensor reading on the y-axis as shown in Figure 6.12. The slope of the trend line was determined to be the sensor correction value, and all of the readings taken by that sensor were multiplied by this value during postprocessing. The correction values are shown in Table 6.6 and the full test data is in Appendix B. Sensor 1 was on the motor side during the torsion test, and the left hand side of Figure 6.4 for the bending tests. The sensors were labeled both physically and

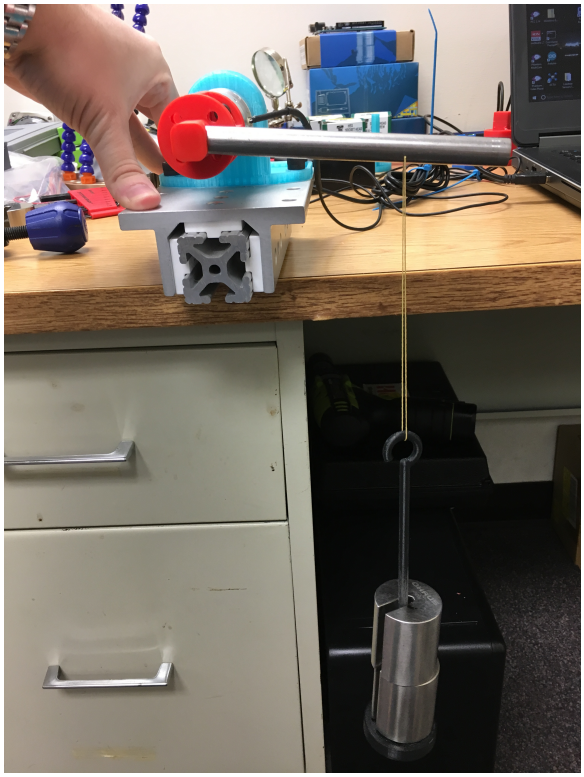

Figure 6.10: The implementation of the recommended torque sensor validation test.

within the software to ensure they were not switched.

The final concern about the torque sensors is the magnitude of the torque values measured. The sensors have a maximum load of 150 N-m, so all of the tests were in the smallest 3% of its range. This means that the torque values measured, especially for the torsion test, were at a similar order of magnitude to the noise of the sensor.

Table 6.6: The torque correction values for each torque sensor.

Sensor Name	Correction Value
Torque Sensor 1	1.3029
Torque Sensor 2	1.1720

6.4.5 Torsion Test Results

The average stiffness for each boom state and size for the torsion test are summarized in Table 6.7. Neither boom is particularly stiff in torsion, and all the values lie within the

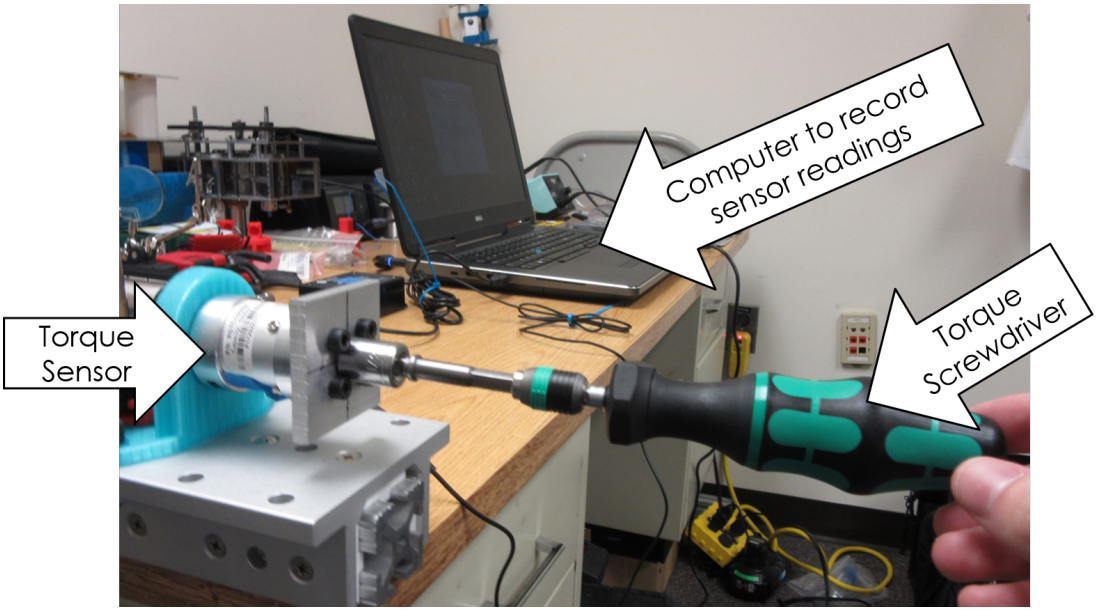

Figure 6.11: The test setup to characterize the offset in the torque sensor.

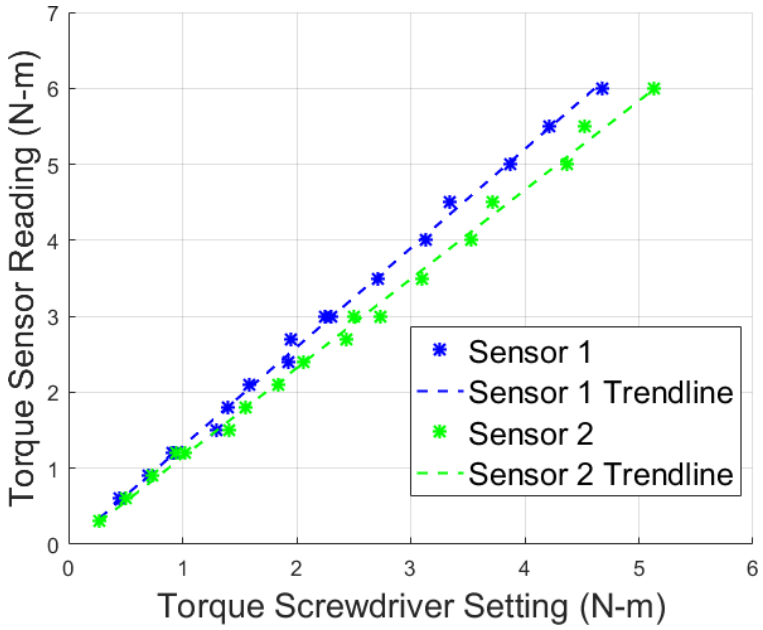

Figure 6.12: The results of the torque sensor characterization test series.

region bounded by the stiffnesses of theoretical closed and open cross-sections discussed earlier. These values show that the sleeve does impart a small but noticeable torsional stiffness since the stiffness is closer to the open cross-section, but not quite that small. It is also important to note that for both boom sizes, the coupled state had the highest stiffness, followed by the partially coupled state, then finally the uncoupled state, as expected.

Table 6.7: Average torsional stiffness for all boom sizes and states with 1σ error.

Boom size and state	Stiffness (N-m)	$\pm 1\sigma$
45 mm coupled	0.3057	0.0309
45 mm partially coupled	0.2284	0.0203
45 mm uncoupled	0.2007	0.0255
20 mm coupled	0.0449	0.0318
20 mm partially coupled	0.0340	0.0108
20 mm uncoupled	0.0247	0.0041

Figure 6.13 shows results of each of the accepted tests with the 45 mm boom results on the left and the 20 mm boom results on the right. The vertical axes are the same for booms of the same size to more easily compare the stiffnesses visually. Some tests were not included because there was not an end video to do the tracker analysis, and some because the first trendline was not 15% of the total test. There is not a significant difference between clockwise and counter-clockwise tests. For the 20 mm booms, it looks like boom 3 was stiffer than boom 1 in general, probably due to manufacturing or assembly.

6.4.6 Bending Test Results

The average stiffness for each boom size, state, and direction are summarized in Table 6.8. The two cases with N/A values for the 1σ are because there was only one valid test in that category. It can be seen that a coupled boom is stiffer than an uncoupled boom, and the booms are stiffer in the out-of-plane direction. This is consistent with the theoretical values because $E_x I_{xx}$ is the out-of-plane direction and is the stiffer value. For the bending testing, each boom was tested until it buckled, which is a failure mode. This meant that repeated tests in the same direction were less stiff due to the weak point in the tape springs, and only the first test in each direction was considered accurate. Another problem was that sometimes the tape springs fractured when they failed, which invalidates all the subsequent tests. There were not enough samples manufactured to use a new sample for each test.

Figures 6.14 and 6.15 shows the bending stiffness values for each of the accepted tests.

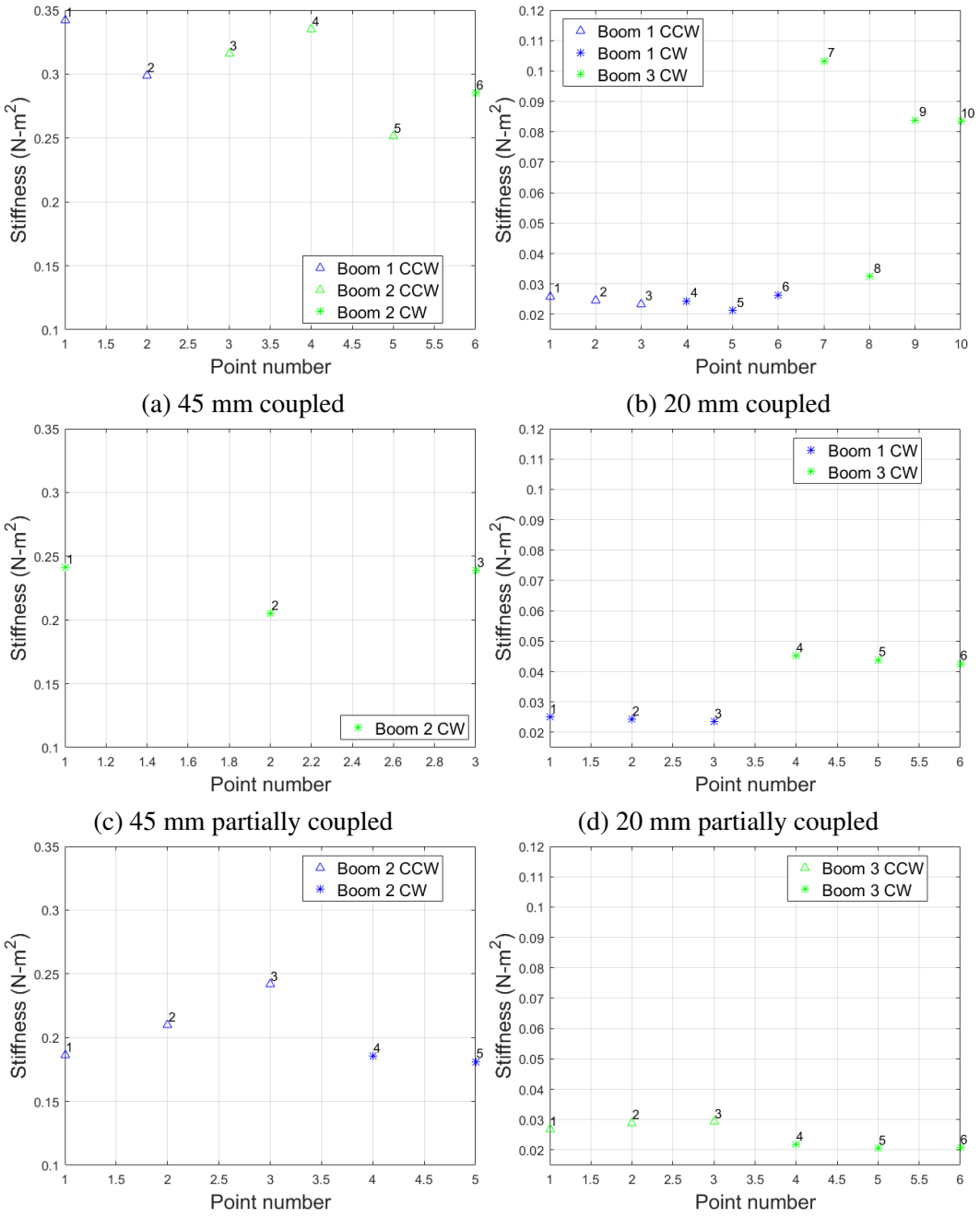

(a) 45 mm coupled

(b) 20 mm coupled

(c) 45 mm partially coupled

(d) 20 mm partially coupled

(e) 45 mm uncoupled

(f) 20 mm uncoupled

Figure 6.13: Torsional stiffness values for all of the accepted tests for each boom size and state.

The worm gear and the linear gear had too much play between the connecting teeth, so when the 45 mm boom was tested in the out-of-plane direction, one of the linear gears started to disengage from the worm gear by moving upward because the boom was too

Table 6.8: Average bending stiffness for all states, sizes, and directions with 1σ error.

Boom size and state	In-plane		Out of plane	
	Stiffness (N-m)	$\pm 1\sigma$	Stiffness (N-m)	$\pm 1\sigma$
45 mm coupled	5.3634	0.5559	12.0440	N/A
45 mm uncoupled	2.9577	0.5551	6.6962	1.8444
20 mm coupled	2.1915	0.1704	2.3726	0.9035
20 mm uncoupled	2.1502	0.0622	2.5592	N/A

stiff. This was overcome by preventing vertical movement of the linear gear during testing. This also became apparent when the end videos were analyzed with the Tracker program because not only was there a large difference between the angle the encoder commanded and the angle actually seen by the boom, there was a significant difference in angle seen by the two ends. In order for this to be a valid 4-point bending test, the two ends need to rotate at similar rates. For many of the tests, one end rotated faster than the other, most likely resulting from the loose fit of the gears. Most of the tests with end differences higher than 35% were rejected as not being accurate tests. Most of the tests with the 20 mm boom buckled closer to one end fitting instead of in the middle. This is most likely resulting from the unequal rotation and the boom samples being too long.

6.5 Conclusion

The torsion test setup functioned as desired and produced consistent results. The bending test setup needs to be redesigned with tighter fitting gears, including vertical constraints on the movement of the linear gear to ensure that the angles imparted on the ends stay within about 10% of each other throughout the test. Since the torques measured were at the extreme low end of the measurement range of the torque sensors, the confidence in the derived stiffnesses is very low.

Future testing needs to be conducted with more sensitive torque sensors, and more test bending test samples. The data collection and analysis methods described here can be utilized for that future testing.

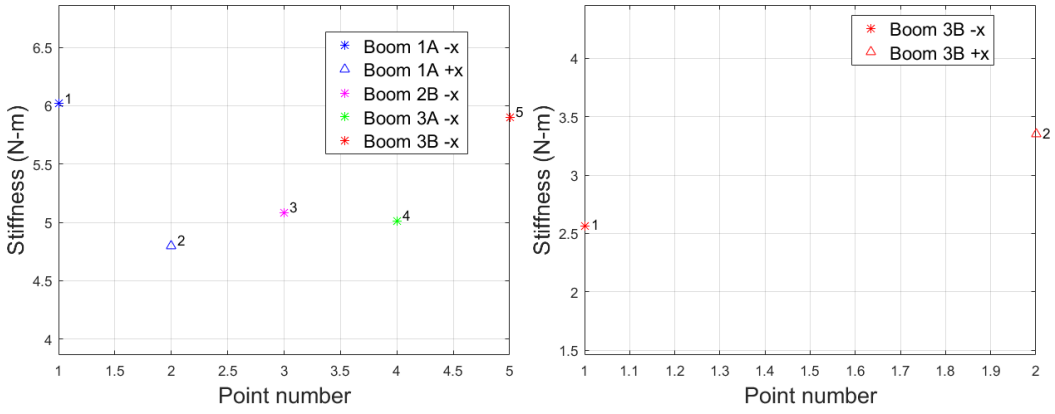

(a) In-plane coupled

(b) In-plane uncoupled

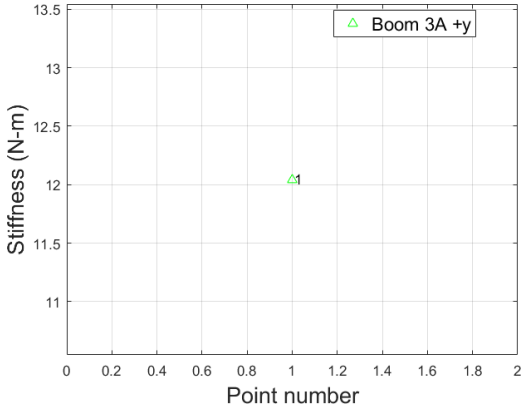

(c) Out-of-plane coupled

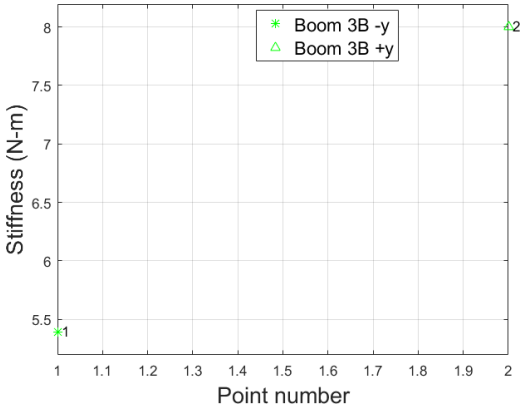

(d) Out-of-plane uncoupled

Figure 6.14: Bending stiffness values for all of the accepted tests for all states and directions for 45 mm booms.

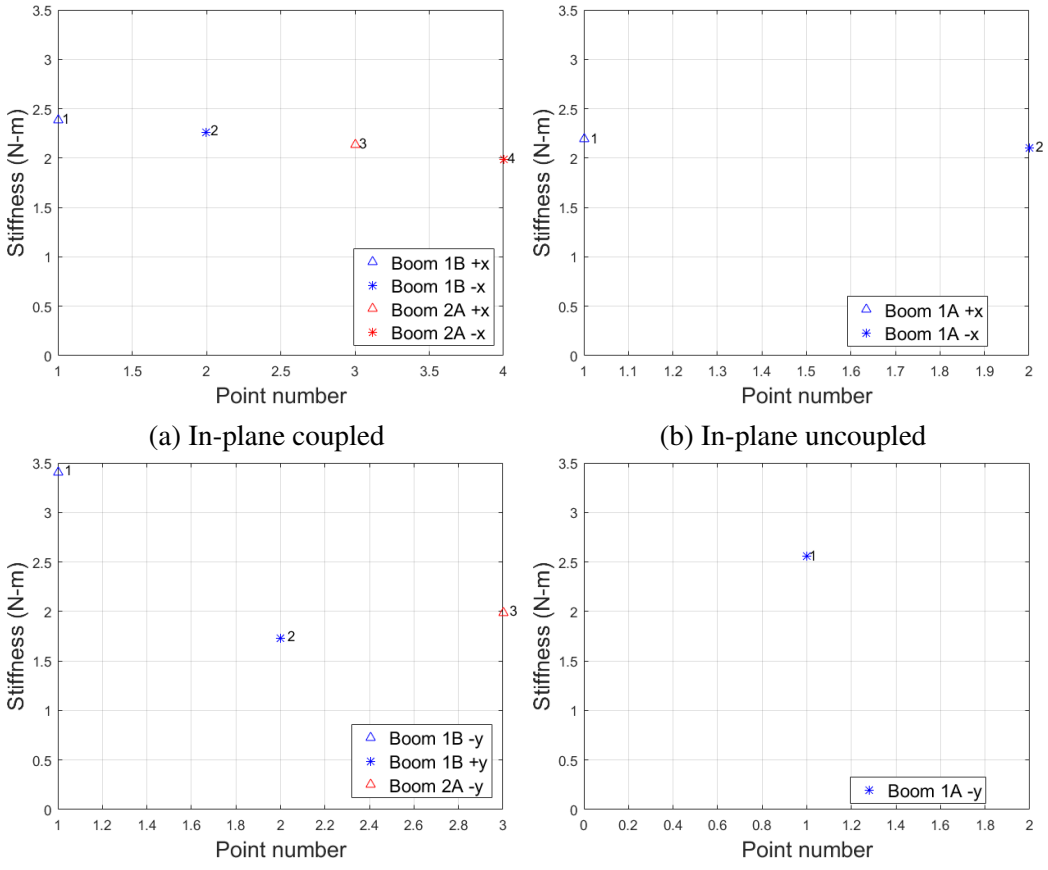

(a) In-plane coupled

(b) In-plane uncoupled

(c) Out-of-plane coupled

(d) Out-of-plane uncoupled

Figure 6.15: Bending stiffness values for all of the accepted tests for all states and directions for 20 mm booms.

CHAPTER 7
CONCLUSIONS

The goal of this work is to create a system that will passively deorbit a satellite from Low Earth Orbit to reduce the probability of collisions. This chapter summarizes the three main contributions to to the current state of the art and where they are addressed in this thesis. Then, it discusses the recommendations for future work to continue the design and development of the $[PS]^2$ system.

7.1 Contributions to the State of the Art

The three contributions this thesis makes to the state of the art are as follows:

Contribution 1 Design of an aerodynamically stable, passive, deployable drag device for small satellite deorbit

Contribution 2 Development and laboratory testing of a 1:10 scale prototype of the drag device to demonstrate functionality

Contribution 3 Characterization of SHEARLESS booms

Contribution 1 is addressed first in Chapter 2 with a trade study to determine the device configuration based on performance, reliability, collision avoidance, and the impact to the host spacecraft. It concludes that an aerodynamically stable drag sail is the favored design if the primary mission does not require a propulsion system. Next requirements were developed , which are addressed in Chapter 3. This chapter first developed the overall driving requirements for a scalable system to create a framework for further development. This included defining the required size of the sail for a range of satellite masses and orbit altitudes, defining the standard interface between the sail and satellite, defining ways

to initiate the deployment, and requiring passive aerodynamic stability. The rest of Chapter 3 discusses the analyses used to determine the specific requirements for the CubeSat and ESPA-class systems. Specifically, the structural requirements for the booms and the material and thickness requirements for the membrane to ensure the system survives the Low Earth Orbit environment for 25 years.

The final aspect of Contribution 1 expands upon the final driving requirement of passive aerodynamic stability with the aerostability analysis of Chapter 4. This chapter describes a simulation of the satellite-sail behavior to determine the favored apex half-angle to balance stability and drag generation. The simulation integrates equations of motion for both the attitude dynamics and orbital mechanics, and includes the three disturbance torques encountered in LEO: aerodynamic, solar radiation pressure, and gravity gradient. The torques are simplified to analytical equations for this model, but aerodynamic damping and self-shadowing are included. The stability of the system is first analyzed using a simplified model that assumes constant application of the disturbance torques, known as wind tunnel mode, followed by analysis of the stability with the full orbital motion. For each phase of the analysis, the simulation is run without the solar radiation pressure torques to enable a comparison between the contributions of the aerodynamics and SRP. It is shown that aerodynamic drag torques dominate starting at approximately an altitude of 500 km, and the apex half-angle was chosen to be 70°.

Contribution 2 is addressed in Chapter 5 with the conceptual design of an ESPA-class drag sail and the design and prototype testing of a CubeSat-class sail for the Aerodynamic Deorbit Experiment that is being built by Purdue University. This chapter uses the trade study results and design decisions from contribution 1 and demonstrates that the stowed volume and mass for a given boom length from Chapter 3 are achievable. The main design choices are stowing each boom on separate deployers to create the pyramid shape, the boom deployer design, and the ripstop and folding patterns for the sail membrane. The size difference between the two classes investigated requires a few design changes that are

also discussed in this chapter. The prototype testing of the CubeSat-class sail furthered the design for the Aerodynamic Deorbit Experiment technology demonstration mission.

Contribution 3 is addressed in Chapter 6 with the characterization testing of the SHEARLESS booms. The procedure for testing the booms and analyzing the data is described. The results provide approximate mechanical properties, but there are a number of ways that the test fixture should be redesigned for future testing to provide more reliable results. These properties verify that the booms are strong enough to meet the requirements discussed in Chapter 3.

7.2 Future Work

A number of simplifying assumptions were made in order to initially understand the different aspects of the design. Overall, the recommendations for future work are to increase the fidelity of the analyses.

The first recommendation is to include the probability of collision in the sizing analysis in Chapter 3. This will take into account the object density in the different orbital bands that the satellite will pass through while deorbiting. This could change the recommended sail size in order to decrease the probability of creating more debris.

A second suggestion is to model the satellite as tumbling when estimating the deployment loads for the boom structural requirements in Chapter 3. The included analysis assumed the deployment was quasi-static, where the deployment is slow and the satellite is stationary. Especially for the CubeSat-class sail, this is not accurate. A higher fidelity model that includes forces from movement of the satellite and faster deploying booms should be conducted. It is worth modeling the deployment of the system in a simulation to better understand deployment behavior.

The third and fourth recommendations involve the stability analysis in Chapter 4. The system should be modeled as a flexible body instead of a rigid body, and Direct Simulation Monte Carlo should be used to model the areodynamics in the simulation to increase the

fidelity.

A fifth suggestion is to continue the hardware development for both the CubeSat-class and ESPA-class designs from Chapter 5. The next step is to build the engineering design unit, then the flight unit for the Aerodynamic Deorbit Experiment mission. After that technology demonstration mission, detailed design and prototype development of the ESPA-class system should be undertaken.

The sixth recommendation is to improve the SHEARLESS characterization test setup according to the recommendations at the end of Chapter 6. These include using torque sensors that match the order of magnitude of the torques being measured, redesigning the bending set up so the gears have a tighter fit, and finally, having many more booms to available to test in bending. Once the test results have been collected, creating a finite element model of these booms using both shell and beam elements will help the booms to be used in future designs.

Appendices

APPENDIX A

SHEARLESS TESTING NOTES

All tests 2-3 times

In plane bending is x-direction

Out of plane bending is y direction

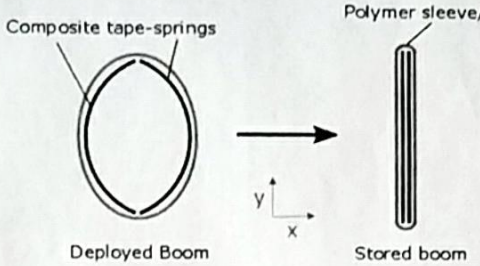

counterclockwise → positive

SHEARLESS Booms

1. Torsion — 20 mm, sample 3 → 39 7/8"
   a. 45 mm, 4 ft long, sample 1 → Length = 46.5"
      i. Clockwise — unsupported Length = 44.5"
      ii. Counterclockwise
   b. 45 mm, 4 ft long, sample 2 → unsupported Length = 44.5"
      i. Clockwise
      ii. Counterclockwise
   c. 20 mm, 1 m long, sample 1 → unsupported Length = 39 7/8"
      i. Clockwise
      ii. Counter Clockwise
   d. 20 mm, 1 m long, sample 2 → unsupported Length = 40"
      i. Clockwise
      ii. Counter Clockwise

coupled / decoupled / partially coupled

2. Bending
   a. 45 mm, 2 ft long, sample 1a
      i. In-plane, right
      ii. In-plane, left
      iii. Out of plane, top
      iv. Out of plane, bottom
   b. 45 mm, 2 ft long, sample 1b
      i. In-plane, right
      ii. In-plane, left
      iii. Out of plane, top
      iv. Out of plane, bottom
   c. 45 mm, 2 ft long, sample 2a
      i. In-plane, right
      ii. In-plane, left
      iii. Out of plane, top

coupled / decoupled

Bending Booms: (unsupported length)

- 45mm 2A → 17 7/8"
- ★45mm 2B → 21 1/8"
- 20mm 2A → 18 7/8"
- 20mm 2B → 19 1/16"
- ★★45mm 1A → 21 1/4"
- 20mm 1A → 18 13/16"
- 20mm 1B → 19"
- 45mm 3A → 21.5"
- 45mm 3AS → 19 15/16"
- 45mm 3B → 21 1/4"

tape springs are twisted
3A was shortened → to cut off damage at end from worm gear 2 not spinning

★ 45mm 2B is made from two halfs of one of the shells from Boom 1

★★ 45mm 1A is made from the other shell from 45mm Boom 1

SHEARLESS Characterization Testing → sheet 1

unsupported length: 44.5"
96.133 encoder points/degree

Date	Boom Size/#	Direction	Type	Test #	Start Time	
8/3/2017	45mm, Boom 1	CCW	torsion	1	12:04:05 PM	135°
8/3/2017	45mm, Boom 1	CCW	torsion	2	12:12:30 PM	added set screw
8/3/2017	45mm, Boom 1	CCW	torsion	3	4:33:40 pm	
8/3/2017	45mm, Boom 1	CCW	torsion	4	4:44:00 pm	100° speed = 9
8/3/2017	45mm, Boom 1	CCW	torsion	5	4:48:10 pm	
8/3/2017	45mm, Boom 1	CW	torsion	6	5:00:35 pm	speed = 10
8/3/2017	45mm, Boom 1	CW	torsion	7	5:05:30 pm	exceeded angle
8/3/2017	45mm, Boom 1	CW	torsion	8	5:09:20 pm	
8/3/2017	45mm, Boom 1	CW	torsion	9	5:12:15 pm	coupled
8/3/2017	45mm, Boom 1	CCW	torsion	10	5:30:10 pm	Decoupled
8/3/2017	45mm, Boom 1	CCW	torsion	11	5:35:20 pm	
8/3/2017	45mm, Boom 1	CCW	torsion	12	5:38:20 pm	
8/3/2017	45mm, Boom 1	CW	torsion	13	5:42:30 pm	
8/3/2017	45mm, Boom 1	CW	torsion	14	5:45:40 pm	
8/3/2017	45mm, Boom 1	CW	torsion	15	5:48:40 pm	
8/3/2017	45mm, Boom 1	CW	torsion	16	5:59:20 pm	Partially coupled driven side
8/3/2017	45mm, Boom 1	CW	torsion	17	6:02:20 pm	
8/3/2017	45mm, Boom 1	CW	torsion	18	6:05:10 pm	
8/4/2017	45mm, Boom 2	CCW	torsion	1	9:09:05 am	speed = 10 coupled
8/4/2017	45mm, Boom 2	CCW	torsion	2	9:12:25 am	
8/4/2017	45mm, Boom 2	CCW	torsion	3	9:15:05 am	
8/4/2017	45mm, Boom 2	CW	torsion	4	9:18:10 am	
8/4/2017	45mm, Boom 2	CW	torsion	5	9:21:00 am	
8/4/2017	45mm, Boom 2	CW	torsion	6	9:23:25 am	
8/4/2017	45mm, Boom 2	CCW	torsion	7	4:52:53 pm	Decoupled
8/4/2017	45mm, Boom 2	CCW	torsion	8	4:58:45 pm	
8/4/2017	45mm, Boom 2	CCW	torsion	9	5:02:20 pm	
8/4/2017	45mm, Boom 2	CW	torsion	10	5:09:00 pm	
8/4/2017	45mm, Boom 2	CW	torsion	11	5:12:40 pm	
8/4/2017	45mm, Boom 2	CW	torsion	12	5:16:35 pm	
8/4/2017	45mm, Boom 2	CW	torsion	13	5:29:55 pm	Partially coupled fixed side
8/4/2017	45mm, Boom 2	CW	torsion	14	5:34:25 pm	
8/4/2017	45mm, Boom 2	CW	torsion	15	5:37:50 pm	
8/7/2017	20mm, Boom 1	CCW	torsion	1	12:13:50 pm	Coupled → motor turned slightly
8/7/2017	20mm, Boom 1	CCW	torsion	2	12:18:30 pm	
8/7/2017	20mm, Boom 1	CCW	torsion	3	12:22:50 pm	
8/7/2017	20mm, Boom 1	CCW	torsion	4	12:25:50 pm	No valuable video data
8/7/2017	20mm, Boom 1	CW	torsion	5	12:31:35 pm	Lost Arduino data (encoder)
8/7/2017	20mm, Boom 1	CW	torsion	6	12:36:20 pm	
8/7/2017	20mm, Boom 1	CW	torsion	7	12:38:50 pm	
8/7/2017	20mm, Boom 1	CW	torsion	8	12:49:00 pm	
8/7/2017	20mm, Boom 1	CW	torsion	9	12:55:40 pm	Partially coupled
8/7/2017	20mm, Boom 1	CW	torsion	10	12:59:00 pm	
8/7/2017	20mm, Boom 1	CW	torsion	11	1:02:00 pm	

20mm Boom 1 unsupported length = 39.875"

SHEARLESS Characterization Testing

	Date	Boom Size/#	Direction	Type	Test #	Start Time	
Decoupled	8/7/2017	20 mm, Boom 1	CW	torsion	12	2:06:20 pm	
	8/7/2017	20 mm, Boom 1	CW	torsion	13	2:09:20 pm	
	8/7/2017	20 mm, Boom 1	CW	torsion	14	2:12:55 pm	
	8/7/2017	20 mm, Boom 1	CCW	torsion	15	2:17:30 pm	
	8/7/2017	20 mm, Boom 1	CCW	torsion	16	2:21:00 pm	
	8/7/2017	20 mm, Boom 1	CCW	torsion	17	2:23:55 pm	
Coupled	8/7/2017	20 mm, Boom 2	CCW	torsion	1	2:33:05 pm	
	8/7/2017	20 mm, Boom 2	CCW	torsion	2	2:37:40 pm	
	8/7/2017	20 mm, Boom 2	CCW	torsion	3	2:40:50 pm	
	8/7/2017	20 mm, Boom 2	CW	torsion	4	2:45:20 pm	
	8/7/2017	20 mm, Boom 2	CW	torsion	5	2:48:15 pm	
	8/7/2017	20 mm, Boom 2	CW	torsion	6	2:51:00 pm	
partially Coupled	8/7/2017	20 mm, Boom 2	CW	torsion	7	4:37:20 pm	
	8/7/2017	20 mm, Boom 2	CW	torsion	8	4:41:20 pm	
	8/7/2017	20 mm, Boom 2	CW	torsion	9	4:44:10 pm	
Decoupled	8/7/2017	20 mm, Boom 2	CW	torsion	10	4:50:15 pm	
	8/7/2017	20 mm, Boom 2	CW	torsion	11	4:53:20 pm	
	8/7/2017	20 mm, Boom 2	CW	torsion	12	4:56:15 pm	
	8/7/2017	20 mm, Boom 2	CW	torsion	13	4:59:20 pm	# Accidentally uploaded CCW code
	8/7/2017	20 mm, Boom 2	CCW	torsion	14	5:03:05 pm	
	8/7/2017	20 mm, Boom 2	CCW	torsion	15	5:06:00 pm	
	8/7/2017	20 mm, Boom 2	CCW	torsion	16	5:08:50 pm	

SHEARLESS Characterization Testing → torsion (second try)

Date	Boom Size/#	Direction	State	Type	#	Start Time	Comments
8/11/2017	20 mm, 3	CCW	coupled	torsion	1	2:43:10	CASIO camera out of focus. Abandoned use from here on out.
8/11/2017	20 mm, 3	CCW	coupled	torsion	2	2:47:15	
8/11/2017	20 mm, 3	CCW	coupled	torsion	3	2:50:05	Forgot to zero encoders
8/11/2017	20 mm, 3	CW	coupled	torsion	4	2:53:40	
8/11/2017	20 mm, 3	CW	coupled	torsion	5	2:58:30	
8/11/2017	20 mm, 3	CW	coupled	torsion	6	3:02:10	
8/11/2017	20 mm, 3	CCW	Decoupled	torsion	7	3:08:40	
8/11/2017	20 mm, 3	CCW	Decoupled	torsion	8	3:11:55	
8/11/2017	20 mm, 3	CCW	Decoupled	torsion	9	3:14:30	
8/11/2017	20 mm, 3	CW	Decoupled	torsion	10	3:17:20	
8/11/2017	20 mm, 3	CW	Decoupled	torsion	11	3:20:10	
8/11/2017	20 mm, 3	CW	Decoupled	torsion	12	3:22:45	
8/11/2017	20 mm, 3	CW	Partially coupled	torsion	13	3:39:55	
8/11/2017	20 mm, 3	CW	Partially coupled	torsion	14	3:41:50	
8/11/2017	20 mm, 3	CW	Partially coupled	torsion	15	3:44:50	

SHEARLESS Characterization Testing → Sheet 2 (Bending)

Date	Boom Size/#	Direction	State	Type	Test #	Start Time	Comments
8/8/2017	45mm, 2A	−X (IP)	Uncoupled	Bending	1	1:22:30	Motor 1 was not rotating
8/8/2017	45mm, 2A	−X (IP)	Uncoupled	Bending	2	1:27:50	Same as test 1
8/8/2017	45mm, 2A	−X (IP)	Uncoupled	Bending	3	1:34:15	Buckled at 5" from end 1. Failure of inner and outer shells. cracks on top edges
8/8/2017	45mm, 2A	−X (IP)	Uncoupled	Bending	4	1:51:55	
8/8/2017	45mm, 2A	−X (IP)	Uncoupled	Bending	5	1:57:10	
8/8/2017	45mm, 2A	+X (IP)	Uncoupled	Bending	6	2:04:50	Buckled at 8 1/2" from end 1. cracked on inner shell top edge
8/8/2017	45mm, 2A	+X (IP)	Uncoupled	Bending	7	2:11:15	
8/8/2017	45mm, 2A	+X (IP)	Uncoupled	Bending	8	2:20:35	
8/9/2017	45mm, 2B	−X (IP)	Coupled	Bending	1	12:31:45	Buckled at 9 1/8" from end 1.
8/9/2017	45mm, 2B	−X (IP)	Coupled	Bending	2	12:37:10	Buckled at 9 1/8" from end 1. ES shell fatigued. Beneath nose IP shell pulled away from ES shell with 2 kinks at buckled wrinkle.
8/9/2017	45mm, 2B	−X (IP)	Coupled	Bending	3	12:40:15	Buckled at 9 1/2" from end 1. Kill switch Didn't work, got too far, no encoder data
8/9/2017	45mm, 1A	−X (IP)	Coupled	Bending	1	2:01:10	Buckled at 6.5" from end 1.
8/9/2017	45mm, 1A	−X (IP)	Coupled	Bending	2	2:09:50	Buckled at Halfway pt
8/9/2017	45mm, 1A	−X (IP)	Coupled	Bending	3	2:11:20	Buckled at Halfway pt. Small crack on top edge of ES shell. Small crack on top edge of ES shell about 4"
8/9/2017	45mm, 1A	+X (IP)	Coupled	Bending	4	2:18:55	Buckled at Halfway, Decoupled on ES shell toward end 2
8/9/2017	45mm, 1A	+X (IP)	Coupled	Bending	5	2:25:40	
8/9/2017	45mm, 1A	+Y (OP)	Coupled	Bending	6	2:38:25	Buckled at root on end 1, Clamp 1 was loose
8/9/2017	45mm, 1A	+Y (OP)	Coupled	Bending	7	2:43:05	Buckled at root on end 1
8/9/2017	45mm, 1A	+Y (OP)	Coupled	Bending	8	3:00:10	Buckled at root on end 1
8/9/2017	45mm, 1A	−Y (OP)	Coupled	Bending	9	3:08:05	Side 2 lifted out of the worm gear
8/9/2017	45mm, 1A	−Y (OP)	Coupled	Bending	10	3:09:10	Side 2 lifted, Boom Buckled at root on end 1
8/9/2017	45mm, 1A	−Y (OP)	Coupled	Bending	11	3:	Aborted
8/9/2017	45mm, 1A	−Y (OP)	Coupled	Bending	12	3:20:05	Buckled at end 1
8/9/2017	45mm, 1A	−Y (OP)	Coupled	Bending	13	3:23:20	Buckled at end 1
8/9/2017	45mm, 1A	+Y (OP)	Uncoupled	Bending	14	3:41:58	Buckled at end 1
8/9/2017	45mm, 1A	+Y (OP)	Uncoupled	Bending	15	3:44:55	Buckled at end 1, End 1 was rotating more than 2
8/9/2017	45mm, 1A	+Y (OP)	Uncoupled	Bending	16	3:49:45	Buckled at end 1
8/9/2017	45mm, 1A	+X (IP)	Uncoupled	Bending	17	4:01:05	Buckled halfway
8/9/2017	45mm, 1A	+X (IP)	Uncoupled	Bending	18	4:10:30	Buckled halfway
8/9/2017	45mm, 1A	+X (IP)	Uncoupled	Bending	19	4:19:10	Buckled halfway

No torque data

SHEARLESS Characterization Testing

Date	Boom Size/#	Direction	State	Type	Test #	Start Time	Comments
8/9/2017	20mm, 2A	+X	Coupled	Bending	1	4:48:35	Buckled 3 3/4" from end 1, damage in bottom of OS shell
8/9/2017	20mm, 2A	+X	Coupled	Bending	2	5:07:25	Buckled same spot
8/9/2017	20mm, 2A	+X	Coupled	Bending	3	5:10:55	Buckled same spot
8/9/2017	20mm, 2A	-X	Coupled	Bending	4	5:19:40	Buckled 6 1/2" from end 2 No fracture yet
8/9/2017	20mm, 2A	-X	Coupled	Bending	5	5:27:40	Buckled same spot
8/9/2017	20mm, 2A	-X	Coupled	Bending	6	5:31:10	Buckled same spot
8/9/2017	20mm, 2A	+Y	Coupled	Bending	7	5:43:05	Top tape is fractured at 7 1/2" from end 1 (+X is up)
8/9/2017	20mm, 2A	+Y	Coupled	Bending	8	5:48:15	Buckled same spot
8/9/2017	20mm, 2A	+Y	Coupled	Bending	9	5:50:55	Buckled same spot
8/9/2017	20mm, 2A	-Y	Coupled	Bending	10	5:55:35	Buckled in 3 spots, Dsame as before → 7" from end 2 in tape
8/9/2017	20mm, 2A	-Y	Coupled	Bending	11	6:02:00	Same
8/9/2017	20mm, 2A	-Y	Coupled	Bending	12	6:05:15	Same
8/10/2017	20mm, 2B	+X	Decoupled	Bending	1	9:34:00	Buckled 4" from end 1
8/10/2017	20mm, 2B	+X	Decoupled	Bending	2	9:39:50	Buckles same spot, Large fracture in center of OS 2 3/4" from end 1 Tiny fracture in upper FS 8" from end 1
8/10/2017	20mm, 2B	-X	Decoupled	Bending	3	9:50:20	Stopped Before actual failure
8/10/2017	20mm, 2B	-X	Decoupled	Bending	4	9:53:05	Buckled 4" from end 2, same spot as before b/c boom was rotated
8/10/2017	20mm, 2B	-X	Decoupled	Bending	5	9:56:25	Buckled same spot
8/10/2017	20mm, 2B	+Y	Decoupled	Bending	6	10:02:20	Fractured center top side @ 9 7/8" from end 1
8/10/2017	20mm, 2B	+Y	Decoupled	Bending	7	10:36:50	Buckled 7 3/4" from end 1
8/10/2017	20mm, 2B	+Y	Decoupled	Bending	8	10:40:30	Same place
8/10/2017	20mm, 2B	-Y	Decoupled	Bending	9	10:48:00	2 failure pts: 1) 2 7/16" from end 1 2) 5/8" from end 2
8/10/2017	20mm, 2B	-Y	Decoupled	Bending	10	10:55:30	Buckled at 2 1/16" from end 1
8/10/2017	20mm, 2B	-Y	Decoupled	Bending	11	10:59:35	Same as above
8/10/2017	20mm, 1B	+X	Coupled	Bending	1	1:07:00	Buckled 4 3/4" from end 1
8/10/2017	20mm, 1B	+X	Coupled	Bending	2	1:09:35	Buckled same spot
8/10/2017	20mm, 1B	+X	Coupled	Bending	3	1:12:25	Same spot
8/10/2017	20mm, 1B	-X	Coupled	Bending	4	1:15:35	Buckled 4 1/2" from end 1
8/10/2017	20mm, 1B	-X	Coupled	Bending	5	1:18:55	Crack 3 1/2" from end 1, edge of OS shell
8/10/2017	20mm, 1B	-Y	Coupled	Bending	6	1:23:40	Buckled 9 3/4" from end 1
8/10/2017	20mm, 1B	-Y	Coupled	Bending	7	1:26:20	3 kinks at the previous fracture pts
8/10/2017	20mm, 1B	-Y	Coupled	Bending	8	1:29:10	Same
8/10/2017	20mm, 1B	+Y	Coupled	Bending	9	1:33:15	Cracked at point near end 1
8/10/2017	20mm, 1B	+Y	Coupled	Bending	10	1:35:55	Same spot

SHEARLESS Characterization Testing

Date	Boom Size/#	Direction	State	Type	Test #	Start Time	Comments
8/10/2017	20mm, 1B	+Y	Coupled	Bending	11	1:38:25	Broken
8/10/2017	20mm, 1A	+X	Decoupled	Bending	1	1:46:20	3" from end 1, very small crack in +Y edge of S1 shell
8/10/2017	20mm, 1A	+X	Decoupled	Bending	2	1:49:20	Same spot, crack expanded slightly
8/10/2017	20mm, 1A	+X	Decoupled	Bending	3	1:51:50	Same spot
8/10/2017	20mm, 1A	−X	Decoupled	Bending	4	3:20:45	2¾" from side 2, same spot b/c boom was spun
8/10/2017	20mm, 1A	−X	Decoupled	Bending	5	3:24:00	Same
8/10/2017	20mm, 1A	−X	Decoupled	Bending	6	3:26:35	Same
8/10/2017	20mm, 1A	+Y	Decoupled	Bending	7	3:30:40	3" from side 2 → same spot
8/10/2017	20mm, 1A	+Y	Decoupled	Bending	8	3:33:30	Same spot, big crack in bottom shell
8/10/2017	20mm, 1A	+Y	Decoupled	Bending	9	3:35:40	Same spot.
8/10/2017	20mm, 1A	−Y	Decoupled	Bending	10	3:38:10	3" from side 1 → boom was spun
8/10/2017	20mm, 1A	−Y	Decoupled	Bending	11	3:40:55	Same
8/10/2017	20mm, 1A	−Y	Decoupled	Bending	12	3:43:06	Same
8/10/2017	45mm, 3A	−X	Coupled	Bending	1	4:42:10	Buckled 10⅜" from end 1
8/10/2017	45mm, 3A	−X	Coupled	Bending	2	4:45:35	Same
8/10/2017	45mm, 3A	−X	Coupled	Bending	3	4:48:50	Same Spot, tore hole in sleeve
8/10/2017	45mm, 3A	+X	Coupled	Bending	4	5:11:00	Middle → 10.5" from side 1
8/10/2017	45mm, 3A	+X	Coupled	Bending	5	5:13:55	½" tear in −Y side of sleeve, crack in −X shell → No torque data
8/10/2017	45mm, 3A	+X	Coupled	Bending	6	5:17:15	Same
8/10/2017	45mm, 3A	+X	Coupled	Bending	7	5:19:15	Same
8/10/2017	45mm, 3A	−Y	Coupled	Bending	8	5:23:40	Gear 2 climbed out of the worm gear
8/10/2017	45mm, 3A	−Y	Coupled	Bending	9	5:26:45	Slightly buckled at end 1, gear 2 climbed
8/10/2017	45mm, 3A	−Y	Coupled	Bending	10	5:30:45	Buckled at end 1, M2 gear train seemed to jam.
8/10/2017	45mm, 3A	−Y	Coupled	Bending	11	5:34:50	Worm Gear 2 was not turning during loading
8/11/2017	45mm, 3A	−Y	Coupled	Bending	12	10:09:30	Worm Gear 2 still not turning
8/11/2017	45mm, 3A	−Y	Coupled	Bending	13	10:29:45	Fixed Worm Gear 2.
8/11/2017	45mm, 3As	−Y	Coupled	Bending	14	10:37:55	Gear 2 climbed out of worm gear
8/11/2017	45mm, 3As	−Y	Coupled	Bending	15	10:40:20	Gear 2 climbed out of worm gear
8/11/2017	45mm, 3As	−Y	Coupled	Bending	16	10:47:55	Gear 2 climbed
8/11/2017	45mm, 3As	−Y	Coupled	Bending	17	10:54:10	Greg held down gear 2, buckled about 0.5" from end 1
8/11/2017	45mm, 3As	−Y	Coupled	Bending	18	10:57:05	Buckled 1.5" from side 1, Fracture on +X shell
8/11/2017	45mm, 3As	−Y	Coupled	Bending	19	11:02:25	Same Spot
8/11/2017	45mm, 3As	+Y	Coupled	Bending	20	11:06:00	Buckled and cracked 10⅝" from side 1, +X shell

SHEARLESS Characterization Testing

Date	Boom Size/#	Direction	State	Type	#	Start Time	Comments
8/11/2017	45mm, 3AS	+Y	Coupled	Bending	21	11:09:35	Failed in the middle and 1" from side 1
8/11/2017	45mm, 3AS	+Y	Coupled	Bending	22	11:12:55	Same Spot
8/11/2017	45mm, 3B	−X	Coupled	Bending	1	11:22:25	Tore sleeve, buckled 6 3/4" from end 1
8/11/2017	45mm, 3B	−X	Coupled	Bending	2	11:24:45	Same spot
8/11/2017	45mm, 3B	−X	Coupled	Bending	3	11:29:15	Buckled 7" from end 1, NO torque data
8/11/2017	45mm, 3B	−X	Coupled	Bending	4	11:35:10	Same spot
8/11/2017	45mm, 3B	+X	Coupled	Bending	5	12:20:50	Tore sleeve, buckled at 12" from end 1
8/11/2017	45mm, 3B	+X	Coupled	Bending	6	12:43:55	10 3/4" from end 1
8/11/2017	45mm, 3B	+X	Coupled	Bending	7	12:46:25	Same spot
8/11/2017	45mm, 3B	−X	Decoupled	Bending	8	12:53:40	9 3/4" from end 1
8/11/2017	45mm, 3B	−X	Decoupled	Bending	9	12:55:55	8 1/2" from end 1
8/11/2017	45mm, 3B	−X	Decoupled	Bending	10	12:57:50	9" from end 1, Slight crack on +Y side of −X
8/11/2017	45mm, 3B	+X	Decoupled	Bending	11	1:01:50	11 1/2" from end 1
8/11/2017	45mm, 3B	+X	Decoupled	Bending	12	1:03:45	11 1/8" from end 1
8/11/2017	45mm, 3B	+X	Decoupled	Bending	13	1:05:45	11" from end 1
8/11/2017	45mm, 3B	−Y	Decoupled	Bending	14	1:10:40	12" from end 1, Crack in +X shell, half of arc length
8/11/2017	45mm, 3B	−Y	Decoupled	Bending	15	1:13:35	Same spot
8/11/2017	45mm, 3B	−Y	Decoupled	Bending	16	1:15:50	Same spot
8/11/2017	45mm, 3B	+Y	Decoupled	Bending	17	1:18:50	8 1/2" from end 1 (Basically same spot as −Y)
8/11/2017	45mm, 3B	+Y	Decoupled	Bending	18	1:21:25	9" from end 1, Starting cracking from the other edge in the same spot
8/11/2017	45mm, 3B	+Y	Decoupled	Bending	19	1:24:55	Stopped a little early so crack wouldn't go through

11:01 at buckle at end 2 clamp slipped 9" from end of boom

APPENDIX B

TORQUE SENSOR VALIDATION TEST DATA

Table B.1: Torque sensor 1 validation test data

Screwdriver Setting (N-m)	Sensor Reading (N-m)	Screwdriver Used
0.3	0.2690	1
0.6	0.4447	1
0.9	0.7018	1
1.2	0.9117	1
1.2	0.9298	2
1.5	1.2985	2
1.8	1.3964	2
2.1	1.5895	2
2.4	1.9296	2
2.7	1.9518	2
3	2.2451	2
3	2.3092	3
3.5	2.7164	3
4	3.1273	3
4.5	3.3371	3
5	3.8729	3
5.5	4.2191	3
6	4.6795	3

Table B.2: Torque sensor 2 validation test data

Screwdriver Setting (N-m)	Sensor Reading (N-m)	Screwdriver Used
0.3	0.2691	1
0.6	0.4996	1
0.9	0.7355	1
1.2	0.9406	1
1.2	1.0259	2
1.5	1.4036	2
1.8	1.5493	2
2.1	1.8439	2
2.4	2.0610	2
2.7	2.4390	2
3	2.5002	2
3	2.7361	3
3.5	3.0977	3
4	3.5268	3
4.5	3.7132	3
5	4.3705	3
5.5	4.5238	3
6	5.1330	3

REFERENCES

[1] E. Levin, J. Pearson, and J. Carroll, "Wholesale debris removal from LEO," *Acta Astronautica*, vol. 73, pp. 100–108, Dec. 2011.

[2] S. Masunaga. (Jun. 23, 2016). "Boeing applies for license to launch proposed satellite constellation," LA times, (visited on 07/26/2016).

[3] (Jan. 26, 2016). "OneWeb Satellites Company Given Birth By Airbus Defence and Space + OneWeb," (visited on 07/26/2017).

[4] P. B. de Selding. (Jan. 19, 2015). "SpaceX To Build 4,000 Broadband Satellites in Seattle," Space News, (visited on 07/26/2016).

[5] D. J. Kessler and B. G. Cour-Palais, "Collision Frequency of Artificial Satellites: The Creation of a Debris Belt," *Journal of Geophysical Research*, vol. 83, pp. 2637–2646, Jun. 1978.

[6] D. J. Kessler, N. L. Johnson, J. C. Liou, and M. Matney, "The Kessler Syndrome: Implications to Future Space operations," Feb. 2010.

[7] "IADC Space Debris Mitigation Guidelines," Inter-Agency Space Debris Coordination Committee, IADC Action Item number 22.4, Sep. 2007.

[8] "Process for Limiting Orbital Debris," NASA, NASA Technical Standard NASA-STD-8719.14A, May 25, 2012.

[9] P. Anz-Meador and D. Shoots, Eds., *Orbital Debris Quarterly News: February 2017* vol. 21 1 Feb. 2017.

[10] D. S. McKnight, F. Di Pentino, A. Kaczmarek, and P. Dingman, "System engineering analysis of derelict collision prevention options," *Acta Astronautica*, vol. 89, pp. 248–253, May 2013.

[11] J. F.S. C. Commander, Ed. (Dec. 15, 2017). "The Satellite Situation Report."

[12] L. E. Jasper, C. R. Seubert, H. Schaub, T. Valery, and E. Yutkin, "TETHERED TUG FOR LARGE LOW EARTH ORBIT DEBRIS REMOVAL," in *AIAA/AAS Astrodynamics Specialists Conference*, Jan. 2012.

[13] H. Hakima and M. R. Emami, "Deorbiter CubeSat: Preliminary Design and Systems Engineering Budgets," in *68th International Astronautical Congress*, Sep. 2017.

[14] P. Andrist, A. Babbitt, V. Ethier, M. Pfaff, G. Rios-Georgio, and T. R. Welter, "DEbris Capture and Orbital Manipulation - DECOM," in *AIAA SPACE 2011 Conference*, Sep. 2011.

[15] M. Shan, J. Guo, and E. Gill, "Contact Dynamics of Net Capturing of Space Debris," in *68th International Astronautical Congress*, Sep. 2017.

[16] J. L. Forshaw and G. S. Aglietti, "THE REMOVEDEBRIS ADR MISSION: LAUNCH FROM THE ISS, OPERATIONS AND EXPERIMENTAL TIMELINES," in *68th International Astronautical Congress*, Sep. 2017.

[17] S.-I. Nishida, D. Uenaka, A. Shimizu, and S. Nakatani, "Light Weight Robot Arm for Capturing Space Debris," in *68th International Astronautical Congress*, Sep. 2017.

[18] X. Collaud, M. Richard-Noca, M. Leroy, G. J. Moreno, O. Kirchhoff, X. Deville, and P.-A. Mausli, "Simulation and Prototyping of the Cleanspace One Capture System," in *68th International Astronautical Congress*, Sep. 2017.

[19] (2016). "D3 Technical Sheet," D-Orbit, (visited on 11/16/2016).

[20] R Hoyt and R Forward, "THE TERMINATOR TETHER: AUTONOMOUS DEORBIT OF LEO SPACECRAFT FOR SPACE DEBRIS MITIGATION," in *38th Aerospace Sciences Meeting*, Jan. 2000.

[21] (2015). "The Terminator Tape and Terminator Tether Satellite Deorbit Systems: Low-Cost, Low-Mass End-of-Mission Disposal for Space Debris Mitigation," Tethers Unlimited, (visited on 07/27/2016).

[22] K. T. Nock, K. M. Aaron, and D. S. McKnight, "Removing Orbital Debris with Less Risk," *Journal of Spacecraft and Rockets*, vol. 50, no. 2, pp. 365–379, Mar. 2013.

[23] K. T. Nock, K. L. Gates, K. M. Aaron, and A. D. McRonald, "Gossamer Orbit Lowering Device (GOLD) for Safe and Efficient De-orbit," in *AIAA/AAS Astrodnyamics Specialist Conference*, Aug. 2010.

[24] (2016). "Minotaur I Launch Vehicle," Spaceflight101.com, (visited on 12/16/2016).

[25] (2016). "MMA's DragNET Successfully Deorbits Minotaur Upper Stage," MMA Design, (visited on 12/15/2016).

[26] S. Clark. (Nov. 9, 2013). “Student-built satellites, military payloads put in orbit,” Spaceflight101.com, (visited on 12/15/2017).

[27] eoPortal News. (2017). “InflateSail,” (visited on 03/08/2018).

[28] The University of Toronto, Ed. (2017-05-11). “After Only One Week, CanX-7 Shows Drag Sails are Effective at Deorbiting Satellite,” (visited on 03/09/2018).

[29] (2014). “DRAGNET (Pat.) De-orbit system,” MMA Design, (visited on 09/04/2015).

[30] P. Harkness, M. McRobb, P. Lützkendorf, R. Milligan, A. Feeney, and C. Clark, “Development status of AEOLDOS - A deorbit module for small satellites,” *Advances in Space Research*, vol. 54, pp. 82–91, 2014.

[31] O. R. Stohlman and V. Lappas, “Deorbitsail: a deployable sail for de-orbiting,” in *54nd AIAA/ASME/ASCE/AHS/ASC Structures, Structural Dynamics and Materials Conference*, Apr. 2013.

[32] H. J. Kramer. (2015). “DeOrbitSail (DOS) Nanosatellite Mission,” (visited on 05/16/2017).

[33] A. Viquerat, M. Schenk, V. Lappas, and B. Sanders, “Functional and Qualification Testing of the InflateSail Technology Demonstrator,” in *2nd AIAA Spacecraft Structures Conference*, 2015.

[34] B. Shmuel, J. Hiemstra, V. Tarantini, F. Singarayar, G. Bonin, and R. E. Zee, “The Canadian Advanced Nanospace eXperiment 7 (CanX-7) Demonstration Mission: De-Orbiting Nano- and Microspacecraft,” in *26th Annual AIAA/USU Conference on Small Satellites*, Aug. 2012.

[35] The University of Toronto, Ed. (May 4, 2017). “CanX-7 Sucessfully Deploys Drag Sails Kicking Off Deorbiting Demonstration,” (visited on 03/01/2018).

[36] J. L. Wirght, *Space Sailing*. Gordon and Breach Science Publishers, 1992, p. 258, ISBN: 2881248039.

[37] L. Johnson, R. Young, E. Montgomery, and D. Alhorn, “Status of solar sail technology within NASA,” *Advances in Space Research*, vol. 48, pp. 1687–1694, Dec. 2010.

[38] D. M. Murphy, “Validation of a Scalable Solar Sailcraft System,” *Journal of Spacecraft and Rockets*, vol. 44, no. 4, pp. 797–808, Jul. 2007.

[39] D. Lichodziejewski, B. Derbes, D. W. Sleight, and T. Mann, “VACUUM DEPLOYMENT AND TESTING OF A 20M SOLAR SAIL SYSTEM,” May 2006.

[40] E. Howell. (May 7, 2014). “Ikaros: First Successful Solar Sail,” Space.com, (visited on 09/01/2016).

[41] Y. Shirasawa, O. Mori, H. Sawada, Y. Chishiki, and K. Kitamura, “A Study on Membrane Dynamics and Deformation of Solar Power Sail Demonstrator ”IKAROS”,” in *53nd AIAA/ASME/ASCE/AHS/ASC Structures, Structural Dynamics and Materials Conference*, Apr. 2012.

[42] H. Sawada, O. Mori, N. Okuizumi, Y. Shirasawa, Y. Miyazaki, M. C. Natori, S. Matunaga, H. Furuya, and H. Sakamoto, “Mission Report on The Solar Power Sail Deployment Demonstration of IKAROS,” in *52nd AIAA/ASME/ASCE/AHS/ASC Structures, Structural Dynamics and Materials Conference*, Apr. 2011.

[43] A. F.M.-E. Heaton, B. F. Faller, and C. K. Katan, “Nanosail– D Orbital and Attitude Dynamics,” pp. 95–113, 2014.

[44] D. Alhorn, J. P. Casas, E. F. Agasid, C. Adams, G. Laue, C. Kitts, and S. O’Brien, “NanoSail-D: The Small Satellite that Could!” In *25th Annual AIAA/USU Conference on Small Satellites*, Aug. 2011.

[45] L. Johnson, J. Castillo-Rogez, and L. McNutt, “Solar Sail Propulsion for Interplanetary CubeSats,” in *52st AIAA/SAE/ASEE Joint Propulsion Conference*, Jul. 2015.

[46] C. Biddy and T. Svitek, “LightSail-1 Solar Sail Design and Qualification,” in *41st Aerospace Mechanisms Symposium*, May 2012.

[47] J. Davis. (Jun. 9, 2015). “LightSail Test Mission Declared Success; First Image Complete,” The Planetary Society, (visited on 09/04/2015).

[48] R. W. Ridenoure, D. A. Spencer, D. A. Stetson, B. Betts, R. Munakata, S. D. Wong, A. Diaz, B. L. Plante, J. D. Foley, and J. M. Bellardo, “Status of the Dual CubeSat LightSail Program,” Aug. 2015.

[49] D. A. Spencer, R. W. Ridenoure, R. Munakata, S. D. Wong, A. Diaz, D. A. Stetson, B. Betts, B. L. Plante, J. D. Foley, and J. M. Bellardo, “Testing the LightSail Program: Advancing Solar Sailing Technology Using a CubeSat Platform,” *Journal of Small Satellites*, vol. 5, pp. 531–550, 2016.

[50] (2013). “Sunjammer: First NASA Solar Sail Mission to Deep Space,” Space Services Holdings, Inc., (visited on 09/04/2015).

[51] A. L. Hoskin, “Blossoming of Coiled Deployable Booms,” in *56th AIAA/ASCE/ASC Structures, Structural Dynamics, and Materials Conference*, 2015.

[52] N. Adeli, "Deployment System for the CubeSail nano-Solar Sail Mission," in *24th Annual AIAA/USU Conference on Small Satellites*, Aug. 2010.

[53] M. Mobrem and C. Spier, "Design and Performance of the Telescopic Tubular Mast," May 2012.

[54] D. M. Murphy, T. W. Murphey, and P Gierow, "Scalable Solar-Sail Subsystem Design Concept," *Journal of Spacecraft and ...*, vol. 40, no. 4, pp. 539–547, Jul. 2003.

[55] C Dupuy and O Le Couls, "Gossamer Technology to Deorbit LEO Non-Propulsion Fitted Satellite.pdf," May 2010.

[56] O. R. Stohlman and E. R. Loper, "Thermal Deformation of Very Slender Triangular Rollable and Collapsible Booms," Jan. 2016.

[57] K. A. Seffen and S Pellegrino, "Deployment Dynamics of Tape Springs," in *Proceedings of the Royal Society London A*, Mar. 8, 1999.

[58] J. A.C.U.A. A. Banik and T. W. Murphey, "Performance Validation of the Triangular Rollable and Collapsible Mast," in *24th Annual AIAA/USU Conference on Small Satellites*, Aug. 9, 2010.

[59] J. M. Fernandez, "Advanced Deployable Shell-Based Composite Booms For Small Satellite Structural Applications Including Solar Sails," in *4th International Solar Sailing Symposium*, Kyoto, Japan, Jan. 17, 2017.

[60] T. W. Murphey and J. A.C.U.A. A. Banik, "Triangular Rollable and Collaspsible Boom," pat. US 7,895,795 B1, Mar. 1, 2011.

[61] J. M. Fernandez, M Schenk, G Prassinos, V. J. Lappas, and S. O. Erb, "Deployment Mechanisms of a Gossamer Satellite and Deorbiter," in *15th European Space Mechanisms & Tribology Symposium*, Sep. 2013.

[62] B. Wang. (2017-03-04). "Total global satellite plans could have around 20,000 satellites in low and mid earth orbits in the 2020s."

[63] WorldVu Satellites Limited, *Application for Satellite Space Station Authorizations*, FCC File Number: SAT-LOI-20160428-00041, 2016-04-28.

[64] Space Exploration Holdings, LLC, *Application for Satellite Space Station Authorizations*, FCC File Number: SAT-LOA-20161115-00118, 2016-11-15.

[65] Space Exploration Technologies Corp, *FCC Experimental License Application*, FCC File Number: 0298-EX-CN-2016; Call Sign: WI2XTA, 2016-12-13.

[66] The Boeing Company, *Application for Satellite Space Station Authorizations*, File Number: SAT-LOA-20160622-0058, Jun. 22, 2016.

[67] Telesat Canada, *Application for Satellite Space Station Authorizations*, FCC File Number: SAT-PDR-20170301-00023, 2017-03-01.

[68] A. Mehrparvar, *CubeSat Design Specification*, 13th ed., The CubeSat Program, Cal Poly SLO, 2014.

[69] R. Hevner, W. Holemans, J. Puig-Suari, and R. Twiggs, "An Advanced Standard for CubeSats," in *25th Annual AIAA/USU Conference on Small Satellites*, 2011.

[70] R. Hoyt. (Sep. 10, 2015). "Space Debris Mitigation Technologies."

[71] A. C. Long and D. A. Spencer, "A Scalable Drag Sail for the Deorbit of Small Satellites," *Journal of Small Satellites*, Submitted.

[72] A. Long and D. A. Spencer, "Stability of a Deployable Drag Device for Small Satellite Deorbit," in *AIAA/AAS Astrodynamics Specialist Conference*, Sep. 2016.

[73] J. R. Wertz, D. E. Everett, and J. J. Puschell, *Space Mission Engineering: The New SMAD*. Microcosm Press, 2011, 128–131, 214–217.

[74] L. G. Jacchia, "Revised Static Models of the Thermosphere and Exosphere with Empirical Temperature Profiles," 1971.

[75] A. E. Hedin, "MSIS-86 Thermospheric Model," *Journal of Geophysical Research*, vol. 92, pp. 4649–4662, May 1, 1987.

[76] A. E. Hedin, "Extension of the MSIS Thermosphere Model into the middle and lower atmosphere," *Journal of Geophysical Research*, vol. 96, pp. 1159–72, Feb. 1, 1991.

[77] NOAA Space Weather Prediction Center. (Mar. 5, 2018). "Solar Cycle Progression," (visited on 03/21/2018).

[78] D. Chavali and S. Hughes. (Mar. 29, 2016). "GMAT WikiStage," (visited on 08/02/2016).

[79] A. Johnson and T. Itchkawich, "Investigation of the Relative Merits Between DAS and ORSAT for Small Satellite Reentry Analysis," in *IEEE Aerospace Conference*, Mar. 2007, pp. 1–9.

[80] A. M. Cebrin, S. Tamrazian, I. Sebastio, D. Spencer, and A. Alexeenko, "DSMC-SPARTA Aerodynamic Characterization of a Deorbiting CubeSat," in *31st Interna-*

tional Symposium on Rarefied Gas Dynamics, Preprint, Glasgow, Scotland, Jul. 23, 2018.

[81] J. M. Fernandez, "Low-Cost Gossamer Systems for Solar Sailing & Spacecraft Deorbiting Applications," PhD thesis, Jul. 2014.

[82] G. Greschik, T. M. Murphey, M. M. Mikulas, and W. K. Belvin, "A Rule of Thumb for the Suspension of Film Sheets Without Catenaries," in *44th AIAA/ASME/ASCE/AHS Structures, Structural Dynamics, and Materials Conference*, Apr. 2003.

[83] A. Adler, M. M. Mikulas, and J. M. Hedgepeth, "Static and Dynamic Analysis of Partially Wrinkled Membrane Structures," Apr. 2000.

[84] J. R. Blandino, J. D. Johnston, and U. K. Dharamsi, "Corner Wrinkling of a Square Membrane Due to Symmetric Mechanical Loads," vol. 39, Oct. 2002.

[85] G Greschik and M. M. Mikulas, "Design Study of a Square Solar Sail Architecture," vol. 39, Sep. 2002.

[86] T. W. Murphey, D. M. Murphy, M. M. Mikulas, and A. Adler, "A Method to Quantify the Thrust Degradation Effects of Structural Wrinkles in Solar Sails," Apr. 2002.

[87] K. N. Slade, W. K. Belvin, and V Behun, "Solar Sail Loads, Dynamics, and Membrane Studies.pdf," Apr. 2002.

[88] D. W. Sleight and D. M. Muheim, "Parametric Studies of Square Solar Sails Using Finite Element Analysis," Apr. 2004.

[89] B. K. Taleghani, D. W. Sleight, D. M. Muheim, W. K. Belvin, and J. T. Wang, "Assessment of analysis approaches for solar sail structural response," Jul. 2003.

[90] K. A. Hart, S. Dutta, K. R. Simonis, B. A. Steinfeldt, and R. D. Braun, "Analytically-derived Aerodynamic Force and Moment Coefficients of Resident Space Objects in Free-Molecular Flow," in *AIAA Atmospheric Fligt Mechanics Conference*, Jan. 13, 2014.

[91] J. M. Fernandez, L. Visagie, M. Schenk, O. R. Stohlman, G. S. Aglietti, V. J. Lappas, and S. Erb, "Design and development of a gossamer sail system for deorbiting in low earth orbit," *Acta Astronautica*, pp. 204–225, 103 2014.

[92] A. R. Sobey and T. R. Lockett, "Design and Development of NEA Scout Solar Sail Deployer Mechanism," in *43rd Aerospace Mechnisms Symposium*, May 2016.

[93] C. R. McInnes, *Solar Sailing: Technology, Dynamics and Mission Applications*. Praxis Publishing, 1999.

[94] M. Arya and S. Pellegrino, "Deployment Mechanics of Highly Compacted Thin Membrane Structures," 2014.

[95] O. A. Bauchau and J. I. Craig, *Structural Analysis: With Applications to Aerospace Structures*. Springer, 2009, pp. 193, 784, ISBN: 978-90-481-2515-9.

[96] Nexolve. (2017). "CP1 Polymide," (visited on 09/01/2017).

[97] Nexolve. (2017). "CORIN XLS Polymide," (visited on 09/01/2017).

[98] R. C. Tennyson, "Atomic oxygen effects on space inflatable materials," in *Gossamer spacecraft: membrane and inflatable structures technology for space applications*, ser. Progress in Astronautics and Aeronautics, C. H. M. Jenkins, Ed., vol. 191, AIAA, 2001, pp. 281–302.

[99] G. T. Yi, K. K. de Groh, B. A. Banks, A. Haloua, E. C. Imka, and G. G. Mitchell, "Overview of the MISSE 7 Polymers and Zenith Polymers Experiments after 1.5 Years of Space Exposure," NASA/TM - 2013-217848, Oct. 2016.

[100] K. K. de Groh, B. A. Banks, J. A. Dever, D. A. Jaworske, S. K. Miller, E. A. Sechkar, and S. R. Panko, "NASA Glenn Research Center's Materials International Space Station Experiments (MISSE 1-7)," NASA/TM - 2008-215482, Dec. 2008.

[101] R. J. Suggs, "Future Solar Activity Estimates for Use in Prediction of Space Environmental Effects on Spacecraft Orbital Lifetime and Performance," George C. Marshall Space Flight Center, Tech. Rep., Jun. 2016.

[102] B. Etkin, *Dynamics of Atmospheric Flight*. Dover Publications, 2000.

[103] S. A. Schaaf and P. L. Chambre, *Flow of Rarefied Gases*. Princeton University Press, 1961.

[104] G. A. Bird, *Molecular Gas Dynamics and the Direct Simulation of Gas Flow*. Oxford University Press, 1994, pp. 148–182.

[105] E. W. Weisstein. (). "Erf." MathWorld – A Wolfram Web Resource, Ed., MathWorld – A Wolfram Wed Resource, (visited on 08/14/2016).

[106] B. Wie, *Space Vehicle Dynamics and Control*. AIAA Education Series, 2008, ch. 6.

[107] R Forward, "Grey Solar Sails," Jul. 1989.

[108] T. R. Kane and D. A. Levinson, *Dynamics: Theory and Applications*. McGraw-Hill Book Company, 1985, pp. 366, 370, ISBN: 0-07-037846-0.

[109] P. A. Tipler and G. Mosca, *Physics for Scientists and Engineers: Volume 1 Mechanics, Oscillations and Waves, Thermodynamics*, 5th. W. H. Freeman and Company, 2004, p. 274, ISBN: 0-7167-0809-4.

[110] R. R. Bate, D. D. Mueller, and J. E. White, *Fundamentals of Astrodynamics*. Dover Publications, 1971, pp. 419–424, ISBN: 0-486-60061-0.

[111] T. S. Kelso. (May 17, 2014). "Visually Observing Earth Satellites," (visited on 10/17/2014).

[112] M. Schoenenberger, A. Dyakonov, and J. V. Norman, "Mars Science Laboratory Aerodynamic Database," NASA Langley Research Center, Aug. 3, 2012, G1 –G6.

[113] P. C. Roberts and P. G. Harkness, "Drag Sail for End-of-Life Disposal from Low Earth Orbit," *Journal of Spacecraft and Rockets*, vol. 44, no. 6, Nov. 2007.

[114] L. McNutt, L. Johnson, D. Clardy, J. Castillo-Rogez, A. Frick, and L. Jones, "Near-Earth Asteroid Scout," in *Space Conference and Exposition*, Aug. 2014.

[115] M. LaChance. (2016). "Purdue wins a launch slot on Atlas V." I. P. University, Ed., (visited on 08/31/2017).

[116] "CubeSat Design Specification, Rev 13," The CubeSat Program, Cal Poly SLO, 2014.

[117] F Dalla Vedova, H Henrion, M Leipold, T. Girot, R Vaudemont, T. Belmonte, K Fleury, and O Le Couls, "The Solar Sail Materials (SSM) project - Status of activities," *Advances in Space Research*, vol. 48, pp. 1922–1926, Aug. 2011.

[118] A. C. Long and D. A. Spencer, "A Passively Stable Pyramid Sail for the Deorbit of Small Satellite Constellations," in *68th International Astronautical Congress*, Adelaide, Australia, Sep. 2017.

[119] J. Fernandez, "SHEAth-Based Rollable LEnticular-Shaped and low-Stiction Composite Boom," pat. US 9,863,148 B2, Jan. 9, 2018.

[120] A. Price, E. Balerud, M. Cox, and C. Nelson, "Retractable boom design for sounding rocket experiments," in *32nd Annual AIAA/USU Conference on Small Satellites*, (Preprint), 2018.

[121] A. J. Lee and J. M. Fernandez, "Mechanics of Bistable Two-Shelled Composite Booms," in *2018 AIAA Spacecraft Structures Conference*, Jan. 2018.

[122] C. Leclerc, L. Wilson, M. A. Bessa, and S. Pellegrino, "Characterization of Ultra-Thin Composite Triangular Rollable and Collapsible Booms," in *4th AIAA Spacecraft Structures Conference*, Grapevine, Texas, Jan. 2017.

[123] D. Brown, *Tracker: Video Analysis and Modeling Tool*, version 4.9.8, Open Source Physics, Jun. 17, 2017.